ARISTOTLE UNIVERSITY OF THESSALONIKI
SCHOOL OF MEDICINE
SECTOR OF RADIOLOGY, MEDICAL PHYSICS & INFORMATICS
MEDICAL PHYSICS LABORATORY

DIRECTOR : ASSOCIATE PROFESSOR ANASTASIOS SIOUNTAS

ACADEMIC YEAR 2018-2019 THESIS NO : 4211

COMMISSIONING CHARACTERIZATION AND EXPLOITATION OF THE CERN SHIELDING BENCHMARK FACILITY (CSBF)

ELPIDA ILIOPOULOU
MEDICAL PHYSICIST

Ph.D. THESIS
SUBMITTED TO THE SCHOOL OF MEDICINE
OF ARISTOTLE UNIVERSITY OF THESSALONIKI

THESSALONIKI, 2018

ΑΡΙΣΤΟΤΕΛΕΙΟ ΠΑΝΕΠΙΣΤΗΜΙΟ ΘΕΣΣΑΛΟΝΙΚΗΣ
ΤΜΗΜΑ ΙΑΤΡΙΚΗΣ
ΤΟΜΕΑΣ ΑΚΤΙΝΟΛΟΓΙΑΣ, ΙΑΤΡΙΚΗΣ ΦΥΣΙΚΗΣ & ΠΛΗΡΟΦΟΡΙΚΗΣ
ΕΡΓΑΣΤΗΡΙΟ ΙΑΤΡΙΚΗΣ ΦΥΣΙΚΗΣ

ΔΙΕΥΘΥΝΤΗΣ : ΑΝΑΠΛΗΡΩΤΗΣ ΚΑΘΗΓΗΤΗΣ ΑΝΑΣΤΑΣΙΟΣ ΣΙΟΥΝΤΑΣ

ΠΑΝΕΠ. ΕΤΟΣ 2018-2019 ΑΡΙΘΜ. ΔΙΔ. ΔΙΑΤΡΙΒΗΣ : 4211

ΛΕΙΤΟΥΡΓΙΑ ΧΑΡΑΚΤΗΡΙΣΜΟΣ ΚΑΙ ΕΚΜΕΤΑΛΛΕΥΣΗ ΤΗΣ ΕΓΚΑΤΑΣΤΑΣΗΣ ΘΩΡΑΚΙΣΕΩΝ ΤΟΥ CERN

ΕΛΠΙΔΑ ΗΛΙΟΠΟΥΛΟΥ
ΦΥΣΙΚΟΣ ΙΑΤΡΙΚΗΣ - ΑΚΤΙΝΟΦΥΣΙΚΟΣ

ΔΙΔΑΚΤΟΡΙΚΗ ΔΙΑΤΡΙΒΗ
ΥΠΟΒΛΗΘΗΚΕ ΣΤΟ ΤΜΗΜΑ ΙΑΤΡΙΚΗΣ
ΤΟΥ ΑΡΙΣΤΟΤΕΛΕΙΟΥ ΠΑΝΕΠΙΣΤΗΜΙΟΥ ΘΕΣΣΑΛΟΝΙΚΗΣ

ΘΕΣΣΑΛΟΝΙΚΗ, 2018

ΑΡΙΣΤΟΤΕΛΕΙΟ ΠΑΝΕΠΙΣΤΗΜΙΟ ΘΕΣΣΑΛΟΝΙΚΗΣ
ΣΧΟΛΗ ΕΠΙΣΤΗΜΩΝ ΥΓΕΙΑΣ
ΤΜΗΜΑ ΙΑΤΡΙΚΗΣ
ΤΟΜΕΑΣ ΑΚΤΙΝΟΛΟΓΙΑΣ, ΙΑΤΡΙΚΗΣ ΦΥΣΙΚΗΣ & ΠΛΗΡΟΦΟΡΙΚΗΣ

ΠΡΟΕΔΡΟΣ ΤΟΥ ΤΜΗΜΑΤΟΣ
ΑΣΤΕΡΙΟΣ ΚΑΡΑΓΙΑΝΝΗΣ

ΔΙΕΥΘΥΝΤΗΣ ΤΟΥ ΤΟΜΕΑ
ΚΩΝΣΤΑΝΤΙΝΟΣ ΚΟΥΣΚΟΥΡΑΣ

TRIPARTITE ADVISORY COMMITTEE:

ANASTASIOS SIOUNTAS, ASSOCIATE PROFESSOR, SUPERVISOR

BAMIDIS PANAGIOTIS, ASSOCIATE PROFESSOR

DR. FROESCHL ROBERT, CERN SUPERVISOR

7-MEMBER EXAMINATION COMMITTEE:

ANASTASIOS SIOUNTAS, ASSOCIATE PROFESSOR, SUPERVISOR

BAMIDIS PANAGIOTIS, ASSOCIATE PROFESSOR

DR. FROESCHL ROBERT, CERN SUPERVISOR

PAPANASTASIOU EMMANOUIL, ASSISTANT PROFESSOR

TZITZIKAS IOANNIS, ASSISTANT PROFESSOR

KITIS GEORGIOS, PROFESSOR (SCHOOL OF PHYSICS, AUTH)

STOULOS STYLIANOS, ASSOCIATE PROFESSOR (SCHOOL OF PHYSICS, AUTH)

ARISTOTLE UNIVERSITY OF THESSALONIKI
SCHOOL OF MEDICINE
SECTOR OF RADIOLOGY, MEDICAL PHYSICS & INFORMATICS
MEDICAL PHYSICS LABORATORY

DIRECTOR : ASSOCIATE PROFESSOR ANASTASIOS SIOUNTAS

ACADEMIC YEAR 2018-2019 THESIS NO : 4211

COMMISSIONING CHARACTERIZATION AND EXPLOITATION OF THE CERN SHIELDING BENCHMARK FACILITY (CSBF)

ELPIDA ILIOPOULOU
MEDICAL PHYSICIST

Ph.D. THESIS
SUBMITTED TO THE SCHOOL OF MEDICINE
OF ARISTOTLE UNIVERSITY OF THESSALONIKI

THESSALONIKI, 2018

Introduction

One of the main application of the FLUKA Monte Carlo simulation code, is in the design of new beam facilities. An indispensable part of the FLUKA code development process, is benchmarking of predictions of new features against experimental data, for example benchmarking the deep shielding penetration by the particles from high energy proton accelerator operations. For this reason, the CERN High energy AcceleRator Mixed field facility (CHARM) and the CERN Shielding Benchmark Facility (CSBF) were especially designed to obtain experimental data, for deep shielding penetration studies. The main goals of this thesis, are to design and to characterize the CSBF, both by means of FLUKA Monte Carlo simulations of the radiation spectra and their validation by activation experiments.

The first prototype of the CSBF was installed, together with the entire shielding of the CHARM facility, during the Long Shut-down 1 (LS1) in 2013/2014. The CHARM facility, has been operating with 24 GeV/c proton beam, since September 2014. A first characterization of the CSBF facility was performed in July 2015, with the activation of bismuth and aluminium detectors in the CSBF. Monte Carlo simulations with the FLUKA code, have been performed to estimate the production yields of bismuth isotopes and sodium for these samples. The production yields estimated by FLUKA Monte Carlo simulations, are compared to the production yields obtained from γ-spectroscopy measurements of the samples taking the beam intensity profile into account.

With the experience acquired during the activation campaign in 2015, the

CSBF has been significantly upgraded during the extended year-end technical stop at the beginning of 2016. Consequently, in September 2016 there was a second activation campaign with activation of bismuth, aluminium and indium samples that were placed in the CSBF, to characterize the upgraded version of the CSBF. Monte Carlo simulations with the FLUKA code, have been performed to estimate the specific production yields of bismuth, sodium and indium isotopes, for these samples, in the new configuration and have then been compared to the production yields obtained from γ-spectroscopy measurements of the samples taking the beam intensity profile into account.

In parallel to the activation campaign in 2016, there was a series of measurements with a high-pressure ionisation chamber, filled with hydrogen gas at 20 bar, calibrated for measuring ambient dose equivalent rates, in the material test location. By comparing the dose rate measured at different positions, the neutron spectrum averaged attenuation lengths of the various commonly used shielding materials are estimated.

The results obtained for the activation campaigns in 2015 and 2016, have shown that the radiation fields in the CSBF are now well understood and well described by FLUKA. These results can be used as guidelines for similar studies at future proton accelerators and at medical facilities.

Εισαγωγή

Μία από τις κύριες εφαρμογές του κώδικα προσομοιώσεων FLUKA Monte Carlo, είναι ο σχεδιασμός νέων εγκαταστάσεων ιοντίζουσας ακτινοβολίας. Ένα αναπόσπαστο κομμάτι της διαδικασίας ανάπτυξης του κώδικα FLUKA, είναι η συγκριτική αξιολόγηση προγνωστικών για νέα χαρακτηριστικά έναντι πειραματικών δεδομένων, για παράδειγμα, συγκριτική αξιολόγηση της διείσδυσης σε βαθιά θωράκιση από σωματίδια που προέρχονται από επιταχυντή πρωτονίων υψηλής ενέργειας εν λειτουργία. Για το λόγο αυτό, το CERN High Energy Accelerator Mixed Field Facility (CHARM) και το CERN Shielding Benchmark Facility (CSBF) σχεδιάστηκαν ειδικά για την απόκτηση πειραματικών δεδομένων για μελέτες διείσδυσης σωματιδίων σε βαθιά θωράκιση. Οι κύριοι στόχοι αυτής της διατριβής, είναι ο σχεδιασμός και ο χαρακτηρισμός του CSBF, τόσο με προσομοιώσεις των φασμάτων ακτινοβολίας με FLUKA Monte Carlo, όσο και με την επικύρωση τους με πειράματα ενεργοποίησης.

Το πρώτο πρωτότυπο του CSBF εγκαταστάθηκε, μαζί με ολόκληρη τη θωράκιση της εγκατάστασης CHARM, κατά τη διάρκεια του Long Shut-down 1 (LS1) το 2013/2014. Η εγκατάσταση CHARM λειτουργεί με δέσμη πρωτονίων 24 GeV/c από τον Σεπτέμβριο του 2014. Ένας πρώτος χαρακτηρισμός της εγκατάστασης CSBF πραγματοποιήθηκε τον Ιούλιο του 2015, με την πραγματοποίηση πειραμάτων ενεργοποίησης ανιχνευτών βισμουθίου και αλουμινίου στο CSBF. Οι προσομοιώσεις Monte Carlo με τον κώδικα FLUKA, πραγματοποιήθηκαν για την εκτίμηση των αποδόσεων παραγωγής ισοτόπων βισμουθίου και νατρίου, για αυτά τα δείγματα. Οι αποδόσεις παραγωγής που εκτιμήθηκαν από τις προσομοιώσεις FLUKA Monte Carlo, συγκρίθηκαν με τις αποδόσεις παρα-

γωγής που λήφθηκαν από τις μετρήσεις της γ-φασματοσκοπίας των δειγμάτων, λαμβάνοντας υπόψη το προφίλ της έντασης δέσμης.

Με την εμπειρία που αποκτήθηκε κατά τη διάρκεια της εκστρατείας ενεργοποίησης το 2015, το CSBF αναβαθμίστηκε σημαντικά κατά τη διάρκεια της εκτεταμένης τεχνικής διακοπής στο τέλος του έτους 2016. Συνεπώς, τον Σεπτέμβριο του 2016 πραγματοποιήθηκε μια δεύτερη εκστρατεία πειραμάτων με ενεργοποίηση δειγμάτων βισμουθίου, αλουμινίου και ινδίου, που τοποθετήθηκαν στο CSBF, για να χαρακτηρίσουν την αναβαθμισμένη έκδοση του CSBF. Οι προσομοιώσεις Monte Carlo με τον κώδικα FLUKA, πραγματοποιήθηκαν για την εκτίμηση των ειδικών αποδόσεων παραγωγής των ισοτόπων βισμουθίου, νατρίου και ινδίου, για τα δείγματα αυτά, στη νέα εγκατάσταση και έπειτα συγκρίθηκαν με τις αποδόσεις παραγωγής που λήφθηκαν από τις μετρήσεις γ-φασματοσκοπίας των δειγμάτων, λαμβάνοντας υπόψη το προφίλ της έντασης δέσμης.

Παράλληλα με την εκστρατεία ενεργοποίησης το 2016, πραγματοποιήθηκε μια σειρά μετρήσεων με θάλαμο ιονισμού υδρογόνου υπό υψηλή πίεση 20 bar, βαθμονομημένο για τη μέτρηση ρυθμού ισοδύναμης δόσης περιβάλλοντος, στο shielding material test location. Με τη σύγκριση του ρυθμού δόσης που μετρήθηκε σε διαφορετικές θέσεις, υπολογίζεται ο μέσος όρος του μήκους εξασθένησης φάσματος νετρονίων των διάφορων, συνήθως, χρησιμοποιούμενων υλικών θωράκισης.

Τα αποτελέσματα που προέκυψαν για τις εκστρατείες ενεργοποίησης το 2015 και το 2016 έδειξαν ότι τα πεδία ακτινοβολίας στο CSBF είναι τώρα καλά κατανοητά και καλά περιγραφόμενα από την FLUKA. Αυτά τα αποτελέσματα μπορούν να χρησιμοποιηθούν ως κατευθυντήριες γραμμές για παρόμοιες μελέτες σε μελλοντικούς επιταχυντές πρωτονίων και σε ιατρικές εγκαταστάσεις.

Acknowledgements

I would like to warmly thank Dr. Robert Froeschl for his continuous guidance and support throughout my PhD work at CERN.

I would also like to express my gratitude to Pr. Anastasios Siountas and Pr. Panagiotis Bamidis for their advice and for their valuable help during my thesis.

Furthermore, I wish to thank my office mate and friend Florent for the understanding and for making this time very joyful.

A special thanks goes to Lina and Nelly for the endless professional and personal conversations we had and the numerous pleasant moments we shared.

Moreover, I would like to thank Julia and Biagio for the fun and relaxed times we had.

I owe special thanks to my friends Marilena, Popi and Stella that supported me despite the distance and their thoughts were always with me.

I am deeply grateful to Francesco for his advice, encouragement all this time and for always being there for me.

Finally, I would like to thank my parents and my brother for believing in me and teaching me that nothing is impossible.

Contents

Chapter 1

CERN accelerator complex

This chapter provides a short review of CERN and CERN's accelerator complex.

1.1 General

CERN, the European Organization for Nuclear Research, is the world's largest particle physics laboratory and is situated at the French-Swiss border, in the area of Geneva. It was founded in 1954 by 12 European countries but now, as of 2017, it has 22 member states. The mission of CERN is to push forward the frontiers of knowledge (e.g the secrets of the Big Bang, what was the matter like within the first moments of the Universe's existence), develop new technologies for accelerators and detectors (e.g information technology-the Web and the GRID, medicine-diagnosis and therapy), train scientists and engineers of tomorrow and unite people from different countries and cultures. At CERN there are currently 2300 staff, 1620 other paid personnel and 10500 users from all around the world. The main fields of interest of CERN are particle, detector and applied physics as well as data acquisition and storage.

1.2 CERN accelerator complex

The CERN accelerator complex is a sequence of accelerators that increase gradually the energy of the particles. Each of these machines rises the energy of the particles before they are injected into the next one. The main particles currently accelerated throughout the CERN accelerator complex are protons and heavy ions. Several experimental areas use protons to produce antiprotons, neutrons, pions or neutrinos. The energies of these particles are high enough so to create a large shower of secondary particles.

The linear accelerator Linac 2 that works as a proton injector accelerates the protons. After the first acceleration through Linac 2 the particles continue to accelerate through a chain of circular accelerators. The particles are accelerated with increasing energy in each and every successive accelerator. As soon as the particles reach the desired final energy that corresponds in a specific accelerator, they can continue in the accelerator chain till they arrive in the LHC or can be extracted to experimental areas that have fixed target experiments that are running in parallel to the LHC. An illustration of the CERN accelerator complex is shown in Fig. 1.1.

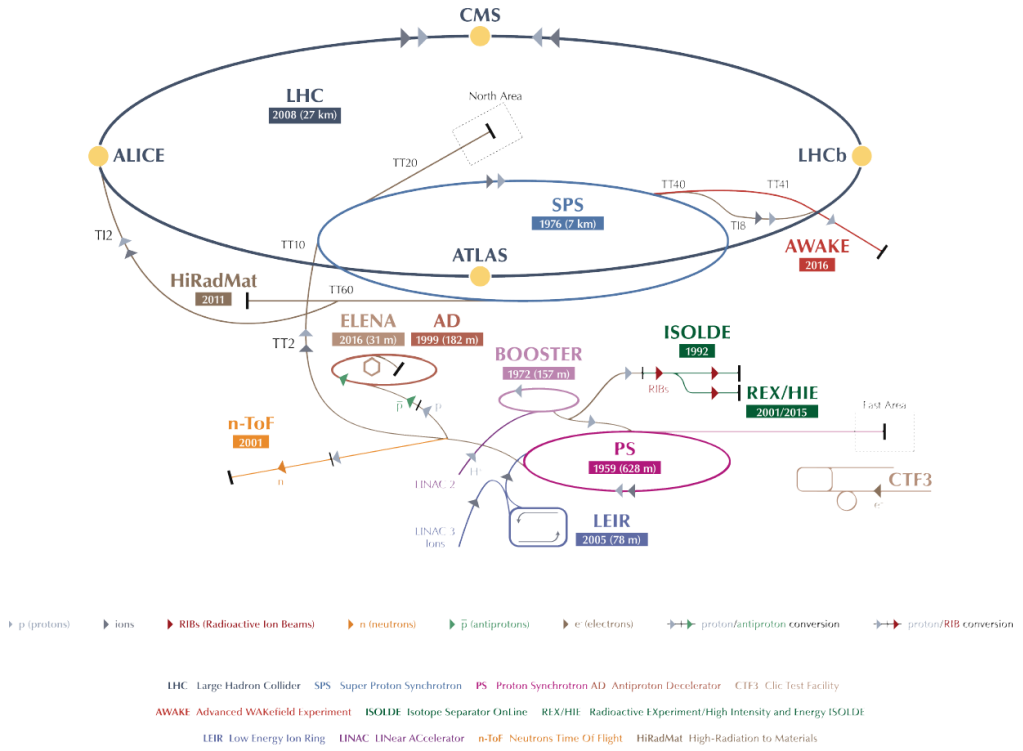

Figure 1.1: CERN accelerator complex.

1.3 LHC injection chain & LHC experiments

All protons start from a bottle of hydrogen gas that is located in the start of the Linac 2. Under an electric field in the Linac 2 source the electrons of the hydrogen atoms are stripped and the result is protons. These protons are then transferred to Linac 2 that accelerates them up to 50 MeV. Afterwards these protons are injected to the PSB.

The Proton Synchrotron Booster (PSB) is a circular accelerator with a 157 m circumference. It consists of four superimposed rings that accelerate the protons from Linac 2 up to 1.4 GeV. Then the protons can be injected to the ISOLDE Radioactive Ion Beam facility or to the PS.

The Proton Synchrotron (PS) is also a circular accelerator and can accelerate protons coming from the PSB as well as heavy ions coming from the Low Energy Ion Ring (LEIR). The PS has a circumference of 628 m and the protons can reach up to 25 GeV kinetic energy. After acceleration, the beam can be transferred to an another circular accelerator, the SPS or to the East experimental Area, the Antiproton Decelerator (AD) and to the neutron time-of-flight facility (nToF).

The Super Proton Synchrotron (SPS) ring has 7 km circumference and the protons can be accelerated up to 450 GeV. The beam of the SPS can be extracted to the EHN1, NA62 and COMPASS experiments in the North Area and to the AWAKE experiment. If the beam is not extracted to one of these experiments, it continues to the LHC and it can fill it at two different points, corresponding to clockwise and counter clockwise circulation in the LHC.

The Large Hadron Collider (LHC) [1] is the largest and most powerful circular accelerator with 27 km circumference. The particles move in opposite trajectories in two separate beam lines. The LHC is built in a tunnel, on average, 100 m under the earth surface and is designed to collide these two beams at 14 TeV, center of mass energy. There are four collision points and at each one of them there are huge detectors with different characteristics and study objectives. These detectors are briefly discussed to the next paragraph.

The ATLAS (A Toroidal LHC ApparatuS) [2] detector is situated at LHC point 1. It weights 7000 tons, has 22 m diameter and is 46 m long. It contains an inner detector, electromagnetic and hadronic calorimeters, muon spectrometers, a solenoid and also a toroidal magnet that produce 2T. The main goals of this general-purpose detector are the study of the Higgs boson, dark matter and extra dimensions.

At the LHC point 2 is located ALICE (A Large Ion Collider Experiment) [3] that is designed to detect the fragments of heavy ion collisions and to study the quark-gluon plasma phase. It is 26 m long with a diameter of 16 m and a weight of 10000 tons.

CMS (Compact Muon Solenoid) [4] is located at LHC point 5. It is the second general-purpose detector of LHC. It weights 12500 tons, is 22 m long with a 15 m diameter. The solenoid magnet creates a magnetic field of 4T. It has the same scientific study objectives like ATLAS. At 2012, the discovery of the Higgs boson was announced with data taken from the two detectors CMS and ATLAS.

In the LHC point 8 the LHCb (Large Hadron Collider beauty) detector is situated. The main goal of this detector is to study CP violation, the differences between matter and antimatter, by investigating the beauty-quark. It is a forward detecting spectrometer that has a length of 21 m, it is 10 m tall, has a width of 13 m and weighs 5600 tons [5].

1.4 Proton Synchrotron (PS)

The Proton Synchrotron (PS) started circulating the first proton beam on 24 November 1959. It was the first synchrotron of CERN. The PS has a circumference of 628 m and it accelerates protons injected from the PSB or heavy ions injected from LEIR. It consists of 100 magnetic units, each 4.4 m long, that provide dipole and quadropole magnetic fields. The PS can reach up to 25 GeV and has several extraction lines, such as the one to the SPS, to the AD, to the nToF and the one to the East Hall through the F61 beam

line. In the East Hall are located the Proton Irradiation Facility (IRRAD) and the CERN High energy AcceleRator Mixed field facility (CHARM) and they receive a beam with 24 GeV/c momentum. The Proton Synchrotron is presented in the Fig. 1.2 together with its extraction lines to the other experiments.

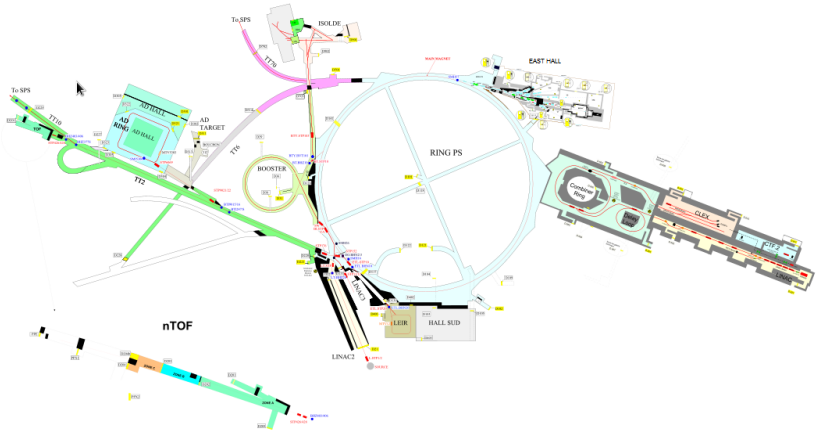

Figure 1.2: The Proton Syncrotron with its several extraction lines.

1.5 East Hall

The East Hall is an experimental area situated at the PS in the building 157. The primary proton beam from the PS is injected to the East Hall through the F61 line with 24 GeV/c beam momentum. This primary extraction line is then split to the F61N (North) line towards the north target and to the F61S (South) line. The beam passing through the F61N impacts on the north target and then the secondary particles produced pass through three beam lines, called T9, T10 and T11. The F61S goes to the T8 beam line. The T8 beam line is a primary beam line that transports the primary protons to the IRRAD and CHARM facilities with a 24 GeV/c beam momentum and where they finally impinge on the CHARM target. The T9, T10 and T11 lines are secondary beam lines that deliver secondary particles up to 15 GeV/c at a production angle of 0 degrees, up to 7 GeV/c at a production angle of 61.6 milliradians and up to 3.5 GeV/c at a production angle of 149.2 milliradians, to T9, T10 and T11 respectively. The East Hall is depicted in the following figure Fig. 1.3 with the different beam lines.

Figure 1.3: East Hall layout.

Chapter 2

CHARM

This chapter describes the CERN High energy AcceleRator Mixed field (CHARM) facility where the experiments for this thesis have been conducted.

2.1 General

The CERN High energy AcceleRator Mixed field facility (CHARM) [6] is located in the East Experimental Area that receives beam from the CERN Proton Synchrotron (PS). The scope of this facility is to test electronic components, mainly from the LHC, in well-known mixed radiation fields at different irradiation locations, more specifically to study the effects of radiation on the equipment in the frame of the R2E project [7–9].

The R2E project was established after observing considerable downtime of the CERN LHC as a result of Single Event Effects (SEE) in electronic equipment in the LHC tunnel that initiated the dumping of the beams in LHC. This case is presented in the Fig. 2.1. To achieve the goal of R2E project of 0.5 SEE induced beam dumps per 1 inverse femtobar of integrated luminosity delivered to ATLAS and CMS in 2015 after the Long Shutdown 1 (LS1), a thorough test campaign of electronic equipment, that was installed in the LHC tunnel, was needed. Therefore the CHARM facility was built in LS1, to be able to test electronic systems with dimensions of up to

1 m x 1 m x 2 m [10].

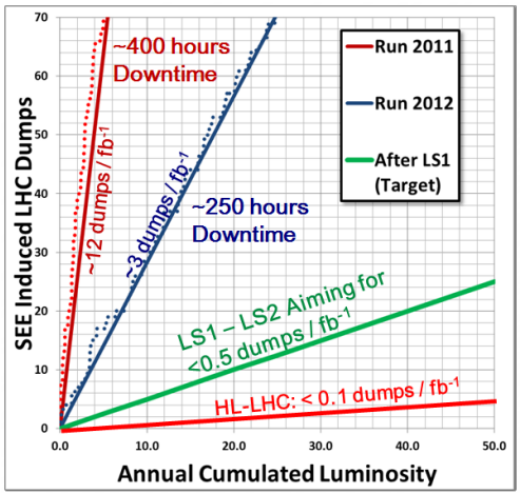

Figure 2.1: LHC beam dumps induced by Single Event Effects (SEE) in electronic equipment.

The CHARM facility can test the equipment under accelerator, ground, atmospheric (neutron energy spectra) and space radiation environments [11]. The location of the CHARM facility is indicated in Fig. 2.2.

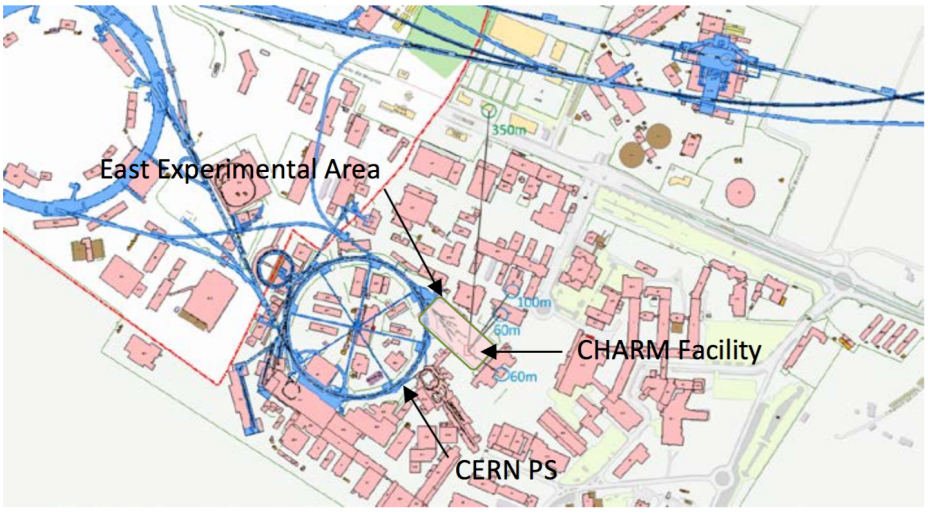

Figure 2.2: Location of the CHARM facility.

2.2 Layout & operational parameters

The CHARM facility receives the proton beam from the CERN PS through the F61S and then the T8 beam-line in the PS East Experimental Area. The beam crosses first IRRAD, a direct proton irradiation facility that is upstream of CHARM and then impacts on the CHARM target. The beam that comes from the PS has a momentum of 24 GeV/c with 5×10^{11} protons per pulse with a pulse length of 350 ms and with a maximum average beam intensity of 6.7×10^{10} p/s [12].

The CHARM facility is surrounded by concrete and iron shielding [13] in order to decrease the radiation outside of the facility to optimized levels. The irradiation room, where the target is located, is big enough so that cumbersome and entire systems can be tested at the irradiation locations. The layout of the facility from the top as well as the target location is shown in the Fig. 2.3.

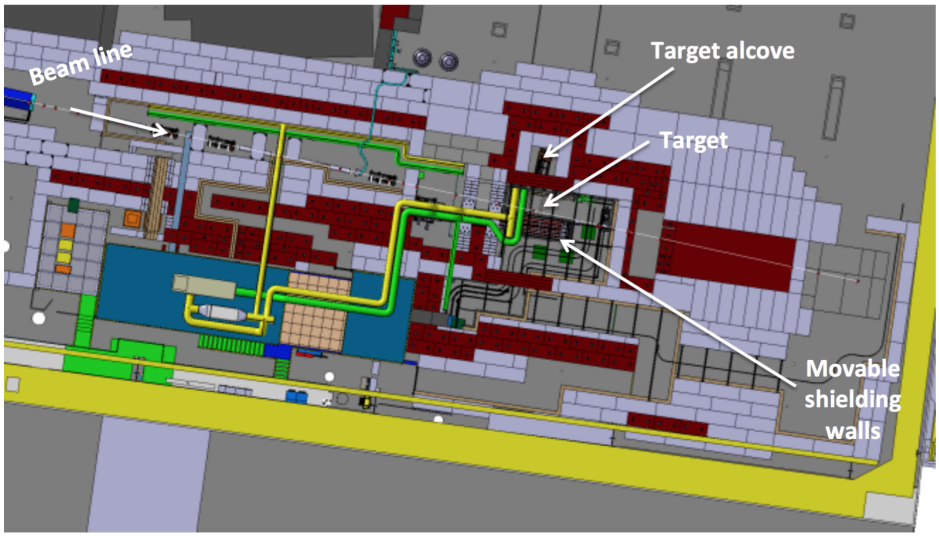

Figure 2.3: Layout of the CHARM facility.

Inside the target room there are four movable shielding walls, with an individual thickness of 20 cm, two made out of concrete and two out of iron. They can be placed between the target and some of the irradiation positions in variable arrangements, so that the test spectra are adjusted to the desired

radiation field (energy and intensity) during the tests. The movable shielding walls are presented in the Fig. 2.4.

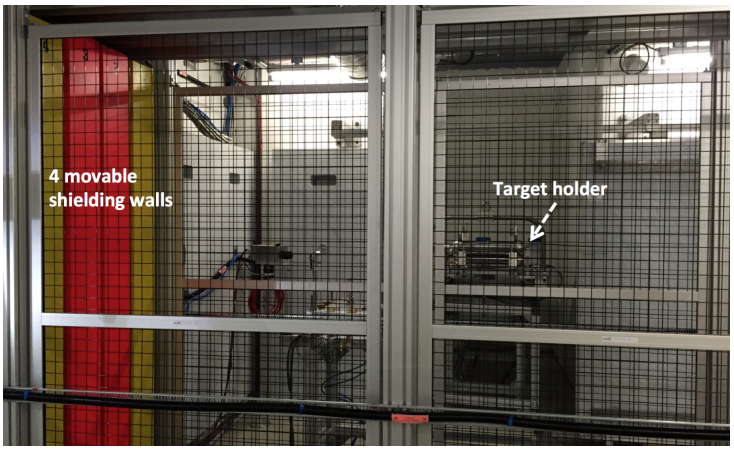

Figure 2.4: A photo taken at an irradiation location of the CHARM target room with the target holder and the four movable shielding walls retracted from the facility. These four shielding walls can be moved individually between the irradiation location and the target.

2.3 Beam parameters & instrumentation

2.3.1 Beam specification

The CHARM facility receives a pulsed proton beam from the CERN PS with a beam momentum of 24 GeV/c. The maximum pulse intensity is 5×10^{11} protons per pulse and the beam is structured in spills (pulses) with a maximum length of 350 ms. The spills are separated by at least 2.4 seconds. When the facility is operating under nominal conditions, the facility receives 2 spills per 45.6 seconds and the average proton beam intensity on target is 2.2×10^{10} p/s. There is also the possibility of reaching up to 6 spills per 45.6 seconds with 6.7×10^{10} p/s maximum proton beam intensity on target, only when CHARM is the only user of beam cycles of the PS in the East Experimental Area [14].

2.3.2 Beam position and size monitoring

To measure the size and the position of the beam, several monitors are used such as the BPM (Beam Position Monitor) when the beam crosses the IRRAD facility, the BTV (Beam TV) and the MWPC (Multi-wire Proportional Chamber) when it crosses CHARM. The MWPC can be used to check the beam size and the position of the beam and the BTV is used to confirm the precision of the beam position after the implementation of changes on the T8 beam line. The values of these monitors are also registered and are available via TIMBER (user interface to the LHC Logging System).

2.3.3 Beam intensity monitoring

The beam intensity can be estimated by two Secondary Emission Chambers, denoted SEC1 and SEC2, and as well as by Ionisation Chamber (IC). At the CHARM facility the SEC1 is used to verify the number of protons on the target (POT). The calibration of the SEC1 is done using the 'fast beam current transformer' (BCT) that is located right after the PS extraction point. Moreover this has been cross checked by foil activation.

An intensity calibration factor of 1.87×10^7 p/count has been established for the SEC1 and has to be applied to the counts per pulse to obtain the number of protons per pulse. This calibration factor had been obtained with aluminium foil activation using sodium isotopes with a statistical uncertainty of 7% from the γ-spectrometry measurement [15] and can be used to easily compare experimental measured quantities with quantities estimated by FLUKA (FLUktuierende KAskade, a Monte Carlo simulation code) [16, 17] calculations.

Although the SEC2 can be used as well to measure the POT, is not a preferred option because this chamber is located after the IRRAD facility and the secondary radiation from the samples placed in IRRAD can affect the signal of the chamber. The measurement values of SEC1, SEC2 and IC are logged in a database they are accessible via TIMBER.

2.4 Targets

There are three different targets that can be used in CHARM, a copper, an aluminium and an aluminium sieve target. In addition, there is the option of having no target in the beam. The 3 targets are placed on a target holder as shown in Fig. 2.5. The target holder can move back and into the beam line and can be retracted to the target alcove when there is an access to the facility. One target is chosen at a time based on the requested intensity radiation field which can vary a factor of 3 among the different targets resulting in a total decrease in the primary radiation field by a factor of 10. The copper target is the one that gives the highest intensity and the aluminium with sieve the lowest. All the targets are cylinders that are 50 cm long with a diameter of 8 cm.

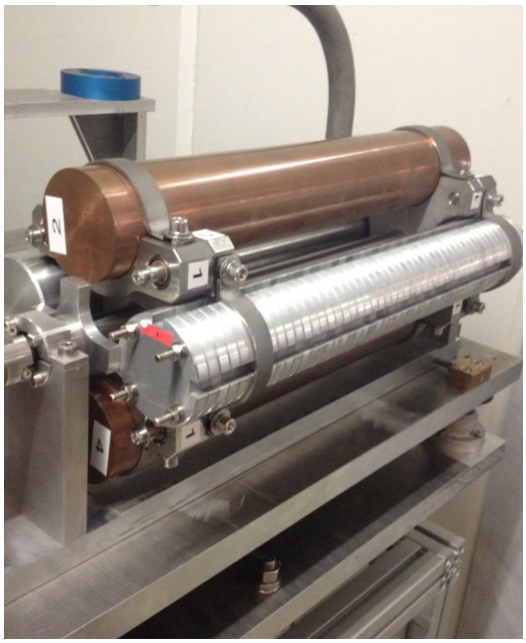

Figure 2.5: That photo shows 2 copper targets and the aluminium with sieve target on the target holder. One of the two copper targets has been currently removed from the target holder.

2.5 Radiation fields

The primary proton beam comes from the PS with a 24 GeV/c momentum and impinges on the CHARM target. The particles that are produced after the beam impacts on the target are a shower of secondary particles such as protons, neutrons, pions, kaons, electrons, positrons, muons and photons with a large amplitude of energies up to 24 GeV. Because of this fact, the radiation field is called 'mixed' inside the CHARM facility. Because of the thick concrete shielding around and top of the facility, the majority of particles that are escaping from the shielding are neutrons, photons, and muons in forward direction.

Due to the multiple and alternative modes of operation of this facility, the radiation field that occurs has a large variation in the particle and energy spectra at the various test locations. The FLUKA Monte Carlo code is used to simulate the radiation fields for different configurations of the facility, using the correct parameters and geometry of the facility. From the results of these simulations the radiation spectra for the test locations are estimated and then used for the calculation of useful quantities referred to the testing of electronics.

2.6 Radiation protection assessment approach

Furthermore, FLUKA was used for the shielding design of the CHARM facility as well as in the radiation protection assessment of the finally adapted design, estimating the prompt radiation, the residual radiation and the activation of air and the radiological impact of its subsequent release to the environment [10].

2.6.1 Prompt radiation

The shielding of the CHARM facility has been designed to respect the CERN Radiological Area classification so that the ambient dose equivalent

rates should be below 3 μSv/h for the control rooms inside the East Hall and less than 15 μSv/h (low occupancy area) at 40 cm outside from the shielding walls for the maximum average beam intensity of 6.7×10^{10} protons per second. Moreover, the ambient dose equivalent rates have to be below 2.5 μSv/h outside of the hall for the maximum average beam intensity. These prerequisites determined the optimized design of all shielding passages (access chicanes, ventilation ducts, cable ducts). Additionally, the locations of the area monitors have been chosen to verify the compliance with these area classification limits.

Furthermore, the shielding had to be designed so that the annual effective dose to members of the public, both coming from prompt radiation (neutron sky-shine) and from releases of air-borne radioactivity to the environment, is below the design goal of 1 μSv for the nominal annual protons on target.

In total, approximately 2000 tons of iron and 4000 tons of concrete have been used for the shielding structure. The design had also to accommodate the fact that design choices were limited due to the presence of existing facilities in the East Experimental Area.

Monte Carlo simulations with the FLUKA code [16, 17] have been performed to estimate the prompt ambient equivalent dose rate levels for the CHARM facility. The prompt ambient equivalent dose rate is shown at the beam-line level in Fig. 2.6 and at 40 cm above the top of the shielding roof in Fig. 2.7, demonstrating the agreement of the shielding design with the design goals with respect to the CERN Radiological Area classification.

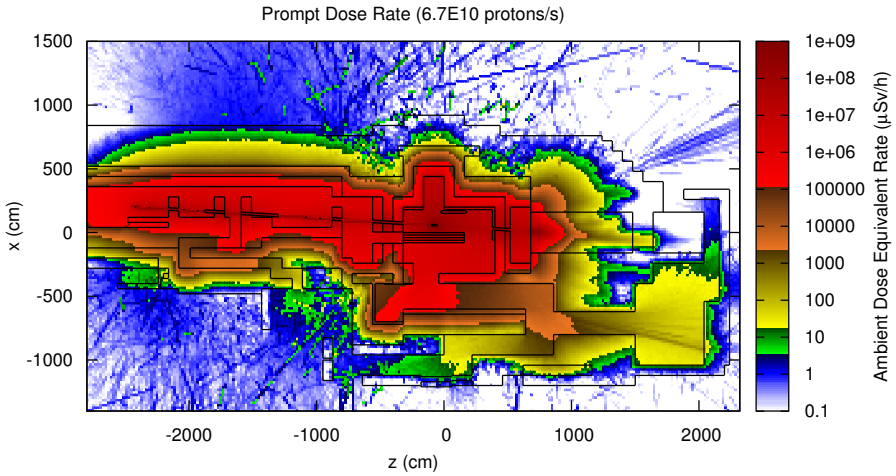

Figure 2.6: Prompt radiation for the maximum beam intensity at beam-line level with color-coded area classification (blue covering the acceptable control room levels and green the acceptable low occupancy area levels).

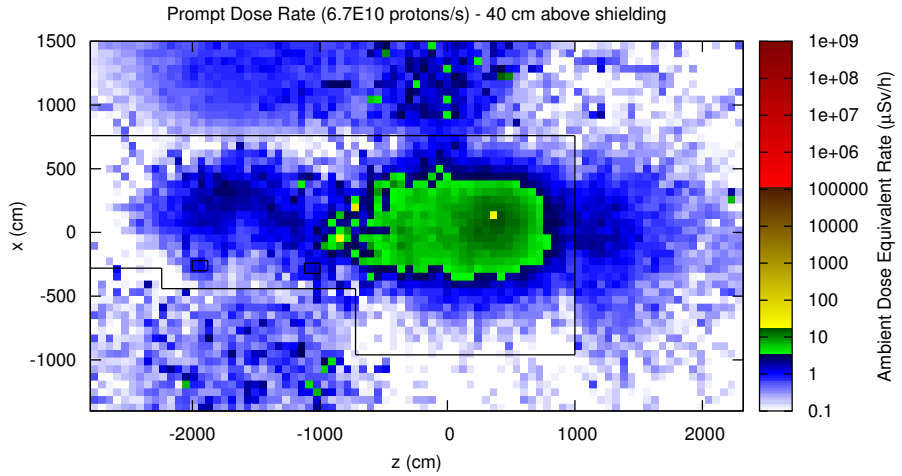

Figure 2.7: Prompt radiation for the maximum beam intensity at 40 cm above the shielding roof with color-coded area classification (blue covering the acceptable control room levels and green the acceptable low occupancy area levels).

2.6.2 Residual radiation

The reduction of the residual ambient radiation levels is an important optimization following the ALARA principle. In addition, reducing the residual ambient radiation levels to lower the effective dose to personnel during interventions minimizes also the administrative requirements for the interventions and, as a consequence, results in a more efficient exploitation of the facility.

To predict the ambient dose equivalent rate levels for various operational scenarios and cool-down times, Monte Carlo simulations have been performed with FLUKA and the DORIAN code [18]. The ambient dose equivalent rate levels for 200 days of operation with maximum beam intensity followed by cool-down periods of 1 hour and 1 day are presented in Fig. 2.8.

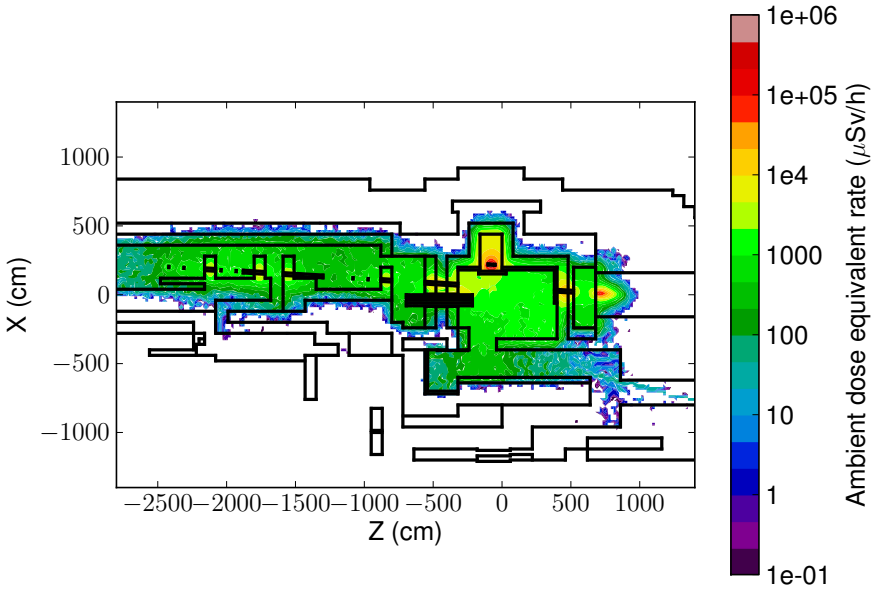

(a)

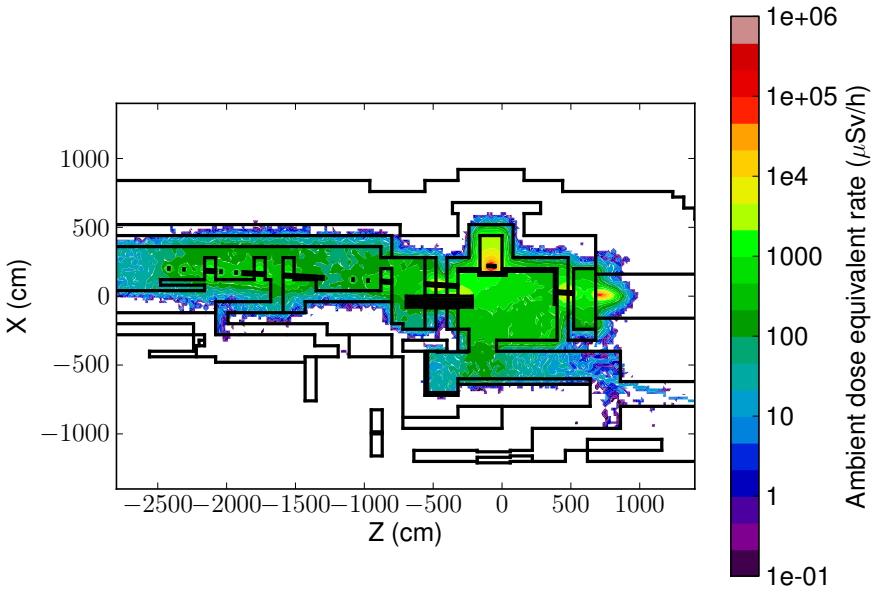

(b)

Figure 2.8: Residual radiation levels after 200 days of operation with maximum beam intensity followed by 1 hour (a) and 1 day (b) of cool-down.

2.6.3 Air activation and subsequent release to the environment

The operation of the CHARM facility results in the activation of the air inside the facility. The following methodology has been used to obtain the radionuclide concentrations, the annual release to the environment and the resulting annual effective dose to members of the public:

1. The track-length spectra for protons, neutrons and charged pions have been scored in the air volumes inside the CHARM facility (and the upstream proton facility) in the FLUKA Monte Carlo simulation.

2. The obtained track-length spectra have been folded with a dedicated set of air activation cross sections [19, 20] to estimate the radionuclide production yields.

3. The radionuclide concentrations in the facility and the release term to the environment have been calculated from the radionuclide production yields taking the time evolution and the characteristics of the ventilation circuit into account.

4. The radionuclide concentrations in the facility after beam stop have been converted to the committed effective dose due to inhalation without flush for a 1 hour access by application of exposure-to-dose conversion coefficients for inhalation [21]. The decrease of the radionuclide concentrations due to decay during the 1 hour period has been taken into account.

5. The release term has been converted to the effective dose to members of the public by application of release to effective dose conversion coefficients, computed with a dedicated Monte Carlo integration program EDARA [22].

In order to meet the design goal that the committed effective dose due to inhalation has to be less than 1 μSv for a 1-hour access, dynamic confinement

with a flush before access has been chosen. To achieve that the effective dose to members of the public to be less than 1 μSv per year (both from prompt radiation and from releases to the environment), the effective dose to members of the public has been calculated as a function of the air tightness, which corresponds to the extraction rate to ensure the dynamic confinement, of the facility. The achieved air tightness of the CHARM facility ensures that the annual effective dose to any member of the public does not exceed 1 μSv

2.7 CERN Shielding Benchmark Facility(CSBF)

The shielding of the CHARM facility also includes the CERN Shielding Benchmark Facility (CSBF) [10] situated laterally above the target. The primary goal of the CSBF is the characterization of the shielding properties of various materials and deep shielding penetration studies, made feasible because of the high beam intensity, for detector calibration, detector inter-comparison studies and activation. It can make parasitic use of the radiation field emerging from the beam impacting on the CHARM target.

The commissioning, characterization and exploitation of the CSBF is the main topic of this thesis, see the following chapters 5, 6, 7, 8 and 9. In each of these chapters are explained the motivation of the CSBF, the activation campaign in 2015, the CSBF upgrade, the commissioning of the upgraded CSBF and the activation campaign in 2016 and finally the study of experimental attenuation factors for different shielding materials for deep shielding neutron penetration.

Chapter 3

Neutron attenuation & activation

This chapter describes the basic properties of the neutron and then specifically neutron attenuation and activation.

3.1 General

Neutrons are subatomic particles. Together with protons are called nucleons and they are a component of the nucleus of an atom. The neutron does not have an electrical charge and its mass is $939.56\,\mathrm{MeV}/c^2$, slighter heavier than a proton ($938.27\,\mathrm{MeV}/c^2$). It also consists of three quarks, one up quark and two down quarks. The free neutron is unstable with a mean lifetime of about 15 minutes ($880.2 \pm 1.0\,\mathrm{s}$). Because of its mass, it can decay into a proton, an electron antineutrino and an electron. This radioactive decay is named β^- decay [23].

3.2 Nuclear interactions

When a particle hits a nucleus an elastic or an inelastic processes can occur. During an elastic scattering, the character of the particles as well as their kinetic energy is preserved and only their direction is changed. In inelastic scattering, the kinetic energy of the system is not conserved. The

difference in kinetic energy can be used to excite a nucleus or to produce new kind of particles. Inelastic scattering can contribute to induced activity only if the new particles produced are unstable [24].

Charged particles can interact with the nucleus, apart from the quantum mechanical tunnel effect, only if they reach a specific energy that is needed to overpass the Coulomb barrier of the nucleus. In contrast, particles with no charge like neutrons will not be pushed away from the nucleus by the electrostatic Coulomb force. When a nucleus absorbs a neutron and a γ ray is emitted then this reaction is called radiative capture. This reaction is more probable when the kinetic energy of the neutron is low, e.g. when the neutrons are thermal (0.025 eV) or slow.

Another reaction that can take place once more with thermal and slow neutrons is when a light target nucleus absorbs a neutron and then a proton or an α particle can be ejected from the nucleus, (n,p) or (n,α) accordingly when the required threshold is overpassed. The nucleus can decay through the emission of a γ ray. For heavier nucleus higher kinetic energy of the neutrons is needed.

For fissile nucleus e.g. ^{235}U, ^{239}Pu, fission can occur also at thermal neutron energies. This means that a heavy nucleus can absorb a neutron, then becomes unstable and breaks in two or more fragments and additionally neutrons.

At energies from a few MeV up to about 50 MeV various types of nuclear reactions can occur. The particles that enter the nucleus can dislocate one or more nucleons, or even a part or fragment of the target nucleus. For instance a proton can be absorbed by the nucleus and excite the nucleus, then one or more nucleons can be emitted with a relatively low kinetic energy, called evaporation. Some of the possible proton and neutron evaporation reactions are the following (p,n), (p,pn), (p,2n), (p,p2n), (p,α) and (n,p), (n,pn), (n,2p), (n,n2p), (n,α).

At higher energies, the process is more complex. When the nucleons are hit by the incident particles in the target atom, they can gain enough

energy so that they can move through the nucleus and strike other nucleons of the same atom. This procedure generates an "intranuclear" cascade of fast nucleons. Finally, the nucleons can either escape from the nucleus or be captured and give all their energy to excite the whole nucleus. A much wider variety of new nuclei can be formed in this way.

Other mechanisms observed at high energies are spallation or high energy fission. Direct ejection of high energy ions or light nuclei, called fragmentation reactions are also observed. A possible result for an incident or an intranuclear cascade particle can be the production of new particles by high energy nucleons striking other nucleons or target nuclei. In this group of newly generated particles, nucleons and antinucleons are able to develop intranuclear cascades in their turn, and eventually transfer their total energy to nucleons in the target nucleus, hence raising the number of all possible products from the nuclear reaction.

There are also other kind of reactions called photonuclear. In these ones, a photon (γ) is absorbed by a nucleus, exciting the nucleus that finally emits one or more nucleons. Some of the photonuclear reactions are (γ,n), (γ,2n), (γ,p) and (γ,α). The threshold level for (γ,n) for most nuclei is around 10 MeV .

3.2.1 Neutron interactions

Neutrons have no charge, thus they cannot interact in matter with the Coulomb force. When a neutron interacts, it is with a nucleus of the absorbing material. As a consequence, the neutron creates secondary particles or the neutron energy or direction is significantly changed [25].

In contrast to photon interactions, the products resulting from neutron interactions are almost always heavy particles. These particles can result from neutron-induced nuclear reactions or can be the nuclei of the absorbing material itself, which have gained energy from neutron collisions.

Neutron reactions are summarized in Tab. 3.1 for different neutron energy ranges.

Table 3.1: Nuclear reactions [24], [26].

Thermal and slow neutron reactions ($\preceq 10$ MeV)	
Elastic scattering X(n,n)X	One of the main mechanisms of energy loss for neutrons up to 1 MeV. The linear momentum and kinetic energy of the system are conserved, however, the neutron can give part of its energy to the recoil nucleus.
Inelastic scattering X(n,n')X* (without nature change of interacting particles)	A neutron is absorbed by a nucleus and then a compound nucleus is formed emitting a secondary neutron of lower kinetic energy. The nucleus left in an excited state, may decay with a γ-ray emission. In order that the excitation of the nucleus takes place, the neutron must have energy higher that 1 MeV.
Radiative neutron capture ${}^{A}_{Z}X(\mathrm{n},\gamma){}^{A}_{Z-1}X$	A neutron hits and enters a nucleus, the nucleus get in an excited state and then returns to its ground state by γ emission. The radiative capture is more feasible to happen when there are thermal and slow neutrons.
Particle ejection X(n,x)Y x=p,α	When a neutron is absorbed, the energy of the excitation level of the nucleus is high enough to knock away a proton or an α particle. The remaining nucleus can continue to be in an excited state and can decay through γ emission. The particle ejection can occur when neutrons are thermal and slow and for light target nucleus.
Fission (n,f)	Fission can happen at thermal energies when a heavy nucleus absorbs a neutron and is divided into two or more fragments and additionally neutrons.
Medium energy reactions (few MeV up to $\sim$ 50 MeV)	
Evaporation X(i,j)Y i=p,n j=n,p,2n,d,α,...	The energy is high enough for an incoming proton to be absorbed by the nucleus and form an excited nucleus. Later, the energy is released by ejecting one or more nucleons or even heavier particles, each with relatively low kinetic energy. This process leaves the nucleus in an excited state that gives off the energy by γ emission. Evaporation reactions can be induced also by neutrons.
High energy reactions (>several tens of MeV)	
Spallation of high energy hadrons X(i,x_1n + x_2p + ...)Y i=p,n,$^{+}\pi$,$^{+}\pi$, ... $x_{1,2...} \in N_0$	An excited nucleus, hit by a hadron with relatively high energy decays by evaporation of several particles (n, p, π, d, α...). So, a large number of light particles are emitted, resulting to a target residue lighter than the original nucleus and generally unstable. Some of the nucleons hit by the incident particle may be directly emitted from the nucleus with relatively large kinetic energy. The rest of the nucleons make secondary collisions with nucleons of the same nucleus before escaping or being caught by it (intranuclear cascade). The secondaries ejected during the spallation reaction may have enough energy to induce further reactions, such as start a hadronic shower. One of the most typical feature of spallation reactions is the emission of many light fragments, mostly neutrons. The excited nucleus can also be de-excited through another process called high energy fission.

The probabilities of the various kinds of neutron interactions change with neutron energy. In the subsections 3.2.1 and 3.2.1 below, neutrons are divided in two categories based on their energy, slow neutrons and fast neutrons. The dividing line is the cadmium cut off energy at about 0.5 eV.

Slow neutron interactions

The important interactions, for slow neutrons, are elastic scattering with absorber nuclei and a large set of neutron-induced nuclear reactions. Due to their small kinetic energy, very little energy can be transferred to the nucleus in elastic scattering. Elastic collisions can have large cross sections and they often bring slow neutrons into thermal equilibrium with the medium of the absorber before another kind of interaction occurs. A big part of the population in the slow neutron energy range is found among thermal neutrons that they have an energy of about 0.025 eV at room temperature.

The slow neutron interaction of big interest are the neutron-induced reactions that can create secondary radiation of sufficient energy to be detected

directly. For the reason that the incoming neutron energy is low, all reactions must have a positive Q-value to be energetically possible. The radiative capture or (n,γ) reaction is the most probable and very critical in the attenuation or shielding of slow neutrons. This reaction can be used for indirect detection of neutrons using activation foils. Reactions like (n,α), (n,p) and (n,fission) are preferred for active neutron detectors because the secondary radiations are charged particles.

Fast neutron interactions

With increasing neutron energy the importance of scattering becomes greater for detection purposes because the neutron can transfer a considerable amount of energy in one collision. In that instance, the secondary radiations are recoil nuclei that have a detectable amount of energy deriving from neutron collisions. At every scattering the neutron loses energy and so is moderated or slowed to lower energy. The most efficient moderator is hydrogen because the neutron can lose up to all its energy in a single collision with a hydrogen nucleus. When the nuclei are heavier only a partial energy transfer is feasible.

If the energy of the fast neutron is adequately high then inelastic scattering with nuclei can occur, in which the recoil nucleus is raised to one of its excited states during the collision. With the emission of a γ ray the nucleus quickly de-excites and the neutron loses a greater fraction of its energy than it would in an elastic collision. Inelastic scattering and the successive γ ray emission play a leading role in the shielding of fast neutrons but are an undesirable effect in the response of most fast neutron detectors that are based on elastic scattering.

3.2.2 Neutron cross sections

Neutrons of a fixed energy have a probability per unit path length that any interaction will occur. This probability is expressed as *cross section* σ per nucleus for each kind of interaction. The unit of cross section is the unit

of area. Cross sections are often expressed in *barns* (10^{-28} m^2). For instance, at given neutron energy neutrons will have an elastic scattering cross section, a radiative capture cross section and so on, each of which will be a function of the neutron energy [25].

When the cross section σ is multiplied by the number of nuclei N per unit volume, it results into the macroscopic cross section Σ.

$$\Sigma = N\sigma \tag{3.1}$$

Σ has the inverse length as unit and demonstrates the probability per unit path length for the specific process described by the "microscopic" cross section σ. Σ_{tot} is the probability per unit path length that any type of interaction will occur when all processes are combined by adding together the cross sections for each particular interaction.

$$\Sigma_{tot} = \Sigma_{scatter} + \Sigma_{rad.capture} + ... \tag{3.2}$$

In a narrow beam attenuation experiment for neutrons, the number of detected neutrons will decrease exponentially with the absorber thickness. Then the attenuation equation is shown in Eq. 3.3.

$$\frac{I}{I_0} = e^{-\Sigma_{tot}t} \tag{3.3}$$

The neutron mean free path λ is given by the $1/\Sigma_{tot}$. For slow neutrons in solid materials, λ can be approximately a centimeter or less, although for fast neutrons in solid materials the λ can be tens of centimeters.

Nevertheless, in most of the cases neutrons are not narrowly collimated so the typical shielding simulations include a broader beam or "bad geometry" conditions. That means, that Eq. 3.3 does not give a sufficient description, because of the added importance of scattered neutrons. For this reason, a more complex neutron transport estimation is needed to predict the number of transmitted neutrons and their distribution in energy. When dealing with the rate of reactions induced by neutrons, it is more useful to use the neutron

flux. First we have to take into account neutrons with single energy or fixed velocity ν and Σ the macroscopic cross section then the product $\nu{\cdot}\Sigma$ shows the interaction frequency for the process. The reaction rate density (reactions per unit time and volume) is given by n(r)$\cdot\nu\cdot\Sigma$, where n(r) is the neutron number density at the vector position r, and n(r)$\cdot\nu$ is the neutron flux $\phi(r)$ with units of length^{-2}time^{-1}. Hence, the reaction rate density is the product of the neutron flux and the macroscopic cross section for the specific reaction, see Eq. 3.4.

$$reaction\,rate\,density = \phi(r)\Sigma \tag{3.4}$$

Eq. 3.4 can be generalized so that combines an energy dependent neutron flux $\phi(r, E)$ and cross section $\Sigma(E)$, see Eq. 3.5.

$$reaction\,rate\,density = \int_0^\infty \phi(r, E)\Sigma(E)dE. \tag{3.5}$$

Spallation cross sections

The nuclear cross section for spallation reaction approaches the geometric cross section of the nucleus at high particle energies. A review of nuclear interaction cross section suggests an empirical dependence of the interaction cross section, σ, on the atomic mass of the target nucleus A

$$\sigma = 42\ A^{2/3} \times 10^{-3}\ \text{(barn)} \tag{3.6}$$

which is a good approximation for the cross section for an inelastic collision by a hadron of energy greater than about 120 MeV [27]. The formula is valid for proton or neutron induced spallation. This cross section is plotted in units of barns (1 barn = $10^{-24}\,\text{cm}^2$) as a function of atomic weight of the target nucleus in Fig. 3.1. High-energy particle nuclear interaction cross sections for common target materials are listed in Table 3.2.

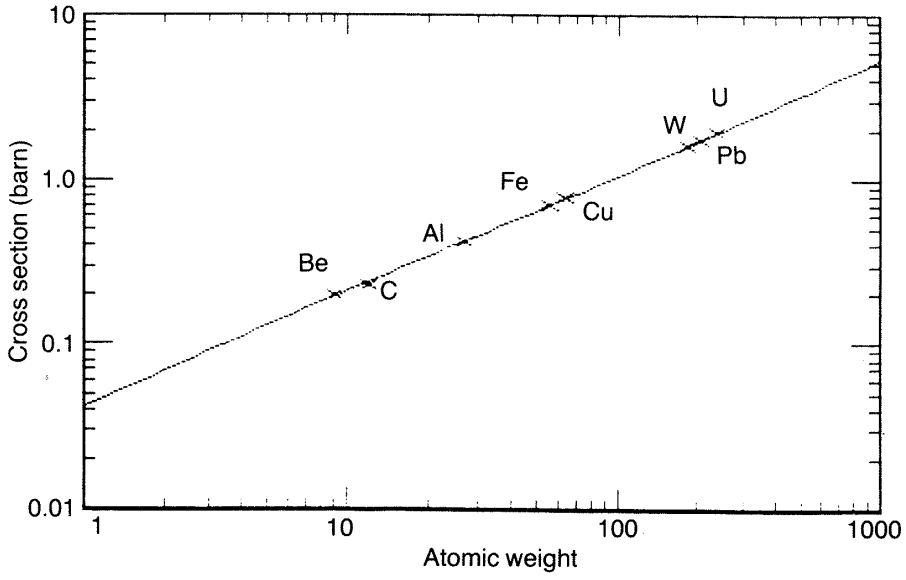

Figure 3.1: The nuclear inelastic cross section in the high energy limit as a function of atomic weight of the target nucleus in units of barns [27].

Table 3.2: Nuclear inelastic cross sections in the high energy limit in various target materials [27].

Material	Inelastic Cross Section (barn)	Nominal density ($g\,cm^{-3}$)
Beryllium	0.20	1.8
Graphite	0.23	2.0
Aluminium	0.42	2.7
Iron	0.70	7.4
Copper	0.78	8.9
Tungsten	1.61	19.3
Platinum	1.78	21.4
Lead	1.77	11.3
Uranium	1.98	19.0

3.3 Neutron attenuation

When there are interactions by primary protons of energy less than 1 GeV, the average secondary particle energy will be less than 120 MeV and then their attenuation mean free path in the shielding varies with energy. Experimental data of the attenuation mean free paths of radiation in concrete exposed laterally to secondary radiation from proton interactions have been reviewed and compared with calculated values. These mean free paths are expressed as a proportion of the limiting value at high energies, λ_0 [27].

The neutron attenuation length is shown in Fig. 3.2 for concrete and mono-energetic broad beam conditions. The attenuation length reaches a value of approximately 117 g/cm^2 above 200 MeV. As the cascade through thick shielding is driven by the high-energy particles, this value is equal to the equilibrium attenuation length at 90 degrees in concrete [28, 29].

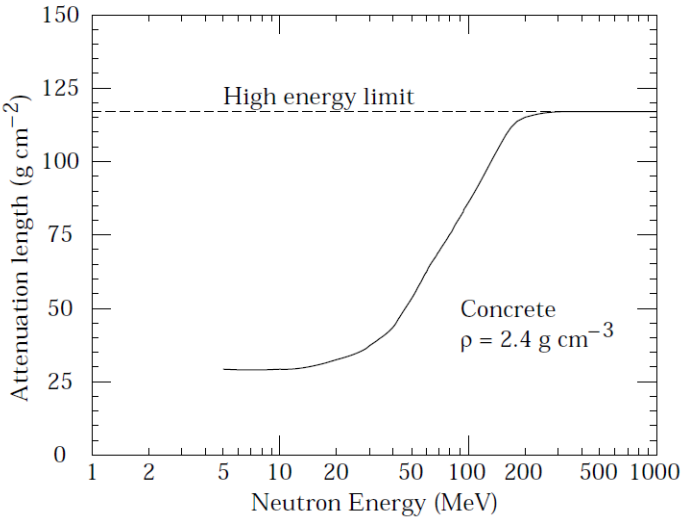

Figure 3.2: The variation of the attenuation length for mono-energetic neutrons in concrete as a function of neutron energy [29].

3.4 Neutron activation

When components at accelerators are exposed directly to the beam or to stray radiation, they may become radioactive decaying by gamma-rays, beta particles and rarely neutrons. The induced radioactivity produced when the accelerator is under operation remains after the accelerator has stopped operating, often for several years. It is one of the risks to the intervening personnel and demands serious restrictions on the accessibility of activated equipment for operation, maintenance, repairs and decommissioning purposes after the shutdown.

3.4.1 Properties of induced radioactivity

If a high-energy hadron interacts with a nucleus, neutrons, protons and other nuclear fragments can be emitted, converting the struck nucleus to that of a different nuclide, which might be radioactive. Some of the secondary particles emitted in an interaction may have sufficient energy to continue and cause additional activation and therefore provoking a nuclear particle cascade. In this process, many nuclei are produced in excited states and de-excite by emitting neutrons, charged particles or fragments (that can be in an excited state as well) in a so called "evaporation" process, or they may de-excite by emitting photons. The process can continue and radionuclides can be produced till the energies of the particles fall below the thresholds for the nuclear reactions concerned or, in the case of exothermic reactions, until they are captured.

Albeit the total amount of radioactivity induced in an accelerator will depend on the primary beam loss, the likelihood of generating a particular radionuclide will also depend on the composition of the material struck, the spectrum of secondaries produced and the production cross section of the isotope concerned. The amount of radionuclides present at any given time will also depend on the radionuclide half-life and the time that the accelerator has been in operation, as well as on the time that the activity has had to decay

since operation stopped. Therefore, the estimation of induced radioactivity in an accelerator is a complicated process [27].

3.4.2 Estimation of induced radioactivity

Generally, induced radioactivity can be generated at all accelerators that produce particles above the reaction threshold of the activation process of interest. When the accelerated beam hits a nucleus, the resulting nuclear reactions can generate a different nuclide, which may or may not be radioactive.

The most simple activation situation at accelerators is that of fixed irradiation of some material by a spatially uniform flux density of particles that begins at time $t = 0$ and continues at a constant rate for an irradiation period that ends at $t = t_i$. This is followed by a decay period called the cooling time t_c, a period of time that begins at $t = t_i$ and ends at $t = t_i + t_c$. For this simple situation, self-absorption of the hadrons by the target is ignored, as is the fact that a whole energy spectrum of particles might be incident. Hence, the process of producing the radioactivity is characterized by a single average cross section factor σ. In the more complicated generalized situations the value of this cross section must be obtained from averaging over the energy spectra of the incident particles [30].

The number of atoms of the radionuclide of interest per unit volume, in the absence of decay chains, will thus be governed by the following equation during the irradiation period:

$$\frac{dn(t)}{dt} = -\lambda n(t) + N\sigma\phi \tag{3.7}$$

where $n(t)$ is the number density of atoms (cm^{-3}) of the radionuclide of interest at time t, λ is the decay constant (s^{-1}), N is the number density of "target" atoms (cm^{-3}), σ is the production cross section (cm^2) and ϕ is the flux density ($\mathrm{cm}^{-2}\,\mathrm{s}^{-1}$) of the incident particles. On the right hand side of this equation, the first term represents the loss of radionuclides through

decay during the irradiation while the second term represents the increase of radionuclides through the production reaction under consideration. The equation has the following solution for $0 < t < t_i$:

$$n(t) = \frac{N\sigma\phi}{\lambda} \{1 - \exp(-\lambda t)\} \tag{3.8}$$

The specific activity induced in the material as a function of time during the irradiation is given by $a(t) = \lambda n(t)$, hence

$$a(t) = N\sigma\phi \{1 - \exp(-\lambda t)\} \ (\text{Bqcm}^{-3}) \quad \text{for} \quad 0 < t < t_i \tag{3.9}$$

When the irradiation reaches to an end ($t = t_i$), the specific activity will be

$$a(t_i) = N\sigma\phi \{1 - \exp(-\lambda t_i)\} \ (\text{Bqcm}^{-3}) \tag{3.10}$$

so that the specific activity as a function of time is characterized by a buildup from zero towards the saturation value equal to $N\sigma\phi$ for an infinitely long irradiation. After the irradiation has stopped ($t > t_i$), the specific activity as a function of the cooling time, $t_c = t - t_i$, will obviously decay exponentially and is defined by the activation equation:

$$a(t_c) = N\sigma\phi \{1 - \exp(-\lambda t_i)\} \{\exp(-\lambda t_c)\} \ (\text{Bqcm}^{-3}) \tag{3.11}$$

The activity evolution for four radionuclides as function of the irradiation and cooling time is shown in Fig. 3.3.

Activation formalism

In more complex cases including decay chains, the formalism has to be extended.

The specific activity of a radionuclide b induced by a loss rate of one

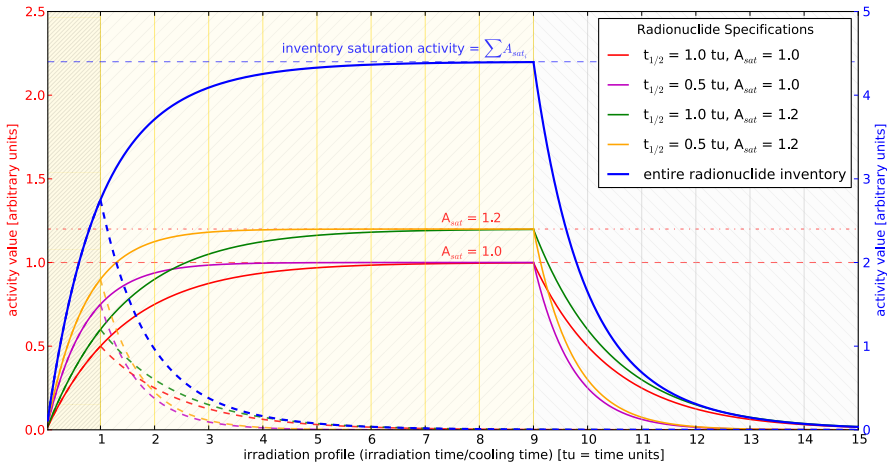

Figure 3.3: Activity evolution of an radionuclide inventory of four radionuclides with different half-lives and production yields as function of the irradiation and cooling time. The irradiation profile of nine half-life periods of irradiation time and up to six half-life periods of cooling time are illustrated in the graph. The dashed lines indicate an irradiation profile of one half-life period of irradiation time and up to 14 half-life periods of cooling time [31].

primary beam particle per second can be described as

$$A_b = \sum_r \sum_e T_{br}\ P_{re}\ m_e \tag{3.12}$$

where m_e stands for the weight fraction for the element e, r shows all the radionuclides that are directly produced from the elements of the material [32]. The matrix T_{br} indicates the time evolution and is defined in a following equation (see Eq. 3.14).

The production rate of an radionuclide r from an element e for a loss rate of one primary beam particle per second is given by the matrix

$$P_{re} = \frac{N_A}{M_e} \sum_{i=\mathrm{p,n},\gamma,\pi^+,\pi^-} \int \Phi_i(E)\, \sigma_{i,e,r}(E)\, dE \tag{3.13}$$

where N_A is Avogadro's constant and M_e is the atomic weight for the element e. The sum is extended over protons (p), neutrons (n), charged pions (π^+, π^-)

and photons (γ). With this definition the natural isotope abundances for each element e are taken into account, i.e. the cross section $\sigma_{i,e,r}(E)$ is an abundance weighted average of the cross sections of each isotope of element e. Additionally, $\Phi_i(E)$ is the radiation fluence for the various secondary particles ($i = \mathrm{p}, \mathrm{n}, \gamma, \pi^+, \pi^-$) generated by one primary beam particle per second. The expression $\sum_e P_{re}\, m_e$ corresponds to the production rate of the radionuclide r in the entire component for a loss rate of one primary beam particle per second.

The time evolution of the specific activity of radionuclide b, i.e. the build–up of radionuclide r and the full decay chain leading to radionuclide b, is explained by the matrix T_{br}. For an irradiation profile of a constant irradiation period of duration t_{irr} followed by a cooling time of duration t_{cool}, the time evolution T_{br} will be

$$\begin{aligned} T_{br}(t_{irr}, t_{cool}) &= \sum_{c,r\to b} \int_0^{t_{irr}} \sum_{m=1}^{j_c} c_m^c \, e^{-\lambda_m^c \, ((t_{cool}+t_{irr})-t_0)} \, dt_0 \\ &= \sum_{c,r\to b} \sum_{m=1}^{j_c} \frac{c_m^c}{\lambda_m^c} \left(e^{-\lambda_m^c \, t_{cool}} - e^{-\lambda_m^c \, (t_{cool}+t_{irr})} \right) \\ &= \sum_{c,r\to b} \sum_{m=1}^{j_c} \frac{c_m^c}{\lambda_m^c} \, e^{-\lambda_m^c \, t_{cool}} \left(1 - e^{-\lambda_m^c \, t_{irr}} \right) \end{aligned} \tag{3.14}$$

where c runs over all decay chains starting from radionuclide r leading to radionuclide b and j_c is the number of radionuclides in a given decay chain c. λ_m^c is the total decay rate of the m^{th} radionuclide in decay chain c. $\tilde{\lambda}_m^c$ is the partial decay rate of the m^{th} radionuclide in the given decay chain c and the coefficient c_m^c is the *bateman coefficient* [33, 34] of the m^{th} radionuclide in decay chain c given by

$$c_m^c = \frac{\prod_{i=1}^{j_c} \tilde{\lambda}_i^c}{\prod_{\substack{i=1 \\ i\neq m}}^{j_c} (\lambda_i^c - \lambda_m^c)}. \tag{3.15}$$

3.4.3 Measurement of neutron activation

One of the ways to measure neutron activation is to measure the energy spectra of the γ-rays emitted with the so called γ-spectroscopy. This can be achieved mainly with scintillation detectors, such as *sodium iodide detectors NaI(Tl)* and with semiconductor detectors, such as *High-Purity Germanium detectors (HPGe)*. The latter one was used as well in the framework of this work for the experimental measurements of activation detectors, more information about the measurements can be found later in the chapters 6 and 8.

Methodology of the current work

First there is an irradiation of activation sample detectors (more details about the placement of the samples can be found in chapters 6 and 8). In the experiments performed, bismuth, aluminium and indium samples were used. After the irradiation is over, the activation samples are taken in the γ-spectrometry laboratory and their activities are measured. Then, these activities are converted to production yields per atom per primary proton on the target by taking into account the corresponding irradiation profiles and the corresponding cool-down times, as shown before in 3.4.2. Basically, using the already mentioned Eq. 3.12, the measured production yield can be calculated just dividing the measured activity by the time evolution that is estimated in each case separately.

On the other hand, the neutron fluence per primary proton on the target on each of the irradiation positions has been estimated by the FLUKA code (see more details in chapter 4). Then, the neutron fluence is weighted with the cross section data of the corresponding radionuclides to obtain the predicted production yields per atom per primary proton on target.

The γ-lines and half lives of the measured radionuclides in the dedicated experiments are indicated on the following table, Tab. 3.3. Typical bismuth spectra obtained in these experiments are shown in Fig. 3.4.

Table 3.3: The γ-lines and the half lives of the measured radionuclides during the experimental periods for this work.

Radionuclide	γ-lines (keV)	Half life (h)
Bi-201	629.1*	1.8
Bi-202	422.2 657.5 960.7	1.72
Bi-203	820.2 825.3 1847.4	11.76
Bi-204	899.2 984.0	11.22
Bi-205	703.4 1764.4	367.44
Bi-206	803.1 881.0 1718.1	149.832
Na-24	1369.0	14.957
In-115m	336.0	4.486

* γ-line of the daughter radionuclide ^{201m}Pb which is in equilibrium with Bi-201.

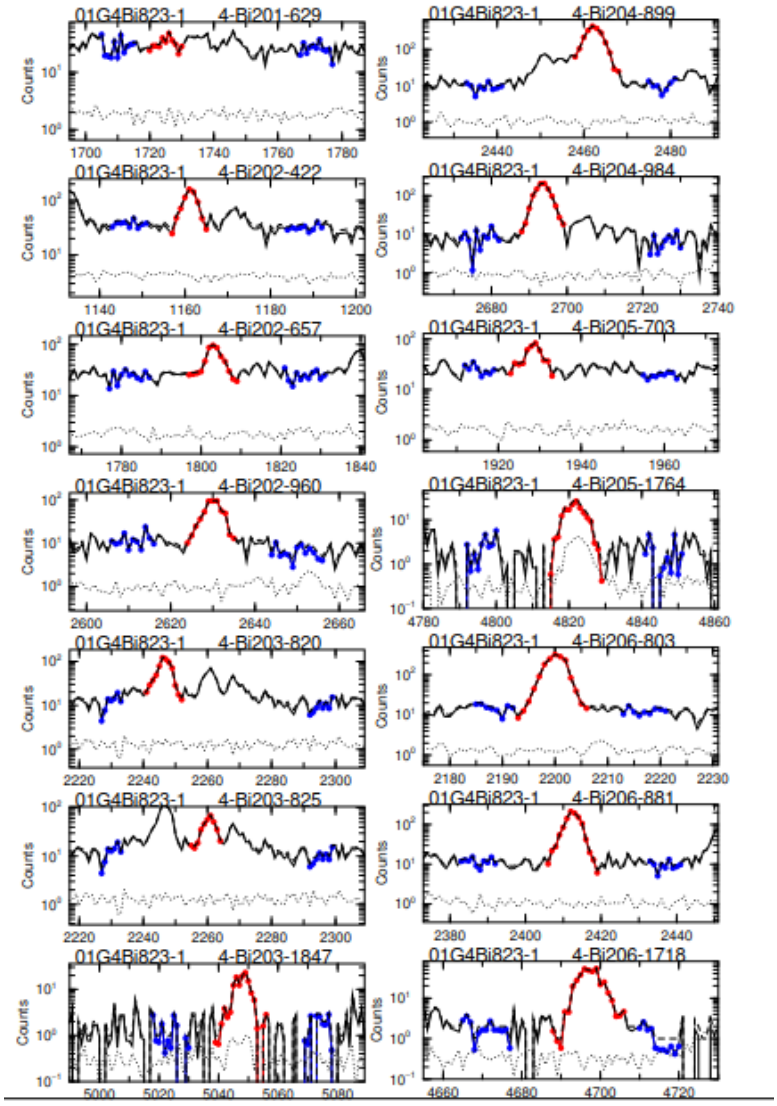

Figure 3.4: Typical bismuth spectra obtained in the present work for a specific sample coded Bi823 (more information can be found in chapter 8, in Tab. 8.3 and in Tab. 8.5 where Bi823 corresponds at the bismuth sample on the position 4). The measured isotope followed by its energy in keV is indicated on the right top of each plot [35].

Chapter 4

The FLUKA Monte Carlo Simulation Code

This chapter presents the FLUKA Monte Carlo simulation code and a description of its most important aspects for this work.

4.1 The FLUKA code

FLUKA (FLUktuierende KAskade) [16, 17] is a general purpose Monte Carlo code tool for the simulation of particle transport and interactions with matter, covering an extended range of applications spanning from proton and electron accelerator shielding to target design, calorimetry, activation, dosimetry, detector design, Accelerator Driven Systems, cosmic rays, neutrino physics, radiotherapy etc. This tool has its roots in radiation protection studies at high energy accelerators and thus contains all features needed in this area of application [36].

The FLUKA code can simulate with high accuracy the interaction and propagation in matter of about 60 different particles, including photons and electrons from 1 keV to thousands of TeV, neutrinos, muons of any energy, hadrons of energies up to 20 TeV (up to 10 PeV by linking FLUKA with the DPMHET code) and all the corresponding antiparticles, neutrons down to

thermal energies and heavy ions. The program can also transport polarised photons (e.g., synchrotron radiation) and optical photons. Time evolution and transport of radiation emitted from the decay of unstable residual nuclei can be performed on-line.

4.1.1 Physical models & features

FLUKA uses physical models for hadron inelastic nuclear interactions, elastic scattering, nucleus-nucleus interactions, transport of charged hadrons and muons, low energy neutrons (<20 MeV), electrons, photons, optical photons and neutrinos.

The module used for hadronic interactions is called PEANUT (PreEquilibrium Approach to Nuclear Thermalization) and comprises a phenomenological description (Dual Parton Model-based Glauber-Gribov cascade) of high-energy interactions (up to 20 TeV), a generalized intra-nuclear cascade and pre-equilibrium emission models as well as evaporation, fragmentation, fission, and de-excitation by gamma emission models. Ions interactions are simulated through interfaces with different codes based on models suitable for certain ranges of energy (DPMJET3 above 5 GeV/nucleon, rQMD-2.4 between 0.1 and 5 GeV/nucleon, Boltzmann Master Equation below 0.1 GeV/nucleon). The interface with DPMJET3 also allows the simulation of minimum-bias proton-proton and heavy ion collisions at LHC energies which enormously facilitates calculations of stray radiation fields around LHC experiments.

The transport of neutrons with energies below 20 MeV is performed by a multi-group algorithm based on evaluated cross section data (ENDF/B, JEF, JENDL, etc.) binned into 260 energy groups, 31 of which are in the thermal energy region. For a few isotopes (1H, 6Li, 10B, 14N) point-wise cross sections can be optionally used during transport. The detailed implementation of electromagnetic processes in the energy range between 1 keV and 1 PeV is fully coupled with the models for hadronic interactions.

Many variance reduction techniques are available in FLUKA, among others, weight windows, region importance biasing as well as leading particle,

interaction length and decay length biasing. Subsection 4.1.3 describes the biasing techniques relevant for this work.

FLUKA has one-of-a-kind capabilities for studies of induced radioactivity, specifically with regard to radionuclide production, their decay and the transport of residual radiation. Particle transport and interaction of prompt and residual radiation are simulated in parallel based on microscopic models for nuclide production and a solution of the Bateman equations for activity build-up and radioactive decay. The decay radiation and its associated electromagnetic cascade are internally flagged as such in order to distinguish them from the prompt cascade. This allows the user to apply different transport thresholds and biasing options to residual and prompt radiation and to score both independently.

Particle fluences can be weighted on-line with energy-dependent conversion coefficients in order to obtain the effective dose or the ambient dose equivalent. Prompt and residual dose equivalent can therefore be calculated in three-dimensional meshes, the latter for arbitrary user-defined irradiation and cooling profiles.

4.1.2 Combinatorial geometry

The combinatorial geometry model used by FLUKA to describe the geometry of the simulation is based on two fundamental concepts: bodies and regions. Bodies are defined as convex solid bodies, e.g. portions of space delimited by surfaces of first (planes) or second (quadratics), infinite cylinders (circular and elliptical) and planes (half-spaces). An advantage of using infinite bodies is that they make input preparation and modification much easier and less error-prone. Regions are defined as combinations of bodies by using the Boolean operators like union, difference and intersection. Each region is not necessarily simply connected, since it can be made of two or more non contiguous parts, but must be of homogeneous material composition. FLUKA provides the user with a geometry debugger in order to facilitate the procedure of building the geometry with the capability of finding un-

defined points, i.e. points which are not included in any defined region, as well as multiple defined points, i.e. points which are included in more than one region. All the regions are surrounded by an infinitely absorbing material ("blackhole"), which absorbs all the escaping particles. A repetition capability ("lattice") is available to avoid the multiple description of repetitive structures. Only one module has to be defined, which can be re-iterated as many times as required. This allows defining geometries, containing up to thousands of different regions, by using only a small number of region and body definitions.

The current FLUKA model for the CHARM and CSBF facility consists of more than 1000 bodies and more than 400 regions.

4.1.3 Biasing

FLUKA is able to perform fully analogue particle transport calculations. However, in many cases of non-uniform radiation fields only on a very small fraction of all histories contributes to the desired response in the regions of interest. In these cases, the user's concern might be to estimate the desired response in the most efficient approach. This can be achieved by the replacement of the actual physical problem with a mathematically equivalent one, i.e. having the same solution but faster statistical convergence. This replacement technique is called *biasing*.

When the limit of the number of histories tends to infinity, the values of all calculated quantities tends exactly to the same averages in the analogue and in the corresponding biased calculation. Namely, biasing is mathematically correct and involves no approximation. Nonetheless, an acceleration of convergence in specific regions of phase space (space/energy) will generally give the disadvantage of a slower convergence in other regions. Due to the fact that an actual calculation does not use an infinite number of particles, but it is necessarily truncated after a finite number of histories, results must be judged accordingly.

Biasing plays a fundamental role, the main part of the present work, be-

cause collecting satisfactory statistics for deep shielding penetration problems requires a lot of computing time.

Importance biasing

The simplest and safest biasing option in FLUKA is importance biasing. This method was used to perform the simulations of this work.

Each geometry region can be assigned an importance, particularly a number between 10^{-4} and 10^{5}, proportional to the contribution that particles in that region are expected to give the desired result: the number of particles moving from a region to the neighbouring one will increase or decrease accordingly to the ratio of importance values assigned to both regions and the particle statistical weight will be modified inversely so that the total weight will remain unchanged. For instance, in a simple, mono-dimensional attenuation problem, the importance is often set at the inverse of the expected fluence attenuation factor for each region, in order that the fluence value is constant with the increasing shielding thickness.

The equivalent dose attenuation by a thick shielding is in first order described by an exponential attenuation [37]:

$$exp(-\frac{z}{\lambda}) \tag{4.1}$$

where z (in g·cm^{-2}) is the shielding thickness and λ (in g·cm^{-2}) is the attenuation length typical of the shielding material. Since each particle (according to its energy) contributes differently to the total equivalent dose, the biasing was built in order to maintain constant the scored dose and not the particle fluence.

The importance value of the inner shielding region can start from 10^{-4} and increase while moving outwards. Every region is given an importance value equal to the value of the previous adjacent one multiplied by a factor R, which is the inverse of the expected attenuation in the considered region:

$$R = \frac{1}{exp(-\frac{\Delta z}{\lambda})} = exp(\frac{\Delta z}{\lambda}) \tag{4.2}$$

where Δz (in g·cm^{-2}) is the shielding thickness of the considered region and λ (in g·cm^{-2}) is the attenuation length. Once 10^5, the highest importance possible in FLUKA, is reached in a certain region, all the following regions are given this same constant value of importance, which means that no biasing is applied.

4.1.4 Scoring

Results in a Monte Carlo calculation can be obtained by adding up the contributions to the "score", or "tally" of a detector defined by the user [17]. A detector is the Monte Carlo equivalent of a measurement instrument. Each detector, also denoted as "estimator", is designed to estimate one or more radiometric quantities, and the final score is a statistical estimation of the average value of the corresponding population of primary particles. As in experimental measurements, it is possible to calculate a standard deviation by running several independent calculations.

There are different input options corresponding to different types of detectors. The simplest one is SCORE which provides energy deposition (proportional to absorbed dose) or star density in every region of the geometry. "Stars" is an old name for inelastic hadron reactions which derives from early experiments with nuclear emulsions.

The same quantities can be scored in a geometry-independent uniform spatial mesh, called a "binning", by means of the option USRBIN. There are several types of binnings: Cartesian, 2D-cylindrical, 3D-cylindrical and even more complex phase space structures. In addition to dose and star density, it is possible to use USRBIN to score weighted particle fluence distributions. USRBIN results are often displayed as colour plots where each colour corresponds to a pre-defined colour-coded range of values.

Fluence, averaged over the volume of a given geometry region, can be

calculated with options USRTRACK. It is a "track-length estimator" (it estimates fluence as volume density of particle trajectory lengths). USRTRACK works also in vacuum and provides fluence differential energy spectra.

Production of residual nuclei can be obtained with command RESNUCLEi. The results, which are closely related to induced activity and dose rate from activated components, can include nuclei produced in low-energy neutron interactions, provided the corresponding information is available in the neutron cross-section library for the materials of interest.

In this thesis, the main scoring options used for the fluence of the particles and the estimation of the ambient dose equivalent were USRTRACK to obtain energy dependent fluence spectra and USRBIN where the fluences were folded with a set of energy dependent coefficients.

Chapter 5

Motivation for the CERN Shielding Benchmark Facility (CSBF)

One of the main areas of application of the FLUKA code is the design of new facilities. Moreover, integral part of the FLUKA code development is benchmarking of predictions of new features against experimental data. It includes both the comparison of predictions of individual models to measurement results (e.g., nuclide production cross sections) as well as benchmarks for actual complex situations that, for example, arise during accelerator operation. The CERN Shielding Benchmark Facility (CSBF) was especially designed to obtain experimental data for benchmarking the deep shielding penetration by the particles from high energy proton accelerator operations.

The CSBF is a unique facility because has great flexibility for realizing different shielding configurations. Furthermore has a variability of beam intensity that can range from $3{\cdot}10^{9}$ to $5{\cdot}10^{11}$ protons per spill and finally, due to its relatively high beam intensity there is good signal even for very thick shielding thicknesses.

The first prototype of the CSBF was installed during the Long Shut-down 1 (LS1) in 2013/2014. It was installed together with the entire shielding of

the CHARM facility. As installed in LS1, the prototype CSBF consisted of 80 cm of cast iron and 360 cm of concrete and barite concrete at some places. The CSBF layout during the LS1 and 2015 is shown in Fig. 6.2. A first characterization of the CSBF facility was performed in July 2015 with the activation of bismuth and aluminium detectors in the CSBF. Monte Carlo simulations with the FLUKA code have been performed to estimate the production yields of bismuth isotopes (^{206}Bi, ^{205}Bi, ^{204}Bi, ^{203}Bi, ^{202}Bi, ^{201}Bi) from^{209}Bi and ^{24}Na from ^{27}Al for these samples. The production yields estimated by FLUKA Monte Carlo simulations are compared to the production yields obtained from γ-spectroscopy measurements of the samples taking the beam intensity profile into account. More details about the activation campaign in 2015 can be found in chapter 6.

Based on the experience gained during the activation campaign in 2015, the CSBF has been significantly upgraded during the extended year-end technical stop at the beginning of 2016. It consists now of 40 cm of cast iron shielding and up to 400 cm of concrete. The new configuration is composed of a 200 cm long removable sample holder concrete block with 3 slots for activation samples, a material test location that is used for the measurement of the attenuation length for different shielding materials as well as for sample activation at different thicknesses of the shielding materials and a dedicated platform for measuring deep penetration neutron spectra with active and passive detectors, covered by two barite concrete blocks. The CSBF layout under normal operation of the CHARM facility is indicated in the Fig. 7.1. In September 2016 there was a second activation campaign with activation of bismuth, aluminium and indium samples that were placed in the CSBF to characterize the upgraded version of the CSBF. Monte Carlo simulations with the FLUKA code have been performed to estimate the specific production yields of bismuth isotopes (^{206}Bi, ^{205}Bi, ^{204}Bi, ^{203}Bi, ^{202}Bi, ^{201}Bi) from ^{209}Bi, ^{24}Na from ^{27}Al and ^{115m}I from ^{115}I for these samples in the new configuration and have then been compared to the production yields obtained from γ-spectroscopy measurements of the samples taking the beam intensity pro-

file into account. More details about the CSBF upgrade and the activation campaign of 2016 are presented in chapter 7 and in chapter 8 respectively.

In parallel to the activation campaign in 2016, there was a series of measurements with a high-pressure ionisation chamber filled with hydrogen gas at 20 bar, calibrated for measuring ambient dose equivalent rates, in the material test location. The ionisation chamber was placed on top of different shielding thicknesses of different shielding materials, e.g normal concrete, barite concrete, cast iron. By comparing the dose rate measured at different positions, the neutron spectrum averaged attenuation length of the shielding materials is estimated. Detailed information about this experiment is presented in chapter 9.

525. Motivation for the CERN Shielding Benchmark Facility (CSBF)

Chapter 6

Activation campaign in the prototype CSBF in 2015

The CERN High Energy AcceleRator Mixed field facility (denoted CHARM, see chapter 2) has been constructed in the CERN Proton Synchrotron (PS) East Experimental Area in 2014 [11]. The facility receives a pulsed proton beam from the CERN PS with a beam momentum of 24 GeV/c with $5{\cdot}10^{11}$ protons per pulse with a pulse length of 350 ms and with a maximum average beam intensity of $6.7{\cdot}10^{10}$ p/s [12] with a minimum pulse spacing of 2.4 s.

The extracted proton beam from the PS impacts on a cylindrical copper or aluminium target and the created secondary radiation field is used to test electronics equipment installed at predefined test positions [8].

The shielding of the CHARM facility [13] also includes the CERN Shielding Benchmark Facility (CSBF) situated laterally above the target [10]. This facility allows deep-penetration benchmark studies of various shielding materials.

The installation of a first prototype version of the CSBF has been performed during the construction of the CHARM facility in 2014.

Activation samples of bismuth and aluminium can be used for the measurement of high-energy neutrons [38]. In order to characterize the radiation fields in the prototype CSBF such samples were placed in the CSBF and in

the CHARM access corridor in July 2015. Monte Carlo simulations with the FLUKA code [16, 17] have been performed to estimate the specific production yields of several bismuth isotopes and sodium-24 for these samples. This chapter describes the comparison between the estimated values from FLUKA and the activation measurements performed in July 2015 with bismuth and aluminium disk samples of different sizes in the prototype CSBF and in the CHARM access corridor [39–41].

6.1 Beam parameters and configurations

This section presents the beam parameters and the facility configurations that were used during the activation experiments. The beam intensity was measured with a Secondary Emission Chamber, denoted SEC1, whose measurement values are logged in the measurement database, TIMBER. An intensity calibration factor of $1.87{\cdot}10^7$ protons/count has been applied to the counts per pulse to obtain the number of protons per pulse. This calibration factor had been obtained with aluminium foil activation using sodium isotopes with a statistical uncertainty of 7% from the γ-spectrometry measurement [42].

A beam size of 1.2 cm x 1.2 cm Full Width at Half Maximum (FWHM) was used for the FLUKA simulations as specified in the layout of the beam line and confirmed with online beam profile measurements [42].

The average beam intensity of CHARM, binned in 10 minutes long intervals, from July 9 to July 15, 2015 when the experiments were conducted, is shown in the Fig. 6.1. The 4 different irradiation periods used during the activation measurements are also indicated in Fig. 6.1.

The beam passes through the upstream IRRAD facility before impacting on the CHARM target. During the period of the experiment, Silicon samples with a total thickness of 0.2 cm were placed into the beam in IRRAD and this was also taken into account in the FLUKA simulations.

The shielding layout of the prototype CSBF is shown in Fig. 6.2. The

chemical composition of the concrete, the barite concrete and the cast iron implemented in the FLUKA Monte Carlo simulations for the shielding with their respective densities are listed in Tab. 6.1, in Tab. 6.2 and in Tab. 6.3.

During the activation experiment, the cylindrical copper target of 8 cm diameter and 50 cm length has been used inside the CHARM facility. Inside the target room, there are four movable shielding walls, each of 20 cm thickness and made out of concrete and iron. They can be placed between the target and the irradiation positions in the CHARM facility in varied arrangement, so that the test spectra are adjusted to the desired radiation field (energy and intensity) during the tests. The movable shielding walls are presented in the Fig. 6.3. For this activation experiment, two different configurations of the four movable shielding walls were used during the different irradiation periods, i.e all movable shielding walls retracted from the facility or all movable shielding walls inside the facility. The configurations have been properly taken into account in the FLUKA Monte Carlo simulations.

Table 6.1: Chemical composition and density of concrete [43].

Concrete	Density 2.4 g/cm^3		
Element	Weight fraction (%)	Element	Weight fraction (%)
Hydrogen	0.561	Silicon	16.175
Carbon	4.377	Sulfur	0.414
Oxygen	48.204	Potassium	0.833
Sodium	0.446	Calcium	23.929
Magnesium	1.512	Titanium	0.173
Aluminium	2.113	Iron	1.263

Table 6.2: Chemical composition and density of barite concrete [44].

Barite Concrete	Density 3.35 (g/cm^3)
Element	Weight fraction (%)
Aluminium	0.418
Barium	46.34
Calcium	5.019
Iron	4.751
Hydrogen	0.358
Magnesium	0.12
Oxygen	31.162
Sulfur	10.786
Silicon	1.046

Table 6.3: Chemical composition [45] and density of cast iron [43].

Cast Iron	Density 7.2 g/cm^3
Element	Weight fraction (%)
Iron	92.3
Carbon	3.85
Manganese	0.3
Silicon	3.4
Phosphorus	0.08
Sulfur	0.02
Cobalt	0.05

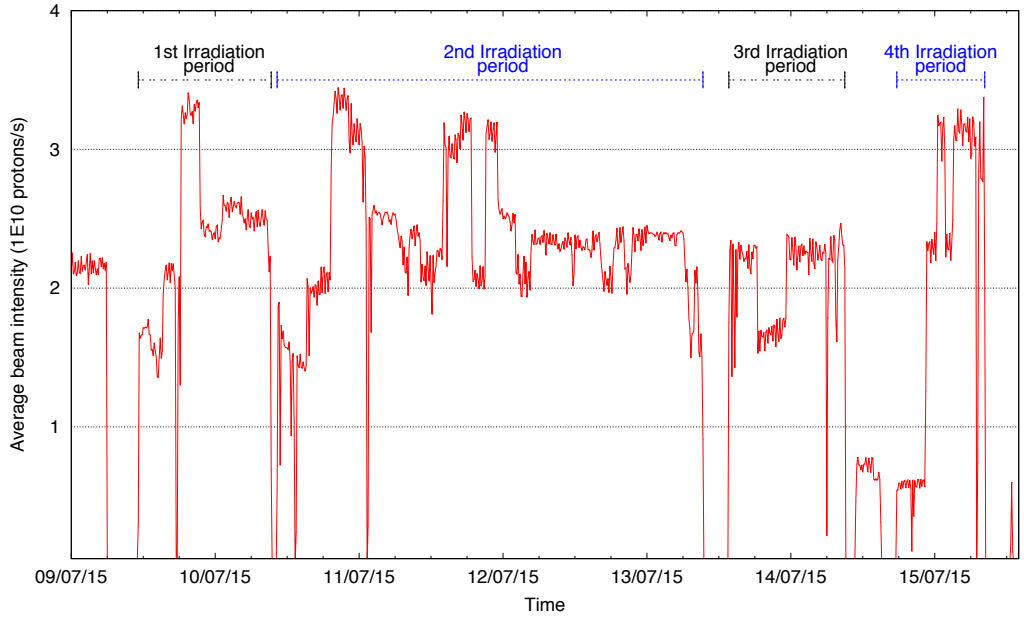

Figure 6.1: Average beam intensity sent to the CHARM facility during the activation experiments in 2015 with binning of 10 minutes long intervals.

6.2 Samples and locations

Eleven disk samples in total, six bismuth samples and five aluminium samples, have been irradiated in 2015. Of these samples, five bismuth samples and four aluminium samples were placed in the prototype CSBF at different heights and one bismuth sample and one aluminium sample inside the CHARM facility access corridor. All the details of the samples including their location, irradiation time, dimensions, weight, time of measurements are presented in Tab. 6.4.

Table 6.4: Description of the irradiated samples and details of the γ-spectrometry measurements in the CERN γ-spectrometry laboratory.

Sample Material	Irradiation Location	Duration of irradiation (h)	Start of irradiation (date and time)	Dimensions (mm)	Weight (g)	γ-spectrometry measurement duration (h)
Bi	80cm Fe + 0cm Concrete	19.3	13/07/2015, 13:40 PM	40(diam.)×4	49.5	3 20
Bi	80cm Fe + 80cm Concrete	19.3	13/07/2015, 13:40 PM	40(diam.)×4	49.52	3 20
Bi	80cm Fe + 160cm Concrete	19.3	13/07/2015, 13:40 PM	80(diam.)×10	523.5	3 20
Bi	80cm Fe + 240cm Concrete	22.16	09/07/2015, 11:10 AM	80(diam.)×10	543.18	3 48
Bi	80cm Fe + 240cm Concrete	94.16	09/07/2015, 11:10 AM	80(diam.)×10	540.34	3
Bi	Access Corridor Loc 3	14.6	14/07/2015, 17:40 PM	40(diam.)×4	49.49	3 3 20
Al	80cm Fe + 0cm Concrete	19.3	13/07/2015, 13:40 PM	40(diam.)×4	13.32	3
Al	80cm Fe + 80cm Concrete	19.3	13/07/2015, 13:40 PM	40(diam.)×4	13.3	15
Al	80cm Fe + 160cm Concrete	19.3	13/07/2015, 13:40 PM	80(diam.)×10	135.4	3
Al	80cm Fe + 240cm Concrete	19.3	13/07/2015, 13:40 PM	80(diam.)×10	135.55	15
Al	Access Corridor Loc 3	14.6	14/07/2015, 17:40 PM	40(diam.)×4	13.31	3 20

The irradiation of the samples in the prototype CSBF has been performed with the four movable shielding walls retracted from the facility. On the other hand, when the samples were placed inside the CHARM facility access corridor, the four movable shielding walls were inside the facility.

The irradiation positions of the samples in the CSBF and also inside the CHARM facility access corridor are illustrated in Fig. 6.2 and Fig. 6.3.

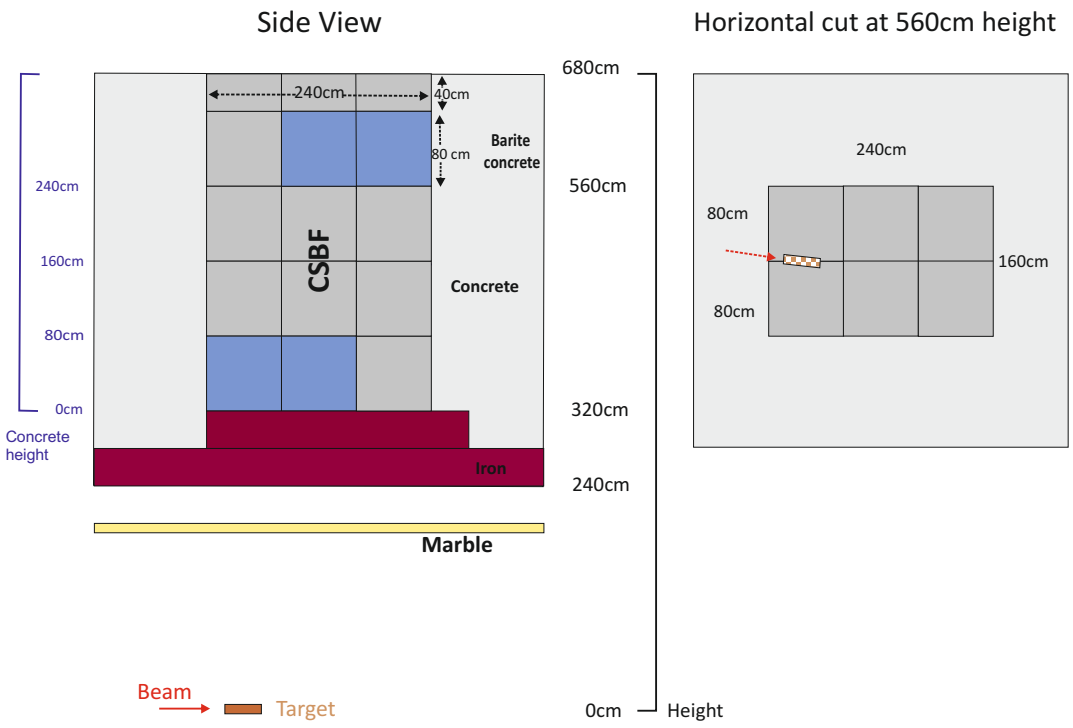

Figure 6.2: Position of the samples (material of the samples as shown in Tab.6.4) at different heights in the prototype CSBF. Barite concrete is indicated in blue. The chemical compositions of concrete, barite concrete and cast iron are shown in Tab.6.1, in Tab.6.2 and in Tab.6.3 respectively.

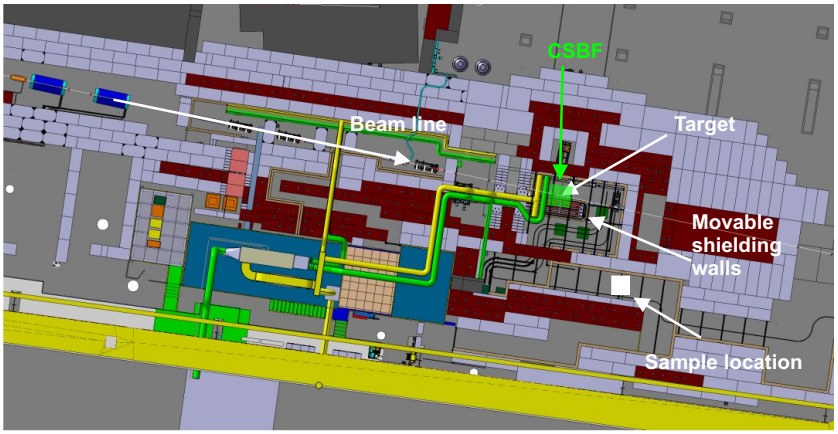

Figure 6.3: Position of the samples inside the CHARM facility access corridor at beam line level indicated with the white square.

6.3 Simulations and measurements results

The simulation results were obtained by first scoring the neutron fluence spectra in the activation sample volumes with FLUKA. A detailed description of the models and cross section data used in FLUKA can be found in [16, 17] and in chapter 4. Then the neutron fluence was weighted with cross section data for the bismuth isotopes and sodium-24 [46], shown in Fig. 6.4, to obtain the predicted production yields per atom per primary proton on the target.

The activities of the bismuth isotopes and sodium-24 were measured for the bismuth and aluminium samples respectively using γ-spectrometry, sometimes even at different cool-down times. In case of multiple γ-spectrometry measurements of the same sample, the activities selected were the ones with the lowest uncertainty of the γ-spectrometry measurements. These activities have been converted to the production yields by taking into account the corresponding irradiation profiles with 10 minutes long binning and the corresponding cool-down times as described in subsubsection 3.4.3.

The production yields predicted by FLUKA and measured by γ-spectrometry are presented in Fig. 6.5, Fig. 6.6 and in Tab. 6.6. The agreement between FLUKA predictions and γ-spectrometry measurements for the production yields is better than a factor of 2. This is illustrated in Fig. 6.7 and Fig. 6.8.

The contributions that have been taken into account for the uncertainty estimation are shown in Tab. 6.7. The uncertainty of the sample positions at the given shielding thicknesses as well as the uncertainty of the beam size have negligible impact on the results as verified by FLUKA simulations. The materials placed in IRRAD during the period of the experiment were taken into account in the simulations. The uncertainty of the production yields coming from the uncertainty of the materials placed in IRRAD is far below 1%.

The uncertainty of the composition of concrete and cast iron as well as the uncertainty of the dimensions of the shielding structure are negligible compared to the uncertainty from the density uncertainty. A hypothetical

change in the concrete density would provoke a change on the slope of the dependence of the yields on the depth of the shielding plotted in Fig. 6.5, Fig. 6.6 and the effect of the change would increase with increased shielding thickness.

The cumulative contribution to the production yields as function of the neutron energy is presented in Fig. 6.9 for the sample placed at a concrete shielding thickness of 240 cm in the CSBF. From this figure it can be seen that for sodium-24, the energy range contributing to the production yield is quite large whereas for the bismuth isotopes the energy ranges are narrower and located around the respective cross section peaks. The 10%, 25%, 75% and 90% quantiles of the production yield distribution for the various radionuclides, denoted $q_{0.1}$, $q_{0.25}$, $q_{0.75}$ and $q_{0.9}$, are presented in Tab. 6.5, quantifying the energy range of the neutron field that has been probed by the comparison of the predictions to measurements of the various radionuclides production processes.

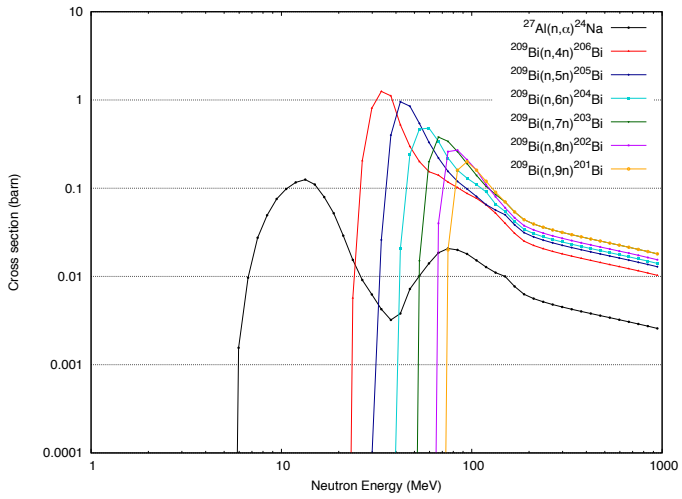

Figure 6.4: Cross sections of the bismuth isotopes and sodium-24 production as a function of the neutron energy [46].

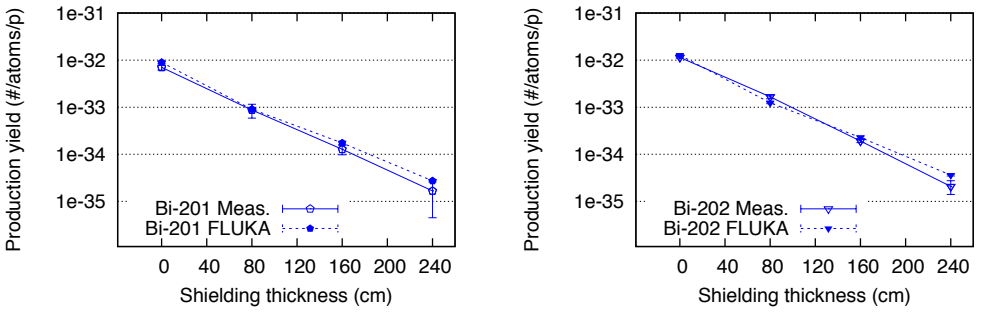

(a) Bi-201

(b) Bi-202

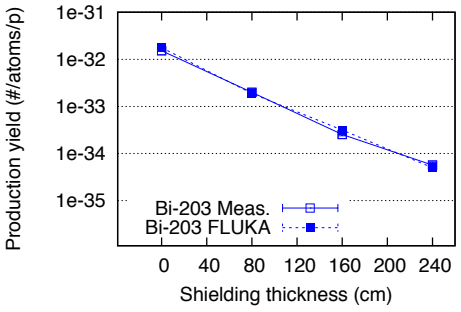

(c) Bi-203

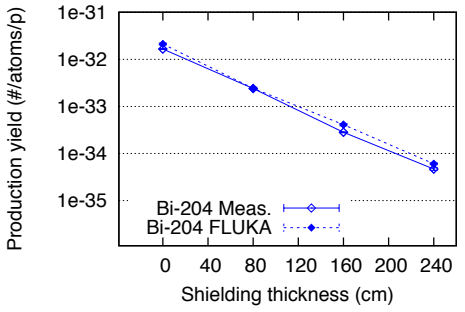

(d) Bi-204

Figure 6.5: Predicted and measured production yields per proton on target for bismuth radionuclides (Bi-201, Bi-202, Bi-203 and Bi-204) as a function of the shielding thickness.

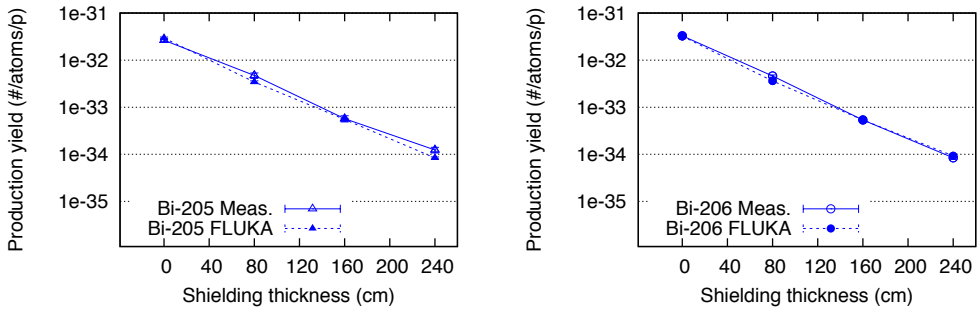

(a) Bi-205

(b) Bi-206

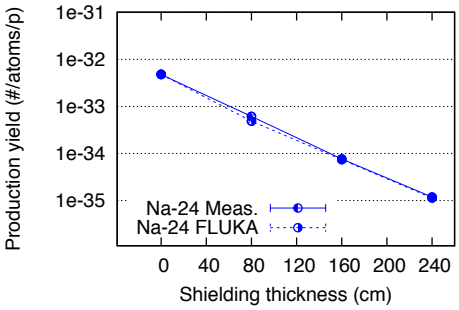

(c) Na-24

Figure 6.6: Predicted and measured production yields per proton on target for bismuth (Bi-205 and Bi-206) and sodium radionuclides as a function of the shielding thickness.

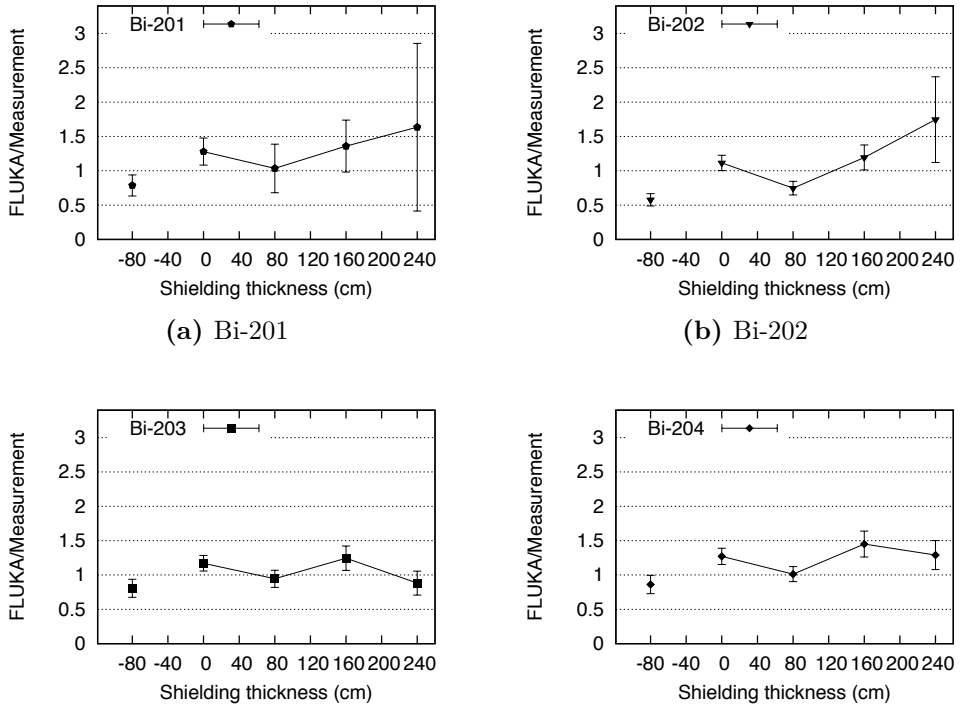

(a) Bi-201 **(b)** Bi-202

(c) Bi-203 **(d)** Bi-204

Figure 6.7: The ratio of predicted and measured production yields per proton on target for bismuth radionuclides as a function of the shielding thickness. The corridor location results are arbitrarily shown at -80 cm shielding thickness, for convenience.

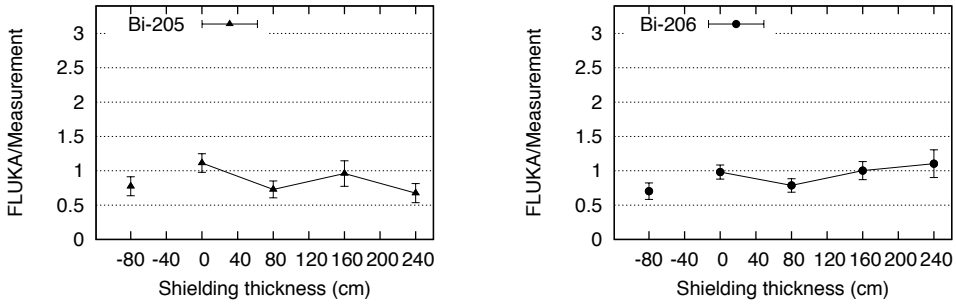

(a) Bi-205

(b) Bi-206

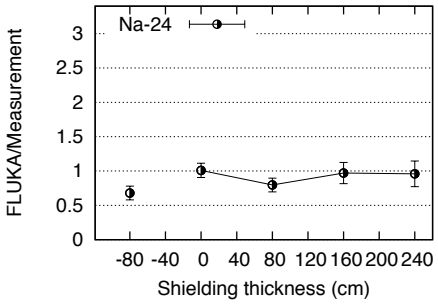

(c) Na-24

Figure 6.8: The ratio of predicted and measured production yields per proton on target for bismuth and sodium radionuclides as a function of the shielding thickness. The corridor location results are arbitrarily shown at -80 cm shielding thickness, for convenience.

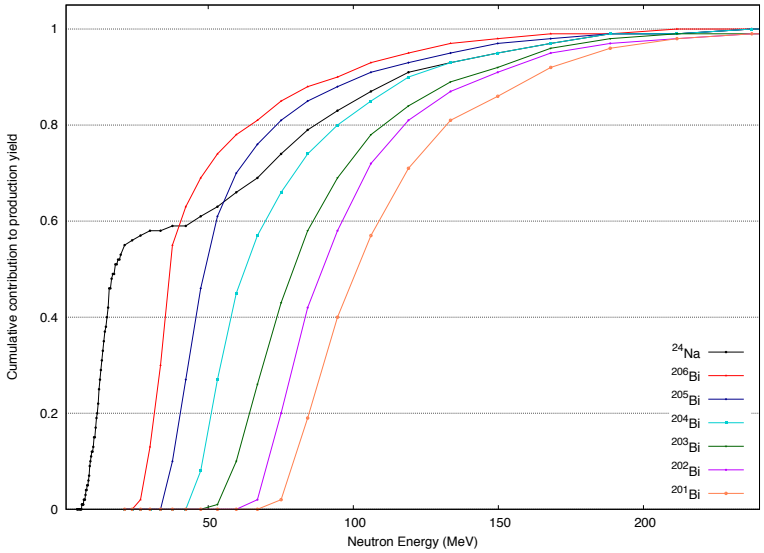

Figure 6.9: Cumulative contribution to the production yields at a concrete shielding thickness of 240 cm as a function of the neutron energy.

Table 6.5: The 10%, 25%, 75% and 90% quantiles of the production yield distribution for the various radionuclides at a concrete shielding thickness of 240 cm.

	Neutron Energy [MeV]			
Radionuclide	$\mathbf{q_{0.1}}$	$\mathbf{q_{0.25}}$	$\mathbf{q_{0.75}}$	$\mathbf{q_{0.9}}$
Bi-201	79.4	87.2	125	162
Bi-202	70.6	77.2	110	145
Bi-203	59.6	66.5	102	138
Bi-204	48.0	52.6	85.9	119
Bi-205	37.6	41.7	65.7	102
Bi-206	29.0	32.5	54.8	94.5
Na-24	9.4	12.4	76.9	115

Table 6.6: Predicted production yields by FLUKA and measured production yields by γ-spectrometry.

Radionuclide	Location (cm)	Predicted Production yield by FLUKA (number/atoms/p)	Uncertainties FLUKA (%)	Measured Production yield (number/atoms/p)	Uncertainties (%)	Ratio Predicted/ Measured	Uncertainties Ratio (%)
Bi-201	Corridor	4.12E-033	±13.6	5.24E-033	±13.9	0.79	±19.5
	0	8.97E-033	±6.2	7.01E-033	±14.1	1.28	±15.48
	80	9.03E-034	±7.5	8.73E-034	±33.3	1.03	±34.2
	160	1.74E-034	±12.71	1.28E-034	±24.7	1.36	±27.8
	240	2.73E-035	±13.5	1.67E-035	±73.4	1.64	±74.7
Bi-202	Corridor	5.42E-033	±13.5	9.39E-033	±7.9	0.58	±15.6
	0	1.27E-032	±6.1	1.14E-032	±7.9	1.12	±10.0
	80	1.24E-033	±7.3	1.66E-033	±11.2	0.75	±13.4
	160	2.28E-034	±11.4	1.91E-034	±10.3	1.19	±15.3
	240	3.63E-035	±13.4	2.08E-035	±33.15	1.75	±35.7
Bi-203	Corridor	8.22E-033	±12.9	1.02E-032	±9.9	0.81	± 16.3
	0	1.78E-032	±5.8	1.52E-032	±7.8	1.17	±9.7
	80	1.88E-033	±7.2	1.99E-033	±11.1	0.94	±13.2
	160	3.16E-034	±10.5	2.54E-034	±9.5	1.24	±14.2
	240	4.99E-035	±13.2	5.66E-035	±14.6	0.88	±19.7
Bi-204	Corridor	1.06E-032	±13.6	1.23E-032	±7.4	0.86	±15.5
	0	2.11E-032	±5.9	1.66E-032	±7.1	1.27	±9.3
	80	2.42E-033	±7.7	2.39E-033	±7.6	1.01	±10.8
	160	4.09E-034	±10.6	2.82E-034	±7.4	1.45	±12.9
	240	6.05E-035	±13.3	4.69E-035	±9.5	1.29	±16.4
Bi-205	Corridor	1.27E-032	±14.3	1.64E-032	±10.6	0.78	±17.8
	0	2.95E-032	±6.6	2.65E-032	±10.1	1.11	±12.1
	80	3.44E-033	±7.8	4.72E-033	±14.8	0.73	±16.8
	160	5.50E-034	±10.4	5.73E-034	±16.4	0.96	±19.4
	240	8.37E-035	±13.6	1.24E-034	±15.4	0.68	±20.6
Bi-206	Corridor	1.35E-032	±15.3	1.92E-032	±7.6	0.71	± 17.1
	0	3.22E-032	±7.4	3.28E-032	±7.4	0.98	±10.5
	80	3.61E-033	±8.8	4.59E-033	±8.9	0.79	±12.5
	160	5.37E-034	±10.2	5.36E-034	±8.2	1.00	±13.1
	240	9.31E-035	±15.2	8.44E-035	±10.2	1.10	±18.3
Na-24	Corridor	1.63E-033	±12.25	2.40E-033	±8.3	0.68	±14.7
	0	4.80E-033	±6.0	4.76E-033	±8.6	1.01	±10.3
	80	4.87E-034	±7.4	6.12E-034	±10.1	0.80	±12.5
	160	7.42E-035	±10.9	7.65E-035	±11.6	0.97	±15.9
	240	1.14E-035	±13.4	1.19E-035	±14.2	0.96	±19.5

Table 6.7: Uncertainties taken into account for the uncertainty estimation of the production yields.

	Source of uncertainty	**Uncertainty on production yield**
Simulations	statistical*	4 - 11 %
	concrete density [1]	0 - 12 % [2]
	cast iron density [1]	4 %
Measurements	γ-spectrometry*	1.3 - 15 % [3]
	sample weights	1 %
	beam intensity (calibration)	7 %
	beam intensity (statistical)*	< 1 %
	beam momentum	< 1 %
	beam position and profile	< 1 %
	target density	< 1 %
	target dimensions	< 1 %

* Statistical uncertainty.
[1] Uncertainty of the concrete and cast iron density is 0.05g/cm^3.
[2] The concrete density uncertainty leads to an uncertainty of the production yield of 0% for 0 cm of concrete and of up to 12% for 240 cm of concrete.
[3] Except for ^{201}Bi at 80, 160, 240 cm and for ^{202}Bi at 240 cm, see Tab. 6.6.

6.4 Summary

Activation disk experiments have been conducted from July 9 to July 15, 2015 in the CHARM facility. Bismuth and aluminium disk samples were placed in different locations in the prototype CSBF and inside the CHARM facility access corridor. The production yields computed from the activities of the irradiated samples measured from γ-spectrometry have been compared to the estimated values from FLUKA Monte Carlo simulations. The agreement is better than a factor of 2.

This agreement is consistent with previous similar studies for shielding penetration at the CERN-EU High Energy Reference Field facility [43]. Moreover, from our experience gained through the activation campaign in July 2015 we decided to upgrade the CSBF in 2016 in order to facilitate the procedure of sample placement and to add more functionalities to the facility. Since the results presented in this chapter confirmed FLUKA as a very reliable Monte Carlo simulation tool, the design of the upgrade of the CSBF in the first months of 2016 has been based on FLUKA simulations.

Chapter 7

The Upgrade of the CSBF in 2016

An activation experiment campaign was performed in 2015 at the CERN Shielding Benchmark Facility(CSBF) (see chapter 6) for the characterization of the prototype of the facility [39–41] and, based on this experience, we decided to upgrade the CSBF in 2016 in order to simplify the exploitation of the facility and to integrate new functionalities. The most important requirements for the CSBF upgrade were i) the use of passive detectors, that can be quickly exchanged, like activation samples or passive dosimeters for validating the radiation spectra predicted by Monte Carlo simulations and thus performing Monte Carlo simulation benchmark studies, ii) the use of active detectors or dosimeters, even attached to phantoms, placed on top of the shielding in order to study deep penetration neutron spectra and iii) the creation of a shielding material test location where the attenuation length (λ) for neutrons can be measured for different shielding materials.

The CSBF has been significantly upgraded during the year-end technical stop at the beginning of 2016. The CSBF upgrade allows for easier manipulation and for having more exploitation possibilities of the facility [41, 47]. The design of the upgraded CSBF was based on FLUKA simulations.

During the operational period of 2016, the CSBF consisted of 40 cm cast iron shielding, 360 cm of standard concrete, barite concrete and cast iron shielding that are part of the three main possible configurations of the CSBF.

These three main possible configurations allow measurements in the removable sample holder concrete block (which is also the nominal configuration of the facility during the nominal CHARM facility operation), on the CSBF platform and at the shielding material test location. These configurations are discussed in the next sections.

The requirements for the implementation of the CSBF upgrade and the expected production yields predicted by FLUKA for the upgrade, respectively, are shown in Tab. 7.1. The values presented in Tab. 7.1 can be reduced by up to a factor of 9 by changing the target of the CHARM facility and can be reduced even lower by changing the intensity per spill and/or the numbers of protons per spill ($\sim$ factor of 1000).

Table 7.1: Requirements of the CSBF upgrade.

	Removable sample concrete block	**CSBF platform**	**Shielding material test location**
Purpose	Passive detectors: Activation samples or Passive dosimeters for Monte Carlo benchmark studies	Active detectors and Dosimeters attached to phantoms: Deep penetration neutron spectrum	Measurement of the attenuation length for different materials
Maximum Ambient Dose Equivalent Rate (μSv/h) for $6.7{\cdot}10^{10}$ p/s	$< 1{\cdot}10^{6}$	50 - 100	< 100

The expected production yields predicted by FLUKA are shown in Tab. 7.2 and refer to reasonable sample sizes to be well above the minimum detectable activity (MDA) of the γ-spectrometry set-up of the CERN γ-spectrometry laboratory.

Table 7.2: Expected production yields (nucl/s/g) predicted by FLUKA for $2.2{\cdot}10^{10}$ p/s and $6.7{\cdot}10^{10}$ p/s, nominal and maximum beam intensity respectively.

	Removable sample concrete block	**CSBF platform**	**Shielding material test location**
Production Yields (nucl/s/gr) estimated by FLUKA for Bi isotopes,^{24}Na and ^{115m}In, for $\mathbf{2.2{\cdot}10^{10}}$ p/s, nominal beam intensity	$2{\cdot}10^{-2}$ - 20	$>3{\cdot}10^{-3}$	$>2{\cdot}10^{-3}$
Production Yields (nucl/s/gr) estimated by FLUKA for Bi isotopes,^{24}Na and ^{115m}In, for $\mathbf{6.7{\cdot}10^{10}}$ p/s, maximum beam intensity	$4.37{\cdot}10^{-2}$ - $7.91{\cdot}10^{1}$	$4.99{\cdot}10^{-3}$ - $3.98{\cdot}10^{-2}$	$9.82{\cdot}10^{-3}$ - 4.22

7.1 Concrete attenuation characterization at the removable sample holder concrete block

The removable sample holder concrete block was needed for the facilitation of the handling procedure of activation samples or passive dosimeters in order to place them deep inside the CSBF shielding. The samples are irradiated with the radiation field emerging from the beam impacting on the target and then attenuated through the concrete shielding. After the irradiation is over, the samples are retracted and their activity can be measured in the γ-spectrometry laboratory.

For this reason, the removable sample holder concrete block provides of 3 slots of 10 cm x 10 cm cross section, denoted as positions, that are centered along the vertical axis of the block, so that they can be filled with the samples. The current layout of the CSBF when the removable sample holder concrete block is inserted, is presented in Fig. 7.1. Position 1 is located at a height of 10.5 cm, measured from the bottom of the removable sample holder concrete block, position 2 at 85.4 cm height and position 3 at 160.35 cm height. There is also a possibility of placing samples on the top of the block, mentioned as position 4 at 200 cm height. The block is easily inserted in and extracted from the CSBF shielding in a specifically designed shaft, with dimensions of 40 cm x 40 cm x 240 cm.

A specifically designed remote controlled hook is used for the manipulation of the removable sample holder concrete block, are shown in Fig. 7.2, Fig. 7.16 and Fig. 7.17.

The handling operations for the facility in this configuration are very efficient. The instalment of the samples to be irradiated, that includes extracting the removable sample holder concrete block and then insert it in the facility, takes maximum 30 minutes. This means that samples can be routinely exchanged during the weekly stop of IRRAD and CHARM facilities on Wednesdays. On the other side, the extraction of already irradiated samples can be done in 15 minutes and then the samples can be transferred directly

to the γ-spectrometry laboratory, applying the proper radiation protection transport rules, for measurement.

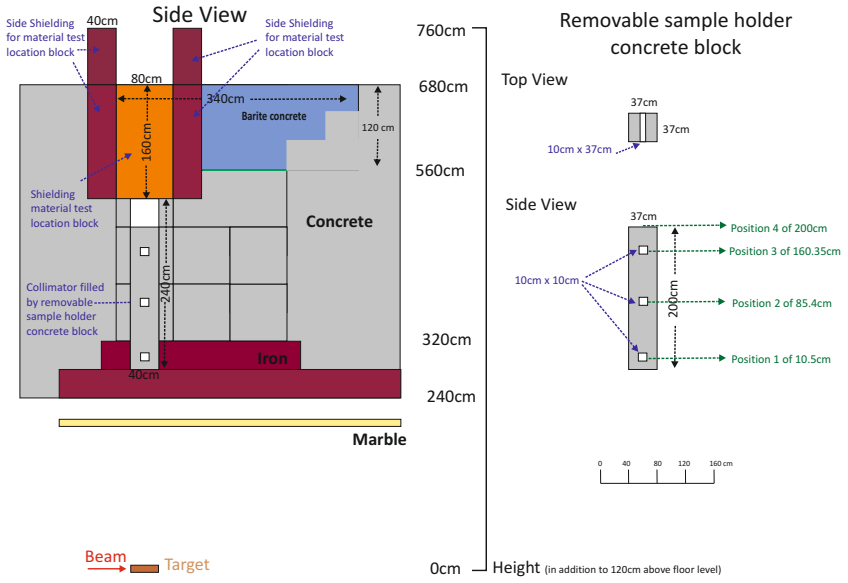

Figure 7.1: CSBF upgrade layout for measurements with the removable sample holder concrete block inserted in the facility.

Figure 7.2: The remote controlled hook used for the manipulation of the removable sample holder concrete block.

7.1.1 Specifications for the removable sample holder concrete block:

The removable sample holder concrete block consists of normal concrete and is 37 cm x 37 cm in horizontal plane and 200 cm in height. The mass of the block is 610 kg, therefore the density is 2.23 g/cm^3. The actual height of the block is limited by the fact that the block can be removed from the facility taking into account the crane clearance plus additional space for handling equipment. The center of the block is slightly offset the center of the target in horizontal plane, see Fig. 7.3.

This block has 3 slots of 10 cm x 10 cm cross-section and a possibility using the upper face as a 4th position. The slots start at heights 10.5 cm, 85.4 cm, 160.35 cm and 200 cm and are centered around the vertical middle axis on one side face. The layout of the CSBF is presented when the removable sample holder concrete block is used in Fig. 7.1.

The neutron spectra predicted by the FLUKA Monte Carlo code at the 4 positions of the removable sample holder concrete block are shown in Fig. 7.4. Moreover the prompt dose equivalent rate is illustrated on the vertical plane of the facility in Fig.7.5 and the fluence of neutrons with a kinetic energy above 20 MeV is shown on the vertical plane of the facility in Fig. 7.6. The shape of the neutron fluence spectra, in Fig. 7.6, between position 3 and position 4 does not change anymore, indicating that the deep shielding equilibrium has been reached.

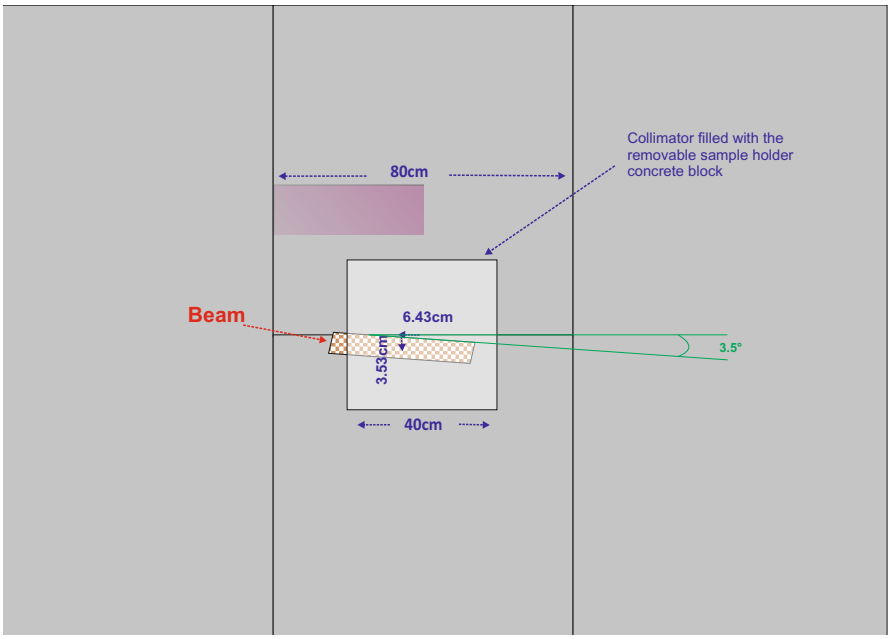

Figure 7.3: The center of the collimator filled with the removable sample holder concrete block is a bit tilted horizontally from the center of the CHARM target.

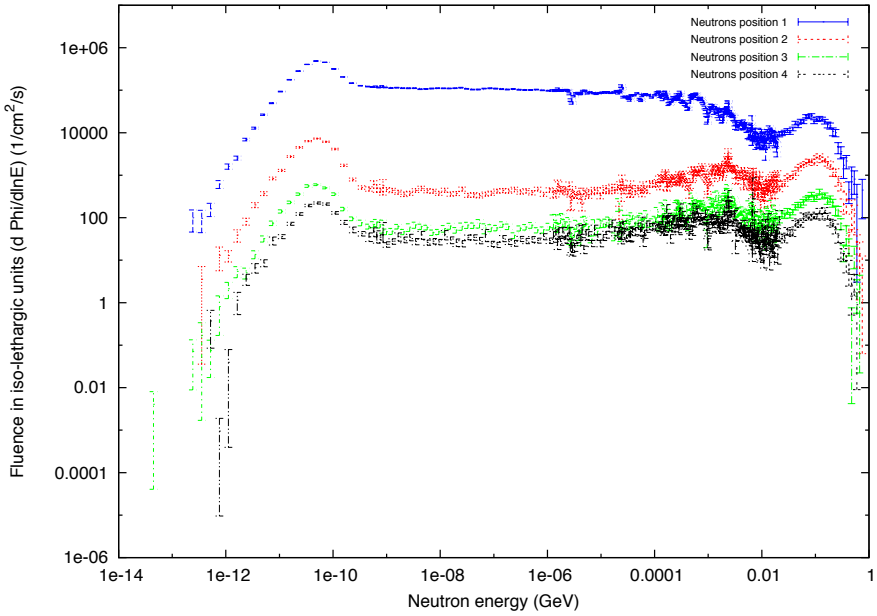

Figure 7.4: Neutron fluence spectra predicted by FLUKA at the 4 different positions in the removable sample holder concrete block for an average beam intensity of $6.7{\cdot}10^{10}$ protons per second.

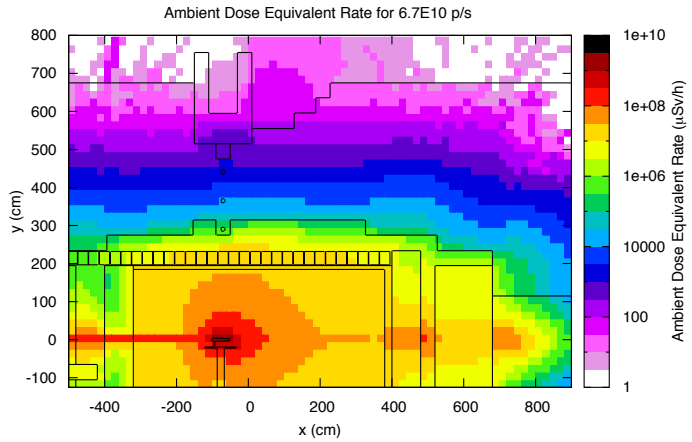

Figure 7.5: Prompt dose equivalent rate on the vertical plane for maximum beam intensity, when the movable shielding is inside the facility, for an average beam intensity of $6.7{\cdot}10^{10}$ protons per second.

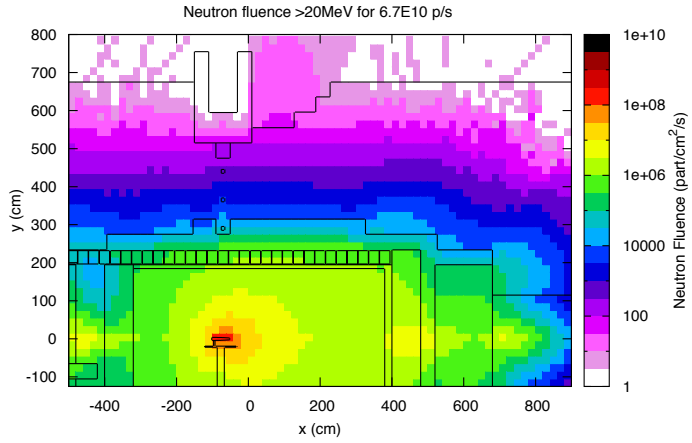

Figure 7.6: Fluence of neutrons with a kinetic energy above 20 MeV on the vertical plane for maximum beam intensity, when the movable shielding is inside the facility, for an average beam intensity of $6.7{\cdot}10^{10}$ protons per second.

7.2 CSBF platform for deep shielding penetration spectra

The CSBF platform was created at a height of 560 cm above beam line level, indicated in Fig. 7.7, covering an area of 120 cm x 160 cm and allows placing active detectors or dosimeters, even attached to phantoms, on the top of the shielding, for measuring their response to a deep penetration neutron spectrum. The shielding layer directly below 560 cm height is implemented with as few gaps as possible. In order to use the platform, two dedicated barite concrete blocks of 120 cm height have to be removed, see Fig. 7.8 and Fig. 7.9. This handling operation can be performed in less than 20 minutes. Measurements at the CSBF platform can be performed in parallel to activation measurements at the removable sample holder concrete block.

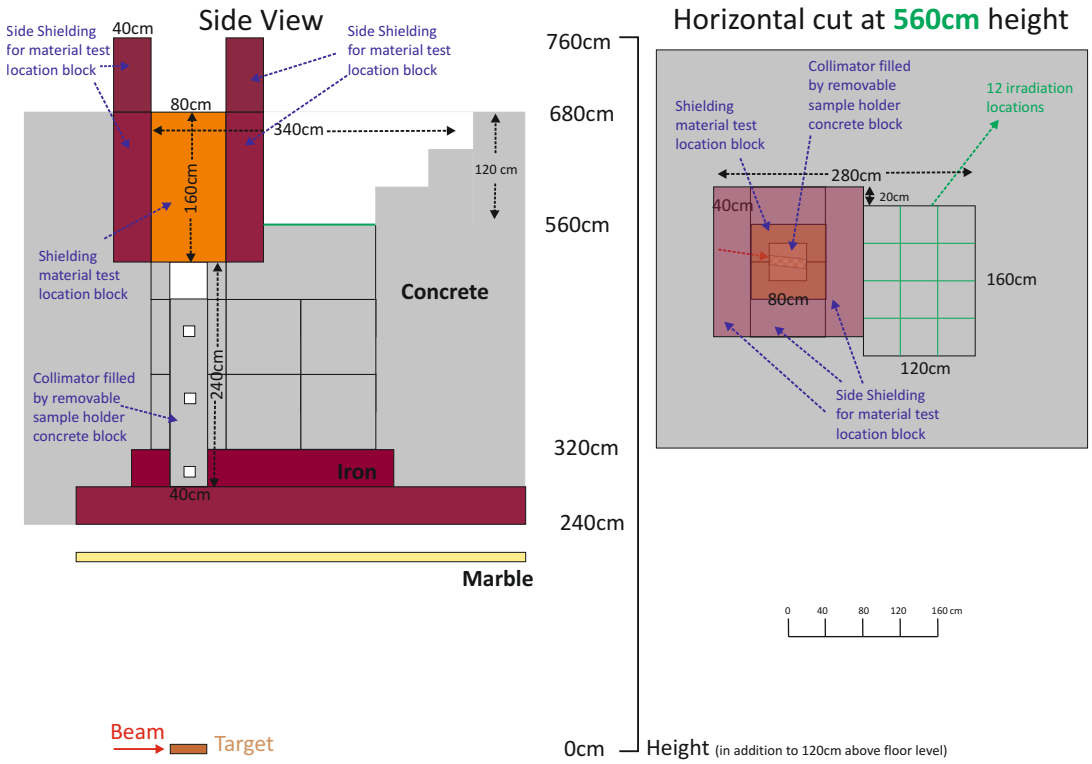

Figure 7.7: CSBF upgrade layout for the CSBF platform usage. The CSBF platform is indicated with the thin green line in the figure on the left.

Figure 7.8: The CSBF platform located at 560 cm above the beam line level, divided into 12 positions.

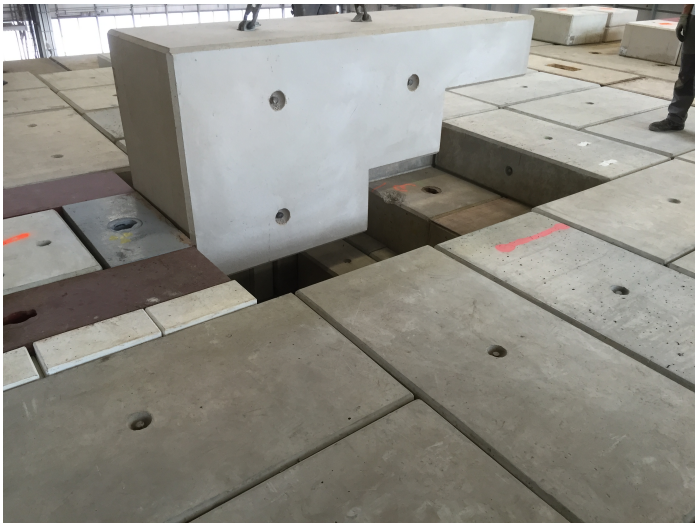

Figure 7.9: Removal of the second dedicated barite concrete block covering the CSBF platform.

7.2.1 Usage of the CSBF platform at 560 cm height:

Compared to the normal operation, the only difference for the scope of the CSBF platform is that the barite concrete covering the irradiation locations is removed. The CSBF platform has been separated in 12 different positions in order to facilitate the documentation of the measurements. This layout of the usage of the CSBF platform can be seen in the Fig. 7.7. Also, the neutron spectra in the 12 different positions of the CSBF platform are presented in Fig. 7.10, showing only negligible differences between the locations.

During operation the ambient dose rate of the platform was measured with a hydrogen-filled ionization chamber in all of the 12 positions and an homogeneity was observed. The results of the ambient dose rate measurements can be found in Tab. 7.3.

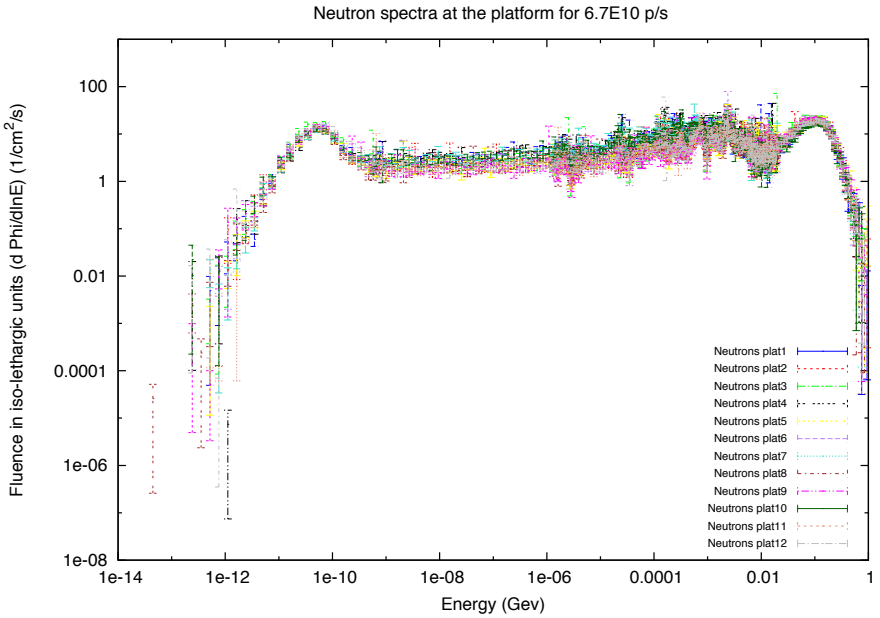

Figure 7.10: Neutron spectra on the 12 different positions on the platform for an average beam intensity of $6.7{\cdot}10^{10}$ protons per second, when the movable shielding is inside the CHARM facility.

Table 7.3: Ambient dose rate (μSv/h) and pSv per primary on target measured on the CSBF platform with an IG5-H20 ionization chamber for different targets for $6.7{\cdot}10^{10}$ p/s average beam intensity.

Targets	Ambient dose rate (μSv/h)	pSv per primary on target
Copper	77.6	63.3
Aluminium	27.3	5.5
Aluminium sieve	10.6	2.4

7.3 Attenuation length measurement at the shielding material test location

The shielding material test location was designed for measuring the spectrum averaged neutron attenuation length (λ) of various shielding materials (e.g. standard concrete, barite concrete, hematite concrete, colemanite concrete, magnetite concrete and cast iron).

To perform these measurements, the removable sample holder concrete block has to be removed from the shaft so that there is a collimated radiation field heading directly to the shielding material test location. The area of this collimated radiation field in 40 cm x 40 cm. The shielding material is then placed in a dedicated shaft with an area of 80 cm x 80 cm, that is centered above the collimated radiation field. FLUKA simulations have been performed and have shown that the contributions from neutrons scattered on the side walls of the shaft and the surrounding shielding structure are less than 3% of the ambient dose equivalent rate due to the lateral cast iron shielding. The current layout of CSBF when the facility is in the material test location mode, is presented in Fig. 7.11.

The available blocks to be inserted into the shielding material test location are of 20, 40 and 80 cm thickness and for each material the ambient dose equivalent rate can be measured up to a shielding thickness corresponding

to approximately 4λ or 5λ (depending on the material). The spectrum averaged attenuation length can then be determined by a second ambient dose equivalent rate measurement with an additional shielding layer, ideally with a thickness of the order of 1λ.

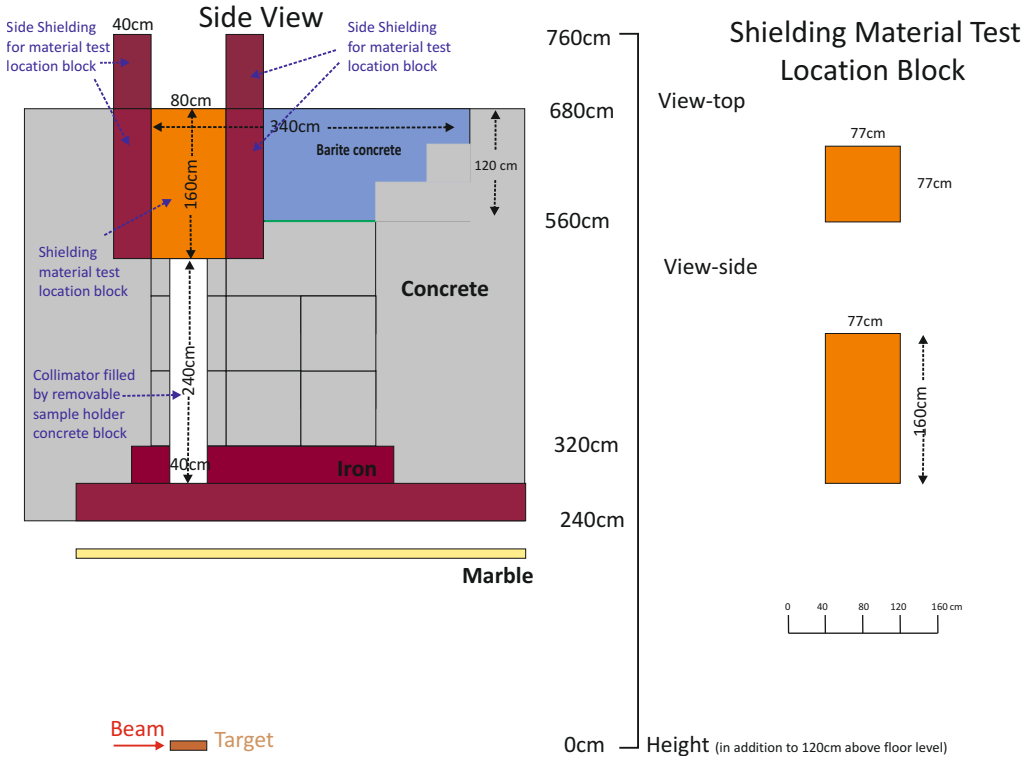

Figure 7.11: CSBF upgrade layout for the Shielding Material Test Location.

7.3.1 Measurement of the attenuation length at the shielding material test location:

The shielding material test location can be filled with the material to be characterized. Two envisaged extreme cases studies, for which FLUKA simulations have been performed, have shown that the side contribution to the ambient dose equivalent dose rate is less than 3% . The first study was performed with cast iron of 100 cm thickness in the shielding material test location (80 cm + optional 20 cm to characterize the 20 cm layer). The second one was concrete of 240 cm thickness (200 cm + optional 40 cm to characterize the 40 cm layer).

The total thickness of shielding material inserted in the shielding material test location can be up to 240 cm, see Fig. 7.11.

Furthermore in the following figures the two above mentioned envisaged studies performed by FLUKA are visualized. Fig. 7.12 and Fig. 7.13 depict the ambient dose equivalent rate on the material test location for the different shielding configurations of 100 cm of iron and 240 cm of concrete. The difference in the neutron spectra in two shielding configurations, the one between 200 cm and 240 cm of concrete and the other between 80 cm and 100 cm of iron are shown in Fig. 7.14 and Fig. 7.15. In Fig. 7.14 and Fig. 7.15 no significant shape change is observed indicating that the deep shielding equilibrium has been reached.

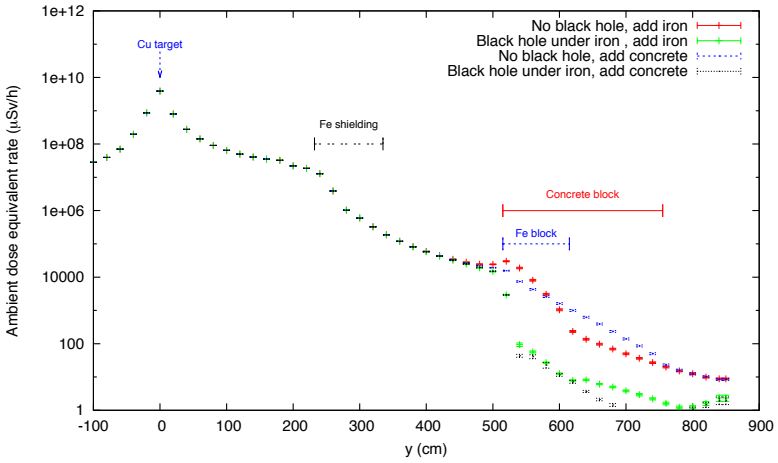

Figure 7.12: Ambient dose equivalent rate as a function of the height above the CHARM target in the shielding material test block location when 100 cm of iron and 240 cm of concrete are added. Two different simulations for FLUKA have been performed without and with blackhole material (i.e. suppressing the direct contribution) under the shielding material test location, for an average beam intensity of $6.7{\cdot}10^{10}$ protons per second.

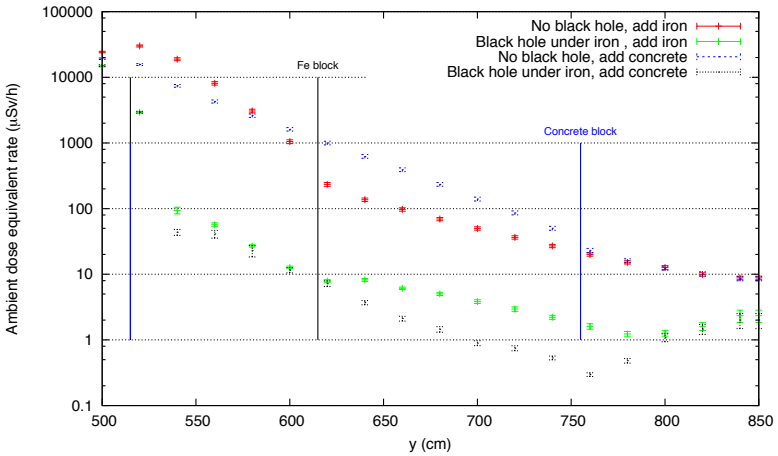

Figure 7.13: Ambient dose equivalent rate as a function of the height above the CHARM target in the shielding material test block location when 100 cm of iron and 240 cm of concrete are added. Two different simulations for FLUKA have been performed without and with blackhole material (i.e. suppressing the direct contribution) under the shielding material test location, for an average beam intensity of $6.7{\cdot}10^{10}$ protons per second.

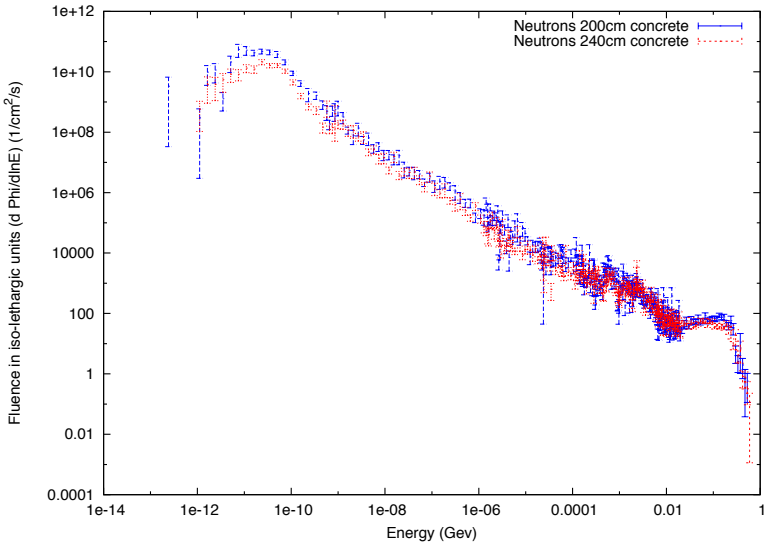

Figure 7.14: Neutron spectra for 200 cm thickness and 240 cm thickness of concrete at the shielding material test block location, for an average beam intensity of $6.7{\cdot}10^{10}$ protons per second.

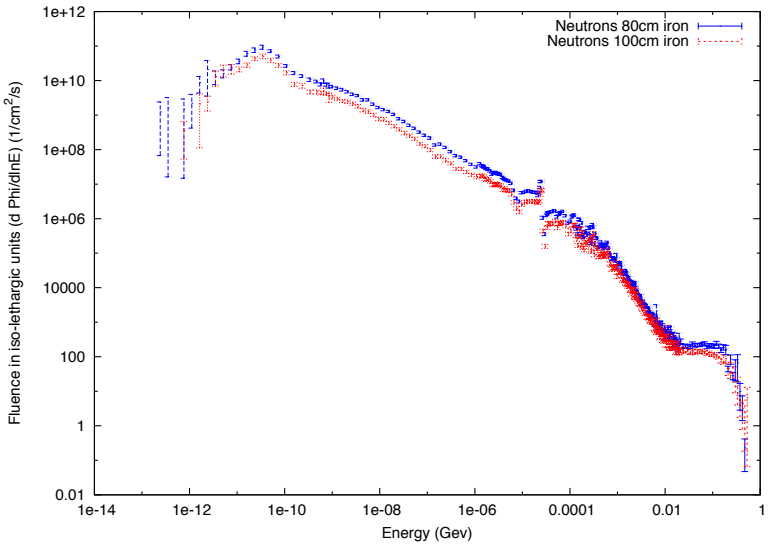

Figure 7.15: Neutron spectra for 80 cm thickness and 100 cm thickness of cast iron at the shielding material test block location, for an average beam intensity of $6.7{\cdot}10^{10}$ protons per second.

Shielding blocks made out of the various materials to be characterized:

The various blocks used in the shielding material test location are 77 cm x 77 cm in horizontal cross-section. The thickness of the blocks is a function of the material, but typically between 20 cm and 80 cm. The density analysis of the different blocks has been performed by weighting each block. The lifting points for transport not at the center of the top face, but moved towards the side, so that the detector does not face any lifting points when it is centered above the block.

The characteristics and the different kind of materials that are used in the shielding material test location are given in Tab. 7.4.

Table 7.4: List of the dedicated blocks to be used in the shielding material test location at the upgraded CSBF.

Material	ID Code	Dimensions(cm^3)	Mass (kg)	Density (g/cm^3)
Standard Concrete	CRJSCXB001-CR000004	80 x 77 x 77	1085	2.29
	CRJSCXB001-CR000005	40 x 77 x 77	550	2.32
	CRJSCXB001-CR000006	40 x 77 x 77	547	2.31
	CRJSCXB001-CR000007	40 x 77 x 77	550	2.32
	CRJSCXB001-CR000008	20 x 77 x 77	290	2.45
	CRJSCXB001-CR000009	20 x 77 x 77	290	2.45
	Removable sample holder concrete block	200 x 37 x 37	610	2.23
Hematite Concrete	CRJSHXB01-CR000019	80 x 77 x 77	1620	3.42
	CRJSHXB01-CR000020	40 x 77 x 77	810	3.42
	CRJSHXB01-CR000021	40 x 77 x 77	820	3.46
	CRJSHXB01-CR000022	20 x 77 x 77	415	3.50
	CRJSHXB01-CR000023	20 x 77 x 77	405	3.42
Barite Concrete	CRJSHXB01-CR000024	80 x 77 x 77	1530	3.23
	CRJSHXB01-CR000025	40 x 77 x 77	795	3.35
	CRJSHXB01-CR000026	40 x 77 x 77	795	3.35
	CRJSHXB01-CR000027	20 x 77 x 77	400	3.37
	CRJSHXB01-CR000028	20 x 77 x 77	400	3.37
Colemanite Concrete	CRJSHXB01-CR000029	80 x 77 x 77	1090	2.30
	CRJSHXB01-CR000030	40 x 77 x 77	550	2.32
	CRJSHXB01-CR000031	40 x 77 x 77	550	2.32
	CRJSHXB01-CR000034	40 x 77 x 77	550	2.32
	CRJSHXB01-CR000032	20 x 77 x 77	280	2.36
	CRJSHXB01-CR000033	20 x 77 x 77	280	2.36
Magnetite Concrete	CRJSHXB01-CR000035	80 x 77 x 77	1740	3.67
	CRJSHXB01-CR000036	40 x 77 x 77	885	3.73
	CRJSHXB01-CR000037	40 x 77 x 77	890	3.75
	CRJSHXB01-CR000038	20 x 77 x 77	445	3.75
	CRJSHXB01-CR000039	20 x 77 x 77	445	3.75
Cast Iron/Stainless Steel		80 x 77 x 77	3645	7.68
Steel S235JRG2		20 x 77 x 77	965	8.14
		20 x 77 x 77	985	8.31
		20 x 77 x 77	985	8.31

7.4 Installation

The installation of the upgraded CSBF has taken place in March and April of 2016. All the blocks were placed in the appropriate positions in order to realize the new version of the CSBF based on the new design of the facility.

This section documents the final configuration of the CSBF after the upgrade.

Figure 7.16: Placement of the removable sample holder concrete block, with the special designed automatic hook used only for this block.

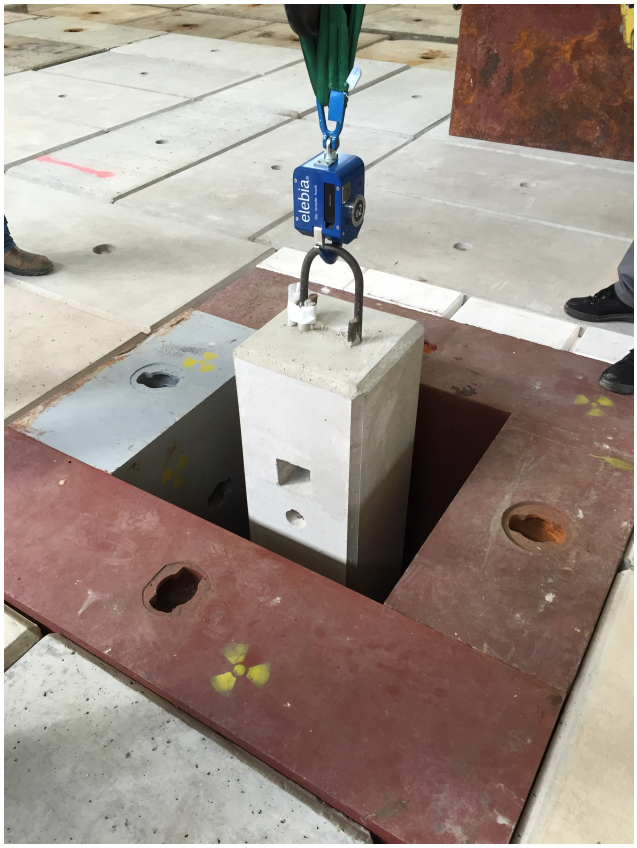

Figure 7.17: Insertion of the removable sample holder concrete block in the dedicated shaft, with the special automatic hook designed only for this block used.

Figure 7.18: Final irradiation position of the removable sample holder concrete block.

Figure 7.19: CSBF platform located at 560 cm above the beam line level.

Figure 7.20: Nominal configuration of the CSBF, with 80 cm of iron and 40 cm concrete shielding. An hydrogen-filled ionization chamber (IG5-H20) is placed on top of the shielding in order to routinely monitor the radiation fields.

Figure 7.21: Measuring the attenuation length of barite concrete with an hydrogen-filled ionization chamber (IG5-H20) at the shielding material test location.

Figure 7.22: Measuring the attenuation length of cast iron with an hydrogen-filled ionization chamber (IG5-H20) at the shielding material test location.

Chapter 8

Commissioning of the upgraded CSBF in 2016

In order to characterize the radiation fields in the upgraded CSBF (see previous chapter 7), activation disk samples made of bismuth, aluminium and indium of different sizes were placed in the upgraded CSBF in July and September 2016. Monte Carlo simulations with the FLUKA code [16,17] have been performed, already in the design phase of the CSBF upgrade (see chapter 7) to estimate the specific production yields of several bismuth isotopes, ^{24}Na and ^{115m}I for these samples. This chapter describes the comparison between the estimated values from FLUKA and the activation measurements performed in July and September 2016 [48].

8.1 Beam parameters and configurations

This section presents the beam parameters and the facility configurations that were used during the activation experiments in September 2016. The beam intensity was measured with a Secondary Emission Chamber, whose measurement values are logged in the CERN measurement database. An intensity calibration factor was applied to the counts per pulse to obtain the number of protons per pulse. This calibration factor had been previously

obtained with aluminium foil activation measurements using sodium isotopes with a statistical uncertainty of 7% of the γ-spectrometry analysis [42].

A beam size of 1.2 cm x 1.2 cm Full Width at Half Maximum (FWHM) was used for the FLUKA simulations as specified in the layout of the beam line and confirmed by online beam profile measurements [42], like in the activation campaign in 2015 that is described in chapter 6.

The average beam intensity of CHARM, binned in 5 minutes long intervals, from July 6 to July 12 and from September 16 to September 22, 2016 when the experiments were conducted, is shown in the Fig. 8.1 and Fig. 8.2 respectively. The first irradiation period corresponds to the irradiation of the aluminum samples, the second to the irradiation of the bismuth samples and the third to the irradiation of the indium samples.

The beam passes through the upstream Proton Irradiation facility (IRRAD) before impacting on the CHARM target. During the period of the experiment, Silicon samples with a total thickness of 0.2 cm were placed into the beam in IRRAD and these samples were also taken properly into account in the FLUKA simulations.

The shielding layout of the CSBF as implemented in the FLUKA simulations is shown in Fig. 7.1. The chemical composition of the concrete, the barite concrete and the cast iron implemented in the FLUKA Monte Carlo simulations for the shielding with their respective densities are listed in Tab. 8.1 and in Tab. 8.2.

During the activation experiment, the cylindrical copper target of 8 cm diameter and 50 cm length has been used inside the CHARM facility. For this activation experiment, only one configuration of the four movable shielding walls, see chapter 2 and more specifically the section 2.2, was used during the different irradiation periods, namely all movable shielding walls retracted from the facility. The configuration has been properly taken into account in the FLUKA Monte Carlo simulations.

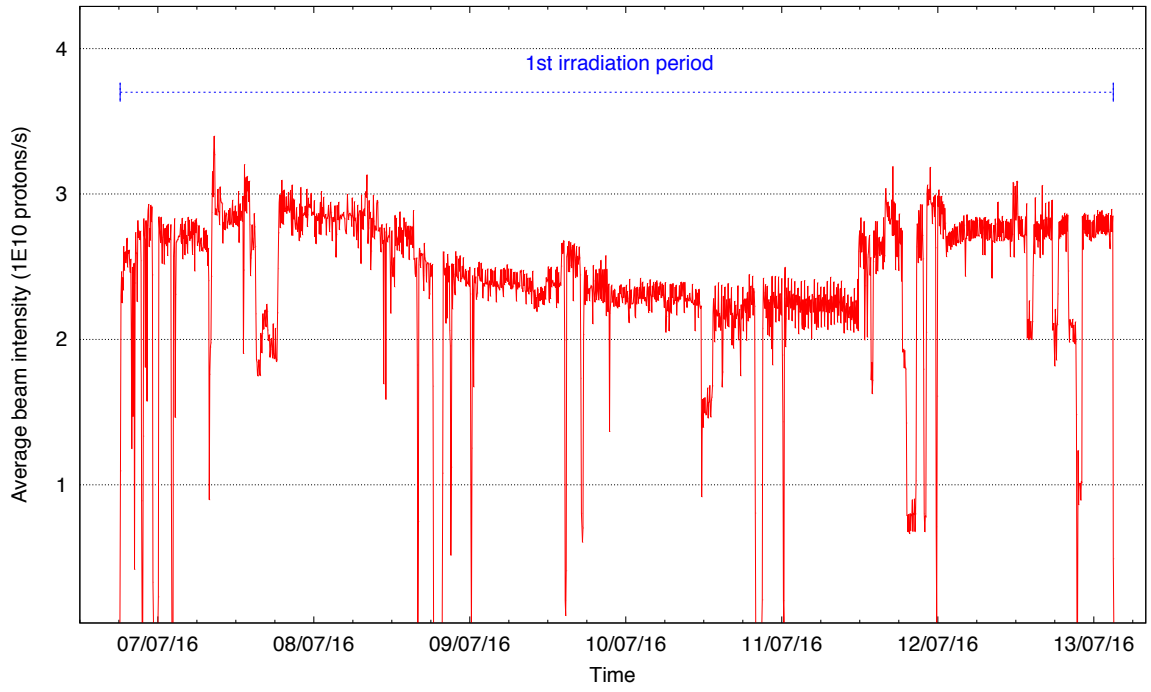

Figure 8.1: Average beam intensity sent to the CHARM facility during the activation experiments with aluminium samples in the removable sample holder concrete block in July 2016 binned in 5 minutes long intervals.

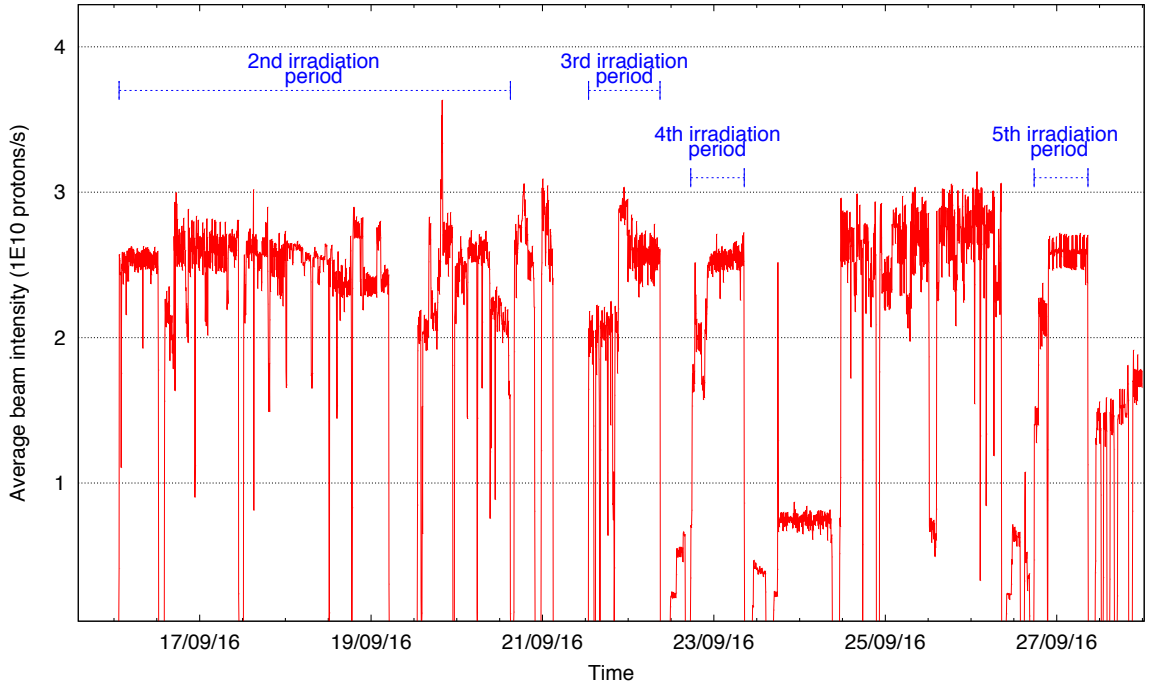

Figure 8.2: Average beam intensity sent to the CHARM facility during the activation experiments in September 2016 binned in 5 minutes long intervals. The 2nd and 3rd irradiation periods correspond to the activation experiments with bismuth and indium samples in the removable sample holder concrete block whereas the 4th and the 5th irradiation periods correspond to the activation experiments with bismuth, aluminium and indium samples in the shielding material test location.

Table 8.1: Chemical composition [43] and density of concrete obtained by measurements.

Concrete	Density 2.35 g/cm^3		
Element	Weight fraction (%)	Element	Weight fraction (%)
Hydrogen	0.561	Silicon	16.175
Carbon	4.377	Sulfur	0.414
Oxygen	48.204	Potassium	0.833
Sodium	0.446	Calcium	23.929
Magnesium	1.512	Titanium	0.173
Aluminium	2.113	Iron	1.263

Table 8.2: Chemical composition [45] and density of cast iron [43].

Cast Iron	Density 7.2 g/cm^3
Element	Weight fraction (%)
Iron	92.3
Carbon	3.85
Manganese	0.3
Silicon	3.4
Phosphorus	0.08
Sulfur	0.02
Cobalt	0.05

8.2 Activation samples and their irradiation

Twenty three disk samples in total, eight bismuth samples, eight aluminium samples and seven indium samples, have been irradiated in 2016. Five bismuth, five aluminium and four indium samples were placed in the removable sample holder concrete block of the CSBF at the 4 positions as indicated in Fig. 7.1. The other three bismuth, three aluminium and three indium samples were placed in the shielding material test location, as indicated in Fig. 7.11, in 3 different thicknesses of normal concrete at 0 cm, 80 cm and 160 cm. All the details of the samples including their location, irradiation time, dimensions, weight, cooling time and duration of γ-spectrometry measurements are presented in Tab. 8.3.

Table 8.3: Description of the irradiated samples and details of the γ-spectrometry measurements.

Sample Material	Irradiation Location	Duration of irradiation (h)	Start of irradiation (date and time)	Dimensions (mm)	Weight (g)	Cooling time (h)	γ-spectrometry measurement duration (h)
Removable sample holder concrete block							
Al	Position 1	149.3	06/07/2016, 18:12 PM	40(diam.)×3	10.4	7	3
	Position 2	149.3	06/07/2016, 18:12 PM	40(diam.)×3	10.4	7	3
	Position 3	149.3	06/07/2016, 18:12 PM	40(diam.)×3	10.4	7	3
	Position 3	149.3	06/07/2016, 18:12 PM	60(diam.)×15	116.9	7	3
	Position 4	149.3	06/07/2016, 18:12 PM	60(diam.)×15	116.9	7	3
Bi	Position 1	109.6	16/09/2016, 01:25 AM	20(diam.)×2	6.23	2	3
	Position 2	109.6	16/09/2016, 01:25 AM	40(diam.)×4	49.5	2	3
						5	12
						26	16
						240	48
	Position 3	109.6	16/09/2016, 01:25 AM	40(diam.)×4	49.52	2	3
						4.5	12
						25.5	16
						187	48
	Position 3	109.6	16/09/2016, 01:25 AM	80(diam.)×10	523.5	2	3
	Position 4	109.6	16/09/2016, 01:25 AM	80(diam.)×10	540.34	2	3
						5	12
						26	16
In	Position 1	20	21/09/2016, 12:55 PM	20(diam.)×2	4.59	6	8
	Position 2	20	21/09/2016, 12:55 PM	40(diam.)×4	36.38	6.5	8
	Position 3	20	21/09/2016, 12:55 PM	80(diam.)×10	375.49	1	3
	Position 4	20	21/09/2016, 12:55 PM	80(diam.)×10	384.77	1.5	3
Shielding material test location							
Al	0 cm	15	22/09/2016, 17:30 PM	40(diam.)×4	13.32	7	18.3
	80 cm	15	26/09/2016, 17:40 PM	80(diam.)×10	135.69	0.75	24
	160 cm	15	22/09/2016, 17:30 PM	80(diam.)×10	134.93	1.2	2
Bi	0 cm	15	22/09/2016, 17:30 PM	40(diam.)×4	49.55	3.4	2.8
						6.5	15
						6.8	48
	80 cm	15	26/09/2016, 17:40 PM	80(diam.)×10	529.42	1.22	2.8
						5.12	18
						23.6	48
	160 cm	15	22/09/2016, 17:30 PM	80(diam.)×10	49.55	1.8	2.8
						5.9	15
						25.4	46
In	0 cm	15	22/09/2016, 17:30 PM	20(diam.)×2	4.61	6	8
	80 cm	15	26/09/2016, 17:40 PM	80(diam.)×10	378.37	1.1	2
	160 cm	15	22/09/2016, 17:30 PM	80(diam.)×10	380.64	1.5	2

8.3 Comparison of FLUKA simulation results to measured production yields

The simulation results were obtained by first scoring the neutron fluence spectra with FLUKA. Then, the neutron fluence was folded with cross section data for the bismuth isotopes, ^{24}Na and ^{115m}I [46], shown in Fig. 8.3, to obtain the predicted production yields per atom per primary proton on the target.

The activities of the bismuth isotopes, ^{24}Na and ^{115m}I were measured for the bismuth, aluminium and indium samples respectively using γ-spectrometry, sometimes even at different cool-down times. In case of multiple samples for the same materials at the same position or multiple γ-spectrometry measurements of the same sample, the activities selected were the ones with the lowest uncertainty of the γ-spectrometry measurements. These activities have been converted to the production yields by taking into account the corresponding irradiation profiles with 5 minutes long binning and the corresponding cool-down times, the same procedure as in the activation campaign 2015 (see chapter 6).

The production yields predicted by FLUKA and measured by γ-spectrometry are presented in Fig. 8.4, Fig. 8.5 and in Tab. 8.5 for the samples placed in the removable sample holder concrete block. The production yields predicted by FLUKA and measured by γ-spectrometry are presented in Fig. 8.8, Fig. 8.9 and in Tab. 8.6 for the samples placed in the shielding material test location. The agreement between FLUKA predictions and γ-spectrometry measurements for the production yields is generally better than a factor of 2. This is illustrated in Fig. 8.6 and Fig. 8.7 for the removable sample holder concrete block and in Fig. 8.10 and Fig. 8.11.

The contributions that have been taken into account for the uncertainty estimation for samples placed in the removable sample holder concrete block and in the shielding material test location are shown in Tab. 8.7 and in Tab. 8.8 respectively. The uncertainty of the sample positions at the given

shielding thicknesses as well as the uncertainty of the beam size have negligible impact on the results as verified by FLUKA simulations. The materials placed in IRRAD during the period of the experiment were taken into account in the simulations. The uncertainty of the production yields coming from the uncertainty of the materials placed in IRRAD is far below 1%.

The uncertainty of the composition of concrete and cast iron as well as the uncertainty of the dimensions of the shielding structure are negligible compared to the uncertainty from the density uncertainty. A hypothetical change in the concrete density would provoke a change on the slope of the dependence of the yields on the depth of the shielding plotted in Fig. 8.4, Fig. 8.5, Fig. 8.8 and Fig. 8.9 and the effect of the change would increase with increased shielding thickness.

The cumulative distribution to the production yields as function of the neutron energy is presented in Fig. 8.12 for the sample placed at a concrete shielding thickness of 160.35 cm in the CSBF. From this figure it can be seen that for Indium-115m and sodium-24, the neutron energy range contributing to the production yield is quite large, larger for the In-115m than the Na-24, whereas for the bismuth isotopes the energy ranges are narrower and located around the respective cross section peaks. The 10%, 25%, 75% and 90% quantiles of the production yield distribution for the various radionuclides, are presented in Tab. 8.4, quantifying the energy range of the neutron field that has been probed by the comparison of the predictions to measurements of the various radionuclides production processes.

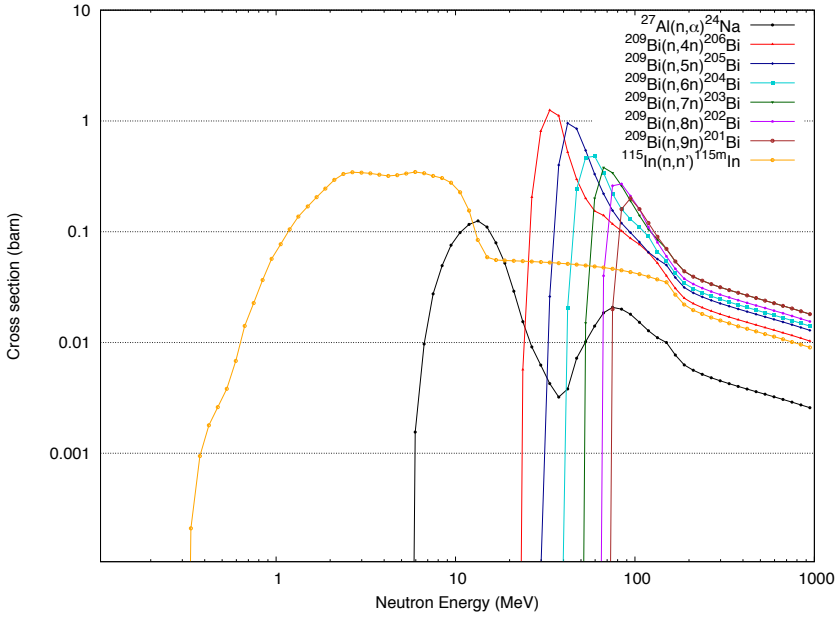

Figure 8.3: Production cross sections of the bismuth isotopes,^{24}Na and ^{115m}I as a function of the neutron energy [46].

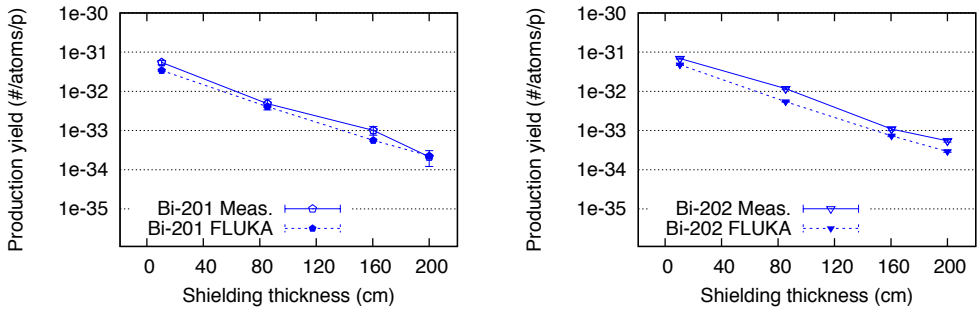

(a) Bi-201

(b) Bi-202

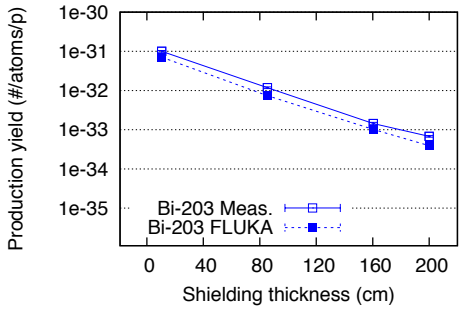

(c) Bi-203

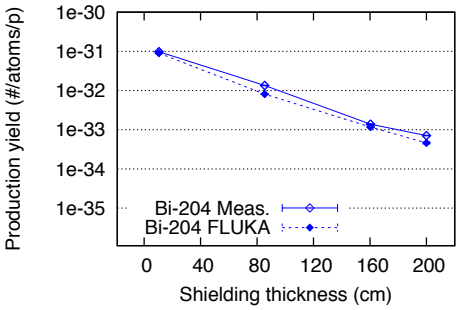

(d) Bi-204

Figure 8.4: Predicted and measured production yields per proton on target for bismuth radionuclides (Bi-201, Bi-202, Bi-203 and Bi-204) as a function of the shielding thickness in the removable sample holder concrete block.

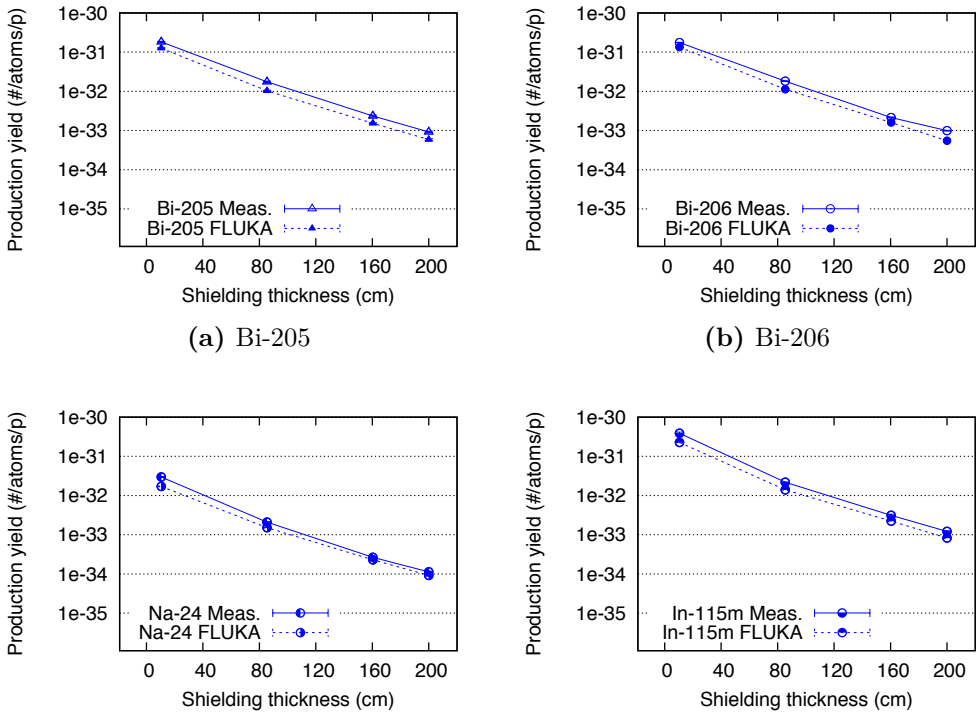

(a) Bi-205 **(b)** Bi-206

(c) Na-24 **(d)** In-115m

Figure 8.5: Predicted and measured production yields per proton on target for bismuth (Bi-205 and Bi-206), sodium and In-115m radionuclides as a function of the shielding thickness in the removable sample holder concrete block.

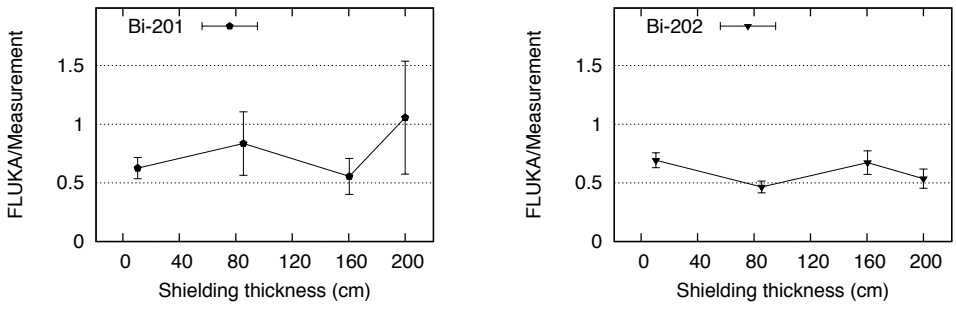

(a) Bi-201

(b) Bi-202

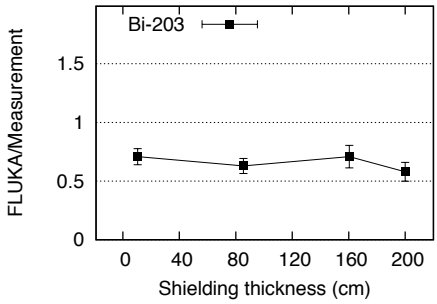

(c) Bi-203

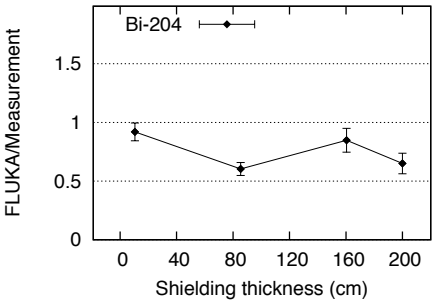

(d) Bi-204

Figure 8.6: The ratio of predicted and measured production yields per proton on target for bismuth radionuclides as a function of the shielding thickness in the removable sample holder concrete block.

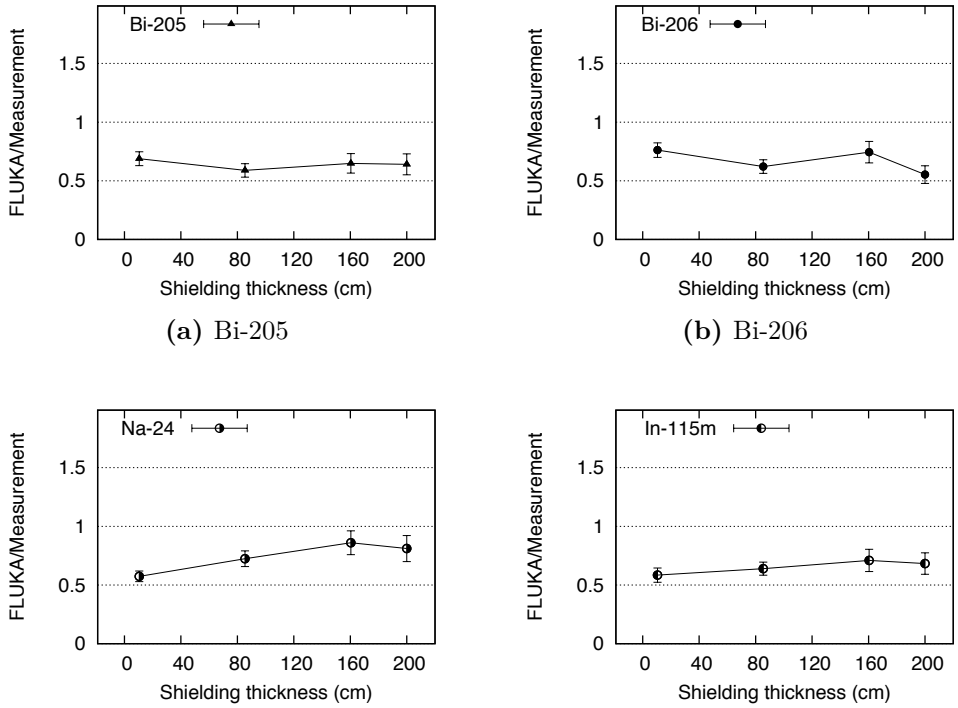

(a) Bi-205 **(b)** Bi-206

(c) Na-24 **(d)** In-115m

Figure 8.7: The ratio of predicted and measured production yields per proton on target for bismuth, sodium and indium radionuclides as a function of the shielding thickness in the removable sample holder concrete block.

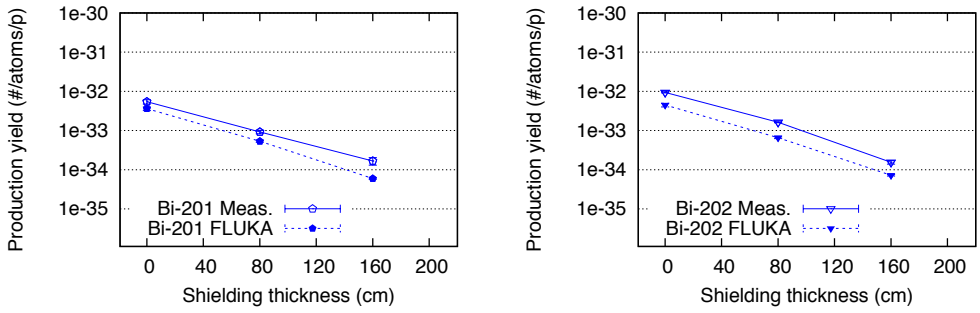

(a) Bi-201

(b) Bi-202

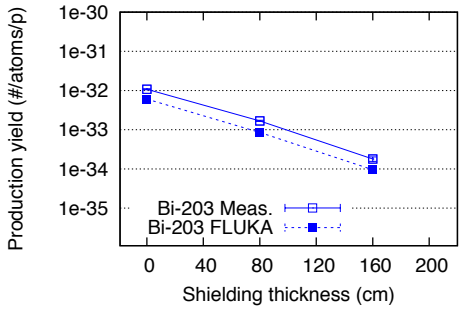

(c) Bi-203

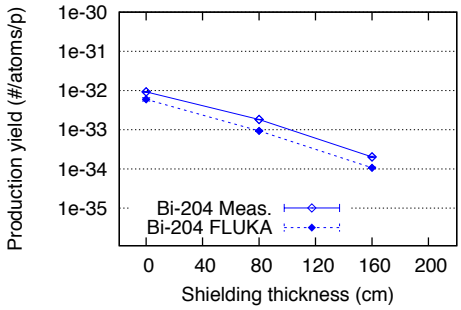

(d) Bi-204

Figure 8.8: Predicted and measured production yields per proton on target for bismuth radionuclides (Bi-201, Bi-202, Bi-203 and Bi-204) as a function of the standard concrete shielding thickness in the shielding material test location.

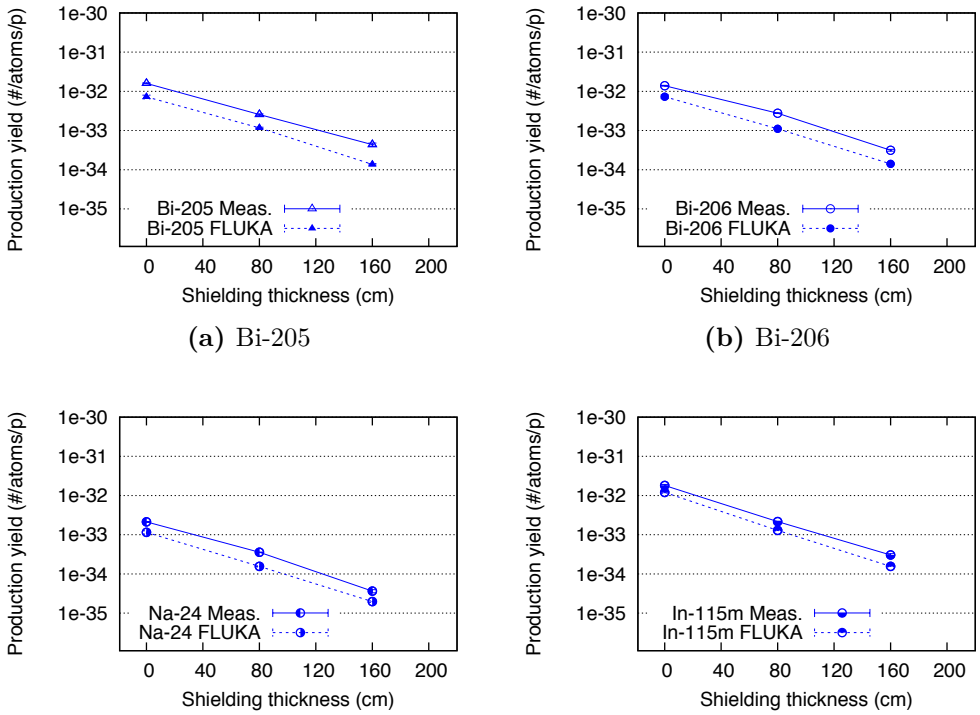

(a) Bi-205 **(b)** Bi-206

(c) Na-24 **(d)** In-115m

Figure 8.9: Predicted and measured production yields per proton on target for bismuth (Bi-205 and Bi-206), sodium and In-115m radionuclides as a function of the standard concrete shielding thickness in the shielding material test location.

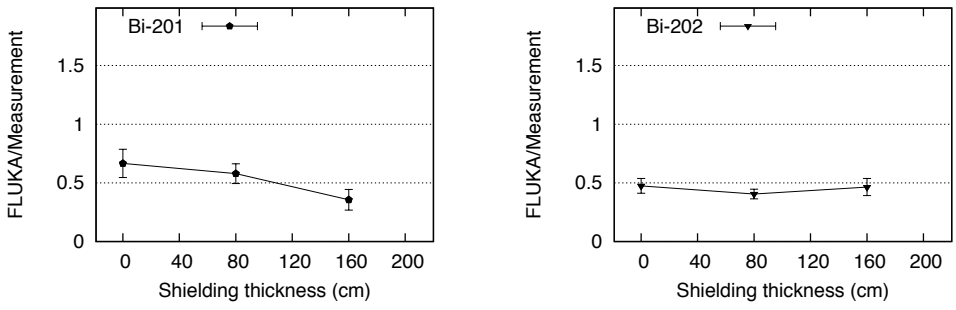

(a) Bi-201

(b) Bi-202

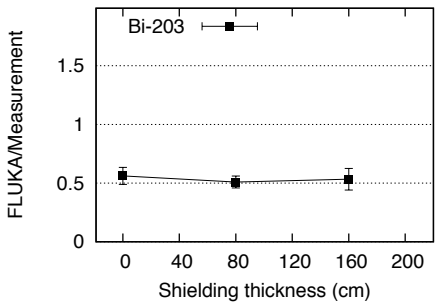

(c) Bi-203

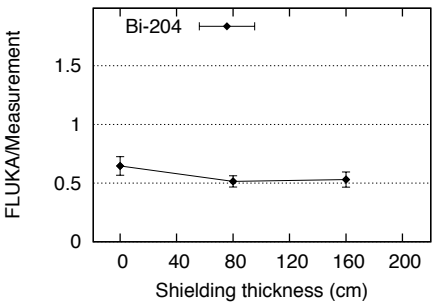

(d) Bi-204

Figure 8.10: The ratio of predicted and measured production yields per proton on target for bismuth radionuclides as a function of the standard concrete shielding thickness in the shielding material test location.

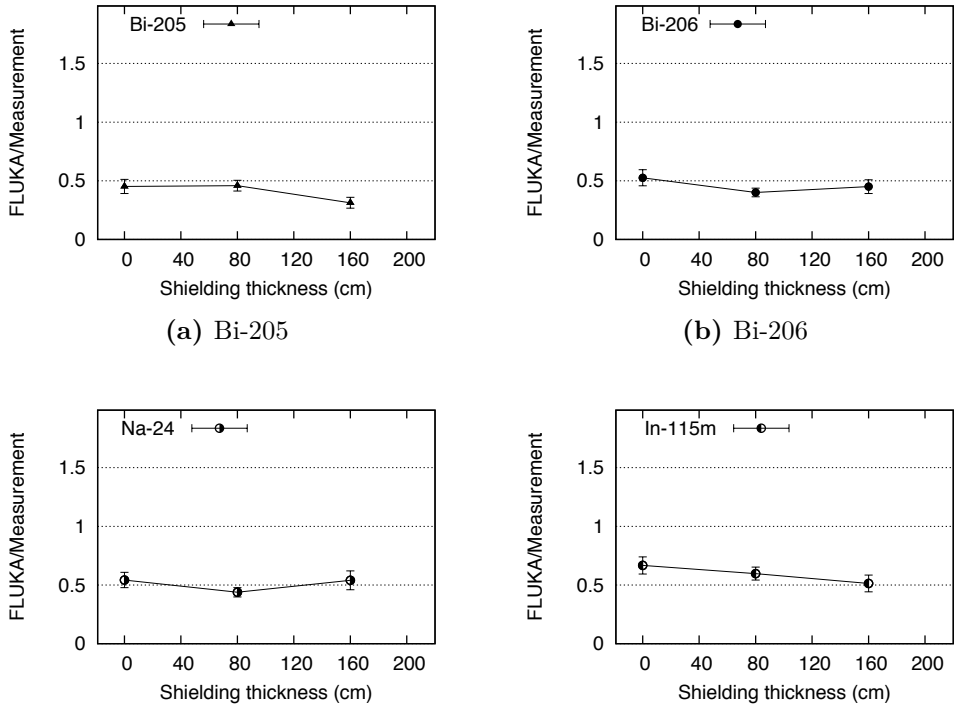

(a) Bi-205 **(b)** Bi-206

(c) Na-24 **(d)** In-115m

Figure 8.11: The ratio of predicted and measured production yields per proton on target for bismuth, sodium and indium radionuclides as a function of the standard concrete shielding thickness in the shielding material test location.

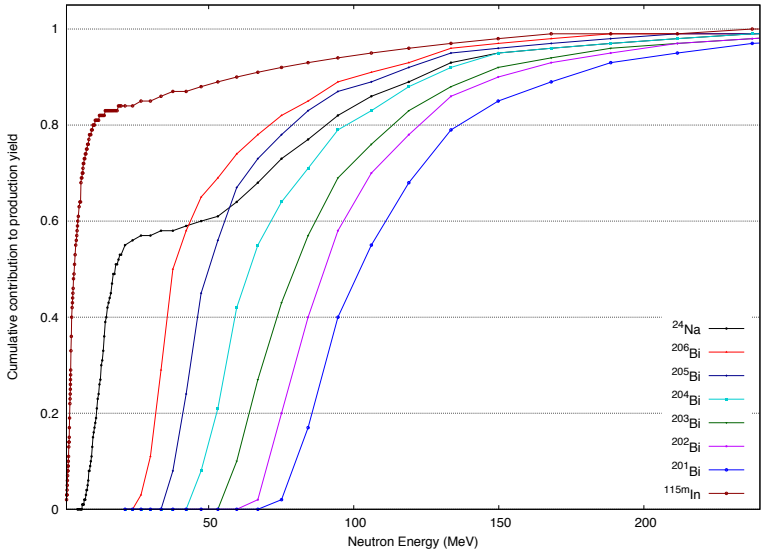

Figure 8.12: Cumulative contribution to the production yields at a concrete shielding thickness of 160.35 cm as a function of the neutron energy for the removable sample holder concrete block.

Table 8.4: The 10%, 25%, 75% and 90% quantiles of the production yield distribution for the various radionuclides at a concrete shielding thickness of 160.35 cm.

	Neutron Energy [MeV]			
Radionuclide	$\mathbf{q_{0.1}}$	$\mathbf{q_{0.25}}$	$\mathbf{q_{0.75}}$	$\mathbf{q_{0.9}}$
Bi-201	79.9	87.8	128	173
Bi-202	70.6	77.4	114	149
Bi-203	59.7	66.1	104	141
Bi-204	48.3	54.4	89.4	126
Bi-205	38.2	42.5	70.2	110
Bi-206	29.5	32.7	61.5	100
Na-24	9.39	12.2	79.7	122
In-115m	1.63	2.33	7.99	59.7

Table 8.5: Predicted production yields by FLUKA and measured production yields by γ-spectrometry for the removable sample holder concrete block.

Radionuclide	Position / Height (cm)	Predicted Production yield by FLUKA (number/atom/p)	Uncertainties FLUKA (%)	Measured Production yield from γ-spect analysis (number/atom/p)	Uncertainties of γ-spect analysis (%)	Ratio Predicted/ Measured	Uncertainties Ratio (%)
Bi-201	1 / 10.5	3.41E-032	±4.64	5.45E-032	±13.72	0.63	±14.50
	2 / 85.4	4.05E-033	±5.80	4.85E-033	±31.88	0.83	±32.40
	3 / 160.35	5.61E-034	±9.92	1.01E-033	±25.77	0.56	±27.61
	4 / 200	2.26E-034	±11.33	2.19E-034	±44.16	1.06	±45.60
Bi-202	1 / 10.5	4.76E-032	±4.50	6.78E-032	±8.01	0.69	±9.20
	2 / 85.4	5.44E-033	±5.71	1.17E-032	±9.09	0.47	±10.74
	3 / 160.35	7.33E-034	±9.68	1.09E-033	±11.32	0.67	±14.90
	4 / 200	2.92E-034	±11.30	5.45E-034	±10.41	0.54	±15.34
Bi-203	1 / 10.5	7.08E-032	±4.11	1.00E-031	±8.78	0.71	±9.69
	2 / 85.4	7.42E-033	±5.60	1.18E-032	±8.54	0.63	±10.20
	3 / 160.35	1.02E-033	±9.36	1.44E-033	±9.76	0.71	±13.52
	4 / 200	3.93E-034	±11.07	6.79E-034	±8.38	0.58	±13.88
Bi-204	1 / 10.5	8.99E-032	±3.94	9.78E-032	±7.25	0.92	±8.26
	2 / 85.4	8.14E-033	±5.53	1.35E-032	±7.20	0.60	±9.08
	3 / 160.35	1.17E-033	±9.31	1.38E-033	±7.50	0.85	±11.96
	4 / 200	4.62E-034	±11.45	7.11E-034	±7.20	0.65	±13.53
Bi-205	1 / 10.5	1.26E-031	±4.00	1.83E-031	±7.58	0.69	±8.57
	2 / 85.4	1.03E-032	±5.65	1.75E-032	±7.92	0.59	±9.73
	3 / 160.35	1.53E-033	±9.40	2.36E-033	±8.72	0.65	±12.82
	4 / 200	5.89E-034	±11.46	9.2E-034	±7.96	0.64	±13.96
Bi-206	1 / 10.5	1.34E-031	±4.01	1.76E-031	±7.14	0.74	±8.20
	2 / 85.4	1.13E-032	±5.91	1.82E-032	±7.25	0.62	±9.35
	3 / 160.35	1.60E-033	±9.71	2.15E-033	±7.50	0.74	±12.30
	4 / 200	5.48E-034	±11.55	9.91E-034	±7.25	0.55	±13.64
Na-24	1 / 10.5	1.71E-032	±3.30	2.98E-032	±7.14	0.57	±7.86
	2 / 85.4	1.52E-033	±5.52	2.10E-033	±7.47	0.72	±9.30
	3 / 160.35	2.28E-034	±9.23	2.65E-034	±7.31	0.86	±11.80
	4 / 200	9.16E-035	±11.20	1.13E-034	±7.96	0.81	±13.74
In-115m	1 / 10.5	2.26E-031	±2.50	3.87E-031	±10.04	0.58	±10.35
	2 / 85.4	1.40E-032	±5.10	2.19E-032	±7.12	0.64	±8.75
	3 / 160.35	2.22E-033	±9.04	3.13E-033	±9.90	0.71	±13.40
	4 / 200	8.26E-034	±10.60	1.21E-033	±8.32	0.68	±13.46

Table 8.6: Predicted production yields by FLUKA and measured production yields by γ-spectrometry for the shielding material test location.

Radionuclide	Position / Height (cm)	Predicted Production yield by FLUKA (number/atom/p)	Uncertainties FLUKA (%)	Measured Production yield from γ-spect analysis (number/atom/p)	Uncertainties of γ-spect analysis (%)	Ratio Predicted/ Measured	Uncertainties Ratio (%)
Bi-201	0	3.61E-033	±10.99	5.42E-033	±14.41	0.67	±18.13
	80	5.34E-034	±7.39	9.23E-034	±12.54	0.58	±14.55
	160	5.94E-035	±9.50	1.67E-034	±22.8	0.36	±24.70
Bi-202	0	4.47E-033	±10.85	9.42E-033	±7.78	0.47	±13.36
	80	6.56E-034	±6.74	1.62E-033	±7.62	0.41	±10.17
	160	7.20E-035	±9.26	1.55E-034	±12.70	0.46	±15.72
Bi-203	0	6.06E-033	±10.47	1.08E-032	±7.54	0.56	±12.90
	80	8.55E-034	±6.16	1.68E-033	±7.83	0.51	±9.96
	160	9.54E-035	±9.21	1.79E-034	±14.59	0.53	±17.25
Bi-204	0	5.96E-033	±10.01	9.23E-033	±7.10	0.65	±12.27
	80	9.36E-034	±5.95	1.82E-033	±7.10	0.51	±9.27
	160	1.07E-034	±9.21	2.02E-034	±8.06	0.53	±12.24
Bi-205	0	7.22E-033	±10.93	1.60E-032	±7.66	0.45	±13.34
	80	1.17E-033	±5.84	2.55E-033	±8.06	0.46	±9.96
	160	1.37E-034	±9.32	4.38E-034	±11.56	0.31	±14.85
Bi-206	0	7.31E-033	±10.76	1.39E-032	±7.31	0.53	±13.01
	80	1.11E-033	±5.71	2.77E-033	±7.20	0.40	±9.19
	160	1.41E-034	±9.51	3.13E-034	±8.84	0.45	±12.98
Na-24	0	1.15E-033	±9.60	2.12E-033	±7.25	0.54	±12.03
	80	1.56E-034	±5.58	3.56E-034	±7.07	0.44	±9.01
	160	1.96E-035	±9.23	3.63E-035	±11.64	0.54	±14.85
In-115m	0	1.20E-032	±5.16	1.80E-032	±9.69	0.67	±10.98
	80	1.29E-033	±5.23	2.16E-033	±7.54	0.60	±9.17
	160	1.56E-034	±8.76	3.04E-034	±10.78	0.51	±13.89

Table 8.7: Uncertainties taken into account for the uncertainty estimation of the production yields for the removable sample holder concrete block.

	Source of uncertainty	Uncertainty on production yield
Simulations	statistical*	1.4 - 5.4 %
	concrete density [1]	0.5 - 10 % [2]
	cast iron density [1]	2 %
Measurements	γ-spectrometry*	1.3 - 14 % [3]
	sample weights	1 %
	beam intensity (calibration)	7 %
	beam intensity (statistical)*	< 1 %
	beam momentum	< 1 %
	beam position and profile	< 1 %
	target density	< 1 %
	target dimensions	< 1 %

* Statistical uncertainty.
[1] Uncertainty of the concrete and cast iron density is 0.05g/cm^3.
[2] The concrete density uncertainty leads to an uncertainty of the production yield of 0.5% for 10.5 cm of concrete and of up to 10% for 200 cm of concrete.
[3] Except for ^{201}Bi at 85.4 cm, 160.35 cm, 200 cm, see Tab. 8.5.

Table 8.8: Uncertainties taken into account for the uncertainty estimation of the production yields for the shielding material test location.

	Source of uncertainty	**Uncertainty on production yield**
Simulations	statistical*	2.6 - 10.8 %
	concrete density [1]	0 - 8.1 % [2]
	cast iron density [1]	2 %
Measurements	γ-spectrometry*	1 - 12.8 % [3]
	sample weights	1 %
	beam intensity (calibration)	7 %
	beam intensity (statistical)*	< 1 %
	beam momentum	< 1 %
	beam position and profile	< 1 %
	target density	< 1 %
	target dimensions	< 1 %

* Statistical uncertainty.
[1] Uncertainty of the concrete and cast iron density is 0.05g/cm^3.
[2] The concrete density uncertainty leads to an uncertainty of the production yield of 0% for 0 cm of concrete and of up to 8.1% for 160 cm of concrete.
[3] Except for ^{201}Bi at 160 cm see Tab. 8.6.

8.4 Summary & Conclusions

The CSBF has been upgraded in 2016, see chapter 7, based on our experience gained through a previous activation campaign in July 2015, in order to facilitate the procedure of sample placement and to add more functionalities in the facility. Based on the results mentioned above [39, 40], FLUKA was used for the design of the upgrade in CSBF (as a reliable Monte Carlo simulation tool).

An activation foil experiment has been conducted at the upgraded CSBF from July 6 to July 26 and September 21 to September 28, 2016. Bismuth, Aluminium and Indium cylindrical samples were placed in the removable sample holder concrete block of the CSBF at different heights. The production yields computed from the activities of the irradiated samples measured by γ-spectrometry have been compared to the estimated production yields from FLUKA Monte Carlo simulations. The agreement is at a level of a factor of 2.

This agreement is good for deep shielding penetration studies and is consistent with previous similar studies at the CERN-EU High Energy Reference Field facility (CERF) [43].

Chapter 9

Experimental attenuation factors for different shielding materials for deep shielding neutron penetration

Studies on the comparison of the attenuation properties of shielding materials currently used, for example concrete, barite concrete and cast iron, as well as proposed protective materials such as colemanite, hematite and magnetite concrete, are conducted at the upgraded CSBF. The obtained attenuation properties will be used in the shielding design studies for future accelerator installations in research institutes as well as in medical facilities.

9.1 Configuration of CSBF

In the CSBF facility the shielding material test location is used to perform attenuation length measurements. During these experiments, the removable sample holder concrete block has to be retracted from the facility and like this a collimated radiation field goes towards the shielding material test location, as discussed in chapter 7, section 7.3. The configuration of the facility during

the attenuation length measurements is shown in Fig. 9.1.

Different shielding materials, with thicknesses of 20, 40 and 80 cm can be placed in the shielding material test location. The details are given in Tab. 7.4.

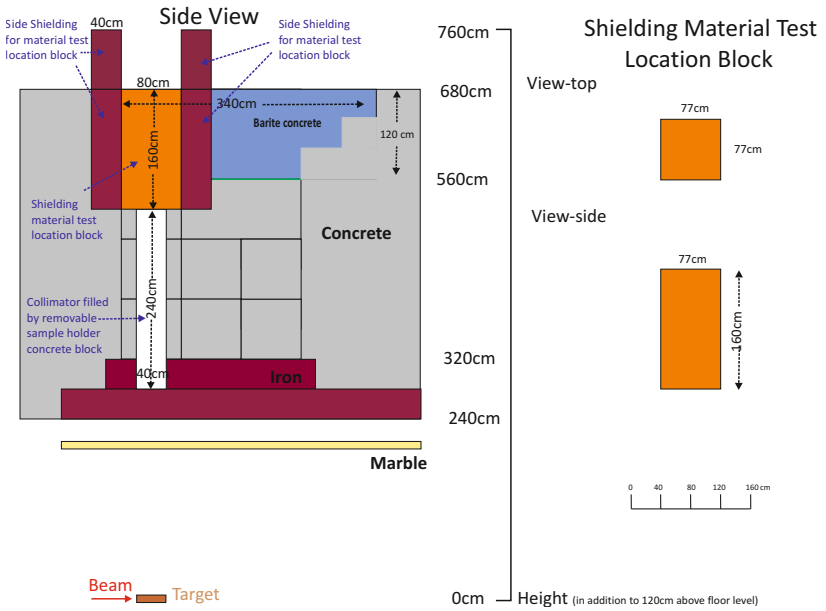

Figure 9.1: CSBF upgrade layout for the Shielding Material Test Location.

9.2 Methodology

A thickness of a specific material, around 4 or 5 times the expected spectrum averaged attenuation length (λ), is placed in the shielding material test location and then the ambient dose equivalent rate can be measured with the use of an hydrogen-filled ionization chamber (IG5) at stable beam intensity. Then an additional shielding block is added, ideally with a thickness of the order of 1λ and a second measurement with an IG5 is performed, preferably keeping the same beam conditions. Thus, the spectrum averaged attenuation length, λ, can be calculated using the following equations :

$$\frac{D_1}{\widetilde{D_2}} = e^{-\frac{1}{\lambda}\cdot(d_1-d_2)}, \tag{9.1}$$

$$\widetilde{D_2} = D_2 \cdot \frac{{R_2}^2}{{R_1}^2}, \tag{9.2}$$

$$\lambda = -\frac{(d_1 - d_2)}{ln(\frac{D_1 \cdot {R_1}^2}{D_2 \cdot {R_2}^2})}, \tag{9.3}$$

where D_1 and D_2 are the ambient dose equivalent per primary proton on target for the first shielding thickness and second shielding thickness. $\widetilde{D_2}$ is the ambient dose equivalent per primary on target, corrected for the increased distance to the target, for the second shielding thickness. The units pSv per primary proton on target derive from the sum of the ambient dose equivalent over the specific irradiation periods and then divided by the number of protons on the target. An intensity calibration factor of $1.87{\cdot}10^7$ protons/count has been applied to the SEC1 counts per spill to obtain the number of protons per spill. The beam intensity and the ambient dose equivalent measurements are shown in Fig. 9.5 and in Fig. 9.6 for the measurements for standard concrete to provide an example.

The quantities d_1 and d_2 correspond to the used thicknesses, in cm. R_1 and R_2 indicate the distance, in cm, from the target for each shielding thickness respectively. Finally, λ is the spectrum averaged neutron attenuation length and is given in cm and $\lambda \cdot \rho$ is the density corrected spectrum averaged neutron attenuation length of the respective shielding material, given in units of $g{\cdot}cm^{-2}$.

Eq. 9.4 and Eq. 9.5 show the uncertainty propagation for the attenuation length:

$$\lambda = f(d, R_1, D_1, D_2) \tag{9.4}$$

For the uncertainty propagation, λ can be written as a function of d, R_1, D_1, D_2, where d equals to the d_2-d_1 and R_2, described in the Eq. 9.2, equals to R_1+d.

Eq. 9.5 gives the formula of the uncertainty propagation of the λ, where the σ_{d} is estimated as 2 mm, $\sigma_{\mathrm{D_1}}$ is the 4% of the value of $\mathrm{D_1}$, $\sigma_{\mathrm{D_2}}$ is the 4% of the value of $\mathrm{D_2}$ and the $\sigma_{\mathrm{R_1}}$ is 2 cm.

$$\sigma_\lambda{}^2 = (\frac{\partial\lambda}{\partial d})^2 \cdot \sigma_{\mathrm{d}}{}^2 + (\frac{\partial\lambda}{\partial D_1})^2 \cdot \sigma_{\mathrm{D_1}}{}^2 + (\frac{\partial\lambda}{\partial R_1})^2 \cdot \sigma_{\mathrm{R_1}}{}^2 + (\frac{\partial\lambda}{\partial D_2})^2 \cdot \sigma_{\mathrm{D_2}}{}^2 \quad (9.5)$$

9.3 Results

The measurements of ambient dose equivalent per primary proton on target are shown in Tab. 9.1 for all irradiation scenarios.

The experimentally determined spectrum averaged attenuation lengths are shown in Tab. 9.2. For the uncertainty of the spectrum averaged neutron attenuation length multiplied by the density, the estimated σ_ρ is the 2% of the density of the corresponding material.

Table 9.1: The dose, in pSv per primary on the target, measured for all the materials available at the shielding material test location.

Shielding materials	**d (cm)**	**D (pSv per primary on target)**
standard concrete	200	$2.82 \cdot 10^{-7}$
	220	$1.48 \cdot 10^{-7}$
	240	$7.74 \cdot 10^{-8}$
barite concrete	160	$5.7 \cdot 10^{-7}$
	180	$2.23 \cdot 10^{-7}$
	200	$1.58 \cdot 10^{-7}$
hematite concrete	160	$3.61 \cdot 10^{-7}$
	180	$1.88 \cdot 10^{-7}$
	200	$1.08 \cdot 10^{-7}$
colemanite concrete	200	$2.83 \cdot 10^{-7}$
	220	$1.62 \cdot 10^{-7}$
	240	$8.90 \cdot 10^{-8}$
magnetite concrete	160	$2.93 \cdot 10^{-7}$
	180	$1.44 \cdot 10^{-7}$
	200	$8.76 \cdot 10^{-8}$
cast iron/ stainless steel	80	$3.93 \cdot 10^{-6}$
	100	$1.61 \cdot 10^{-6}$
	120	$8.43 \cdot 10^{-7}$
	140	$2.55 \cdot 10^{-7}$

Table 9.2: The spectrum averaged neutron attenuation length (λ) and $\lambda \cdot \rho$ as well as their absolute uncertainties for all the materials available measured at the shielding material test location.

Shielding materials	d1 (cm)	d2 (cm)	D_1 (pSv per primary on target)	D_2 (pSv per primary on target)	λ (cm)	$\lambda \cdot \rho$ ($g \cdot cm^{-2}$)
standard concrete	200	240	$2.82 \cdot 10^{-7}$	$7.74 \cdot 10^{-8}$	33.76 ± 1.62	82.72 ± 4.32
barite concrete	160	200	$5.7 \cdot 10^{-7}$	$1.58 \cdot 10^{-7}$	34.22 ± 1.67	115.34 ± 6.11
hematite concrete	160	200	$3.61 \cdot 10^{-7}$	$1.08 \cdot 10^{-7}$	36.62 ± 1.91	126.70 ± 7.10
colemanite concrete	200	240	$2.83 \cdot 10^{-7}$	$8.90 \cdot 10^{-8}$	38.14 ± 2.06	90.02 ± 5.24
magnetite concrete	160	200	$2.93 \cdot 10^{-7}$	$8.76 \cdot 10^{-8}$	36.59 ± 1.90	137.23 ± 7.71
cast iron/stainless steel	80	140	$3.93 \cdot 10^{-6}$	$2.55 \cdot 10^{-7}$	23.58 ± 0.53	194.54 ± 5.85

The average beam intensity of CHARM, binned in 5 minutes long intervals, for September 2016 and August 2017 when the attenuation length experiments were conducted, is shown in Fig. 9.2 and in Fig. 9.3 respectively.

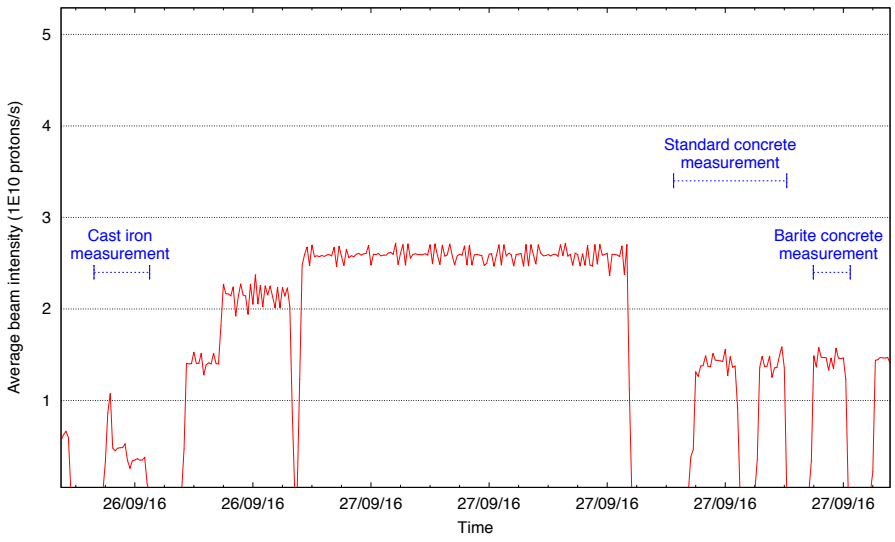

Figure 9.2: Average beam intensity sent to the CHARM facility during the attenuation length experiment at the shielding material test location in 2016 with binning of 5 minutes long intervals.

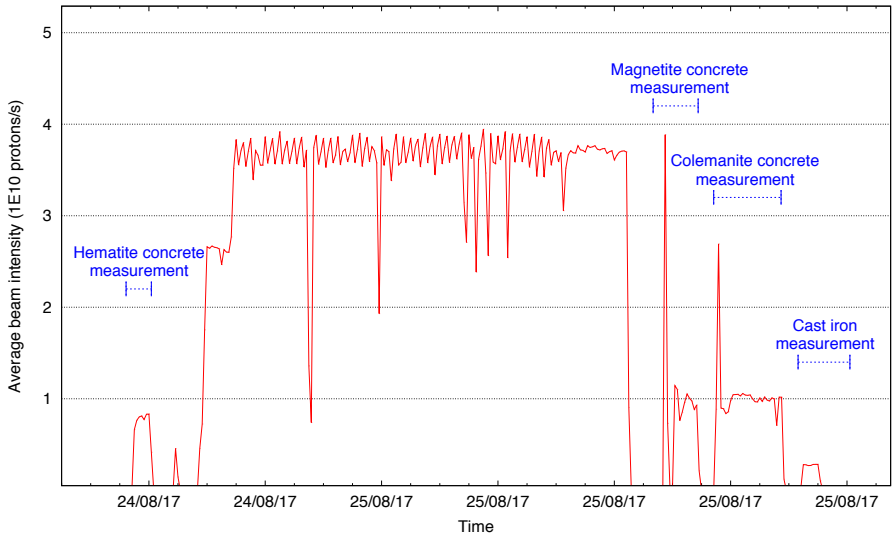

Figure 9.3: Average beam intensity sent to the CHARM facility during the attenuation length experiment at the shielding material test location in 2017 with binning of 5 minutes long intervals.

The spectrum averaged attenuation length λ has been experimentally determined for six materials, as shown in Fig. 9.2 and Fig. 9.3. The materials are given in Tab. 7.4 and Tab. 9.1.

The beam intensity and ambient dose equivalent measurements for standard concrete are shown in Fig. 9.4, Fig. 9.5 and Fig. 9.6, to provide an example. More specifically, the average beam intensity of CHARM, binned in 5 minutes long intervals, for September 27, 2016 when the attenuation length experiment for standard concrete was conducted, is shown in the Fig. 9.4. The 6 different irradiation periods used during the measurements are also indicated in Fig. 9.4. Fig. 9.5 and Fig. 9.6 show the beam intensity per spill (protons on target) and the ambient dose equivalent (μSv) per 1.2 s measurement interval for the same 6 measurement periods for the standard concrete, respectively.

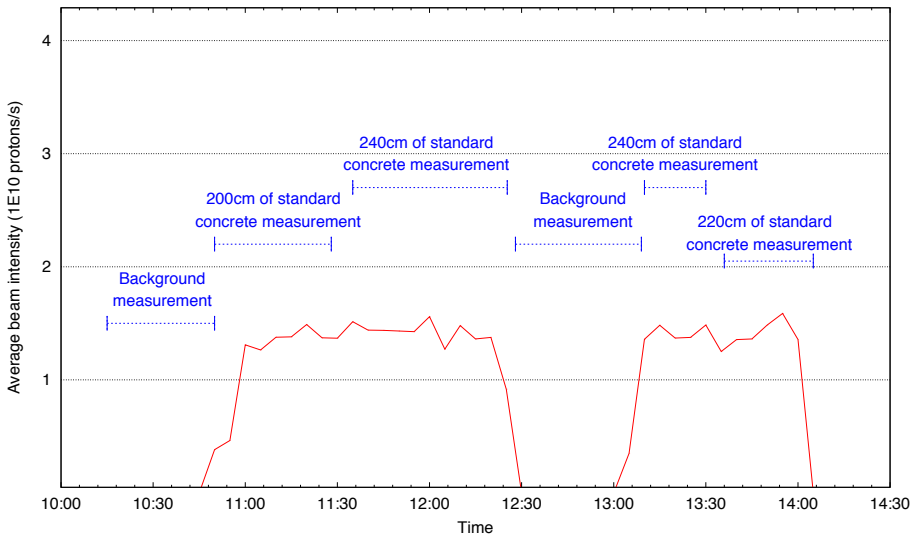

Figure 9.4: Average beam intensity sent to the CHARM facility during the attenuation length experiment at the shielding material test location for standard concrete in 2016 with binning of 5 minutes long intervals.

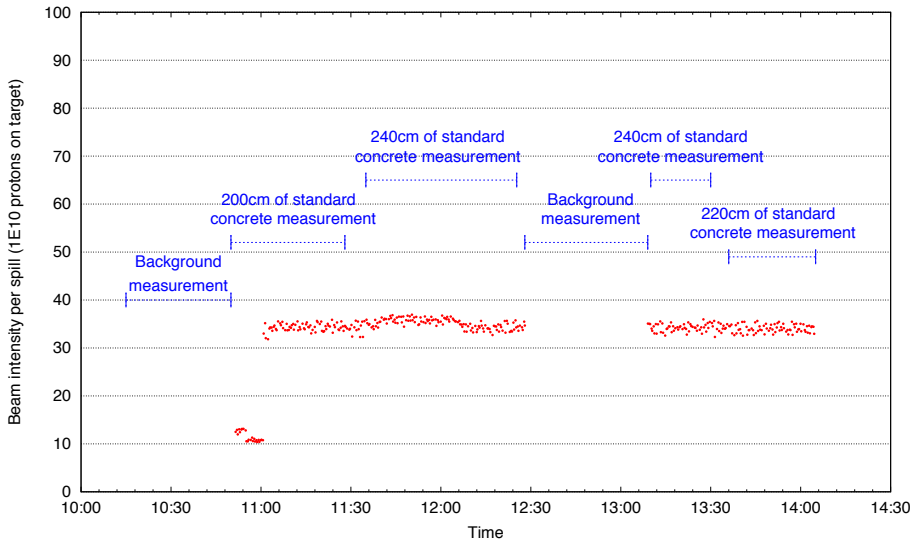

Figure 9.5: Beam intensity per spill (protons on target) sent to the CHARM facility during the attenuation length experiment at the shielding material test location for standard concrete in 2016.

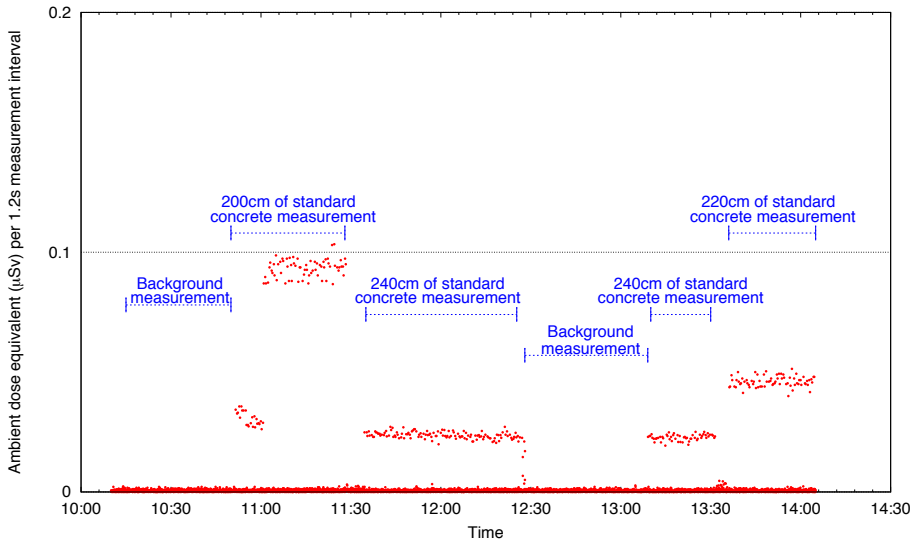

Figure 9.6: Ambient dose equivalent (μSv) per 1.2 s measurement interval, measured at the shielding material test location of CSBF for the standard concrete attenuation length measurement.

9.4 Summary

Attenuation length measurements were performed at the shielding material test location of the CSBF, for six available shielding materials. From the measurements of the ambient dose equivalent, the spectrum averaged neutron attenuation length (λ) and the density corrected spectrum averaged neutron attenuation length ($\lambda \cdot \rho$) were calculated. A disagreement was found for neutron fields at 90° (the CSBF is located laterally at 90° above the CHARM target and the beam line) compared to high energy particle attenuation mean free paths in various target and shielding materials given in the bibliography [27], typically for lower energetic neutron spectra. Therefore, further experimental investigations are needed to understand this discrepancy of the results.

The fact that the FLUKA Monte Carlo simulation code describes attenuation by shielding well, underlines the need for Monte Carlo simulations in shielding design in general and for validation of these results.

Conclusions

The installation of the first prototype of the CSBF was completed during the Long Shut-down 1 (LS1) in 2013/2014, together with the installation of the CHARM facility.

An activation campaign has been conducted from July 9 to July 15, 2015 in the CHARM and the CSBF facility. Bismuth and aluminium disk samples were placed in different locations in the prototype CSBF, and inside the CHARM facility access corridor. The production yields computed from the activities of the irradiated samples, measured from γ-spectrometry, have been compared to the estimated values from FLUKA Monte Carlo simulations. The agreement is better than a factor of 2.

Therefore, from our experience gained through the activation campaign in July 2015, we decided to upgrade the CSBF in 2016 in order to facilitate the procedure of sample placement, and to add more functionalities to the facility. Since the results obtained during the activation in 2015 confirmed FLUKA as a very reliable Monte Carlo simulation tool, the design of the upgrade of the CSBF in the first months of 2016 has been based on FLUKA simulations.

Thus, an activation foil experiment has been conducted at the upgraded CSBF from July 6 to July 26 and September 21 to September 28, 2016. Bismuth, Aluminium and Indium cylindrical samples, were placed in the removable sample holder concrete block and at the shielding material test location of the CSBF at different heights. The production yields computed from the activities of the irradiated samples, measured by γ-spectrometry,

have been compared to the estimated production yields from FLUKA Monte Carlo simulations. The agreement is at a level of a factor of 2.

The results obtained by both activation campaigns in 2015 and in 2016, show that the agreement between the measured values by γ-spectrometry and the estimated production yields from FLUKA Monte Carlo simulations, is good for deep shielding penetration studies and is consistent with previous similar studies at the CERN-EU High Energy Reference Field facility (CERF).

The measurements performed to the shielding material test location to estimate the spectrum averaged attenuation length λ, were performed for several commonly used shielding materials, by measuring the ambient dose equivalent rate measured for two different thicknesses, in order to characterize the different available materials and understand their shielding properties. These materials, can be used in the shielding design studies for future accelerator installations in research institutes, as well as in medical facilities.

The CSBF is now well described and characterized by means of measurements and FLUKA simulations and it will be opened to the scientific community for further experiments.

Συμπεράσματα

Η εγκατάσταση του πρώτου πρωτότυπου του CSBF ολοκληρώθηκε κατά τη διάρκεια του Long Shut-down 1 (LS1) το 2013/2014, μαζί με την εγκατάσταση του CHARM.

Μια εκστρατεία πειραμάτων ενεργοποίησης διεξήχθη από τις 9 Ιουλίου έως τις 15 Ιουλίου 2015 στην εγκατάσταση του CHARM και στο CSBF. Δείγματα δίσκων βισμουθίου και αλουμινίου τοποθετήθηκαν σε διαφορετικές θέσεις στο πρωτότυπο CSBF και μέσα στο διάδρομο πρόσβασης της εγκατάστασης του CHARM. Οι αποδόσεις παραγωγής που υπολογίστηκαν από τις μετρήσεις ραδιενέργειας των ακτινοβολημένων δειγμάτων, που μετρήθηκαν από τη γ-φασματομετρία, έχουν συγκριθεί με τις εκτιμώμενες τιμές των αποδόσεων παραγωγής, από τις προσομοιώσεις FLUKA Monte Carlo. Η συμφωνία είναι καλύτερη από έναν παράγοντα 2.

Ως εκ τούτου, από την εμπειρία που αποκτήθηκε μέσω της εκστρατείας ενεργοποίησης τον Ιούλιο του 2015, αποφασίσαμε να αναβαθμίσουμε το CSBF το 2016 προκειμένου να διευκολυνθεί η διαδικασία της τοποθέτησης δειγμάτων και να προστεθούν περισσότερες λειτουργίες στην εγκατάσταση. Δεδομένου ότι τα αποτελέσματα που προέκυψαν κατά τα πειράματα ενεργοποίησης το 2015, επιβεβαίωσαν ότι η FLUKA είναι ένα πολύ αξιόπιστο εργαλείο προσομοίωσης Monte Carlo, ο σχεδιασμός της αναβάθμισης του CSBF κατά τους πρώτους μήνες του 2016 βασίστηκε σε προσομοιώσεις FLUKA.

Έτσι, διεξήχθη ένα πείραμα ενεργοποίησης δειγμάτων στο αναβαθμισμένο CSBF από τις 6 Ιουλίου έως τις 26 Ιουλίου και από τις 21 Σεπτεμβρίου έως τις 28 Σεπτεμβρίου 2016. Τα κυλινδρικά δείγματα βισμουθίου, αλουμινίου και ινδίου, τοποθετήθηκαν σε διαφορετικά ύψη στο removable sample holder concrete block και στο shielding material test location. Οι αποδόσεις παραγωγής που υπολογίστηκαν από τις μετρήσεις ραδιενέργειας των ακτινοβοληµένων δειγμάτων, που μετρήθηκαν με γ-φασματομετρία, έχουν συγκριθεί με τις εκτιμώμενες αποδόσεις παραγωγής από τις προσομοιώσεις FLUKA Monte Carlo. Η συμφωνία είναι στο επίπεδο του παράγοντα 2.

Τα αποτελέσματα που προέκυψαν από τις δύο εκστρατείες ενεργοποίησης το 2015 και το 2016, δείχνουν ότι η συμφωνία μεταξύ των μετρούμενων τιμών με τις μετρήσεις γ-φασματοσκοπίας και τις εκτιμώμενες αποδόσεις παραγωγής από τις προσομοιώσεις FLUKA Monte Carlo, είναι καλή για μελέτες διείσδυσης σωματιδίων σε βαθιά θωράκιση και είναι σύμφωνη με παλαιότερες παρόμοιες μελέτες στην εγκατάσταση CERN-EU High Field Reference Field (CERF).

Οι μετρήσεις που διεξήχθησαν στο shielding material test location για την εκτίμηση του μέσου όρου του μήκους εξασθένησης, λ, φάσματος νετρονίων, πραγματοποιήθηκαν για αρκετά κοινά χρησιμοποιούμενα υλικά θωράκισης, με μέτρηση του ρυθμού ισοδύναμης δόσης περιβάλλοντος που μετρήθηκε για δύο διαφορετικά πάχη, προκειμένου να χαρακτηριστούν τα διαφορετικά διαθέσιμα υλικά και να κατανοηθούν οι ιδιότητες θωράκισης τους. Αυτά τα υλικά θωράκισης, μπορούν να χρησιμοποιηθούν στις μελέτες σχεδιασμού θωράκισης για μελλοντικές εγκαταστάσεις επιταχυντών σε ερευνητικά ιδρύματα καθώς και σε ιατρικές εγκαταστάσεις.

Το CSBF είναι πλέον καλά περιγραφόμενο και χαρακτηρισμένο με μετρήσεις και προσομοιώσεις FLUKA και θα ανοίξει στην επιστημονική κοινότητα για περαιτέρω πειράματα.

Appendix

The publications related to this thesis are listed below:

1. E. Iliopoulou et al., *Measurements and FLUKA Simulations of Bismuth and Aluminum Activation at the CERN Shielding Benchmark Facility (CSBF)*, Proceedings of SATIF 13, Dresden, Germany, (2016)

2. A. Curioni, R. Froeschl, M. Glaser, E. Iliopoulou, F.P. La Torre, F. Pozzi, F. Ravotti, M. Silari, *Single- and multi-foils ^{27}Al (p,3pn) ^{24}Na activation technique for monitoring the intensity of high-energy beams*, Nuclear Instruments and Methods in Physics Research A 858, (2017) p. 101–105

3. E. Iliopoulou et al., *Measurements and FLUKA simulations of bismuth and aluminium activation at the CERN Shielding Benchmark Facility (CSBF)*, Nuclear Instruments and Methods in Physics Research A 885,(2018) p. 79–85

4. E. Iliopoulou et al., *Measurements and FLUKA Simulations of Bismuth, Aluminium and Indium Activation at the CERN Shielding Benchmark Facility (CSBF)*, Proceedings of ARIA 17, Lund, Sweden, 2018 J. Phys.: Conf. Ser. **1046** 012004

5. T. Kajimoto, T. Sanami, N. Nakao, R. Froeschl, S. Roesler, E. Iliopoulou, A. Infantino, M. Brugger, E. Lee, N.Shigyo, M. Hagiwara, H. Yashima, H. Yamazaki, K. Tanaka, S. Endo, *Neutron energy spec-*

trum measurement using NE213 scintillator at CHARM, Nuclear Instruments and Methods in Physics Research B 429, (2018) p. 27–33

6. T. Oyama, M. Hagiwara, T. Sanami, H. Yashima, N. Nakao, E.J. Lee, E. Iliopoulou, R. Froeschl, A. Infantino, S. Roesler, *Measurement and calculation of thermal neutrons induced by the 24 GeV/c proton bombardment of a thick copper target*, Nuclear Instruments and Methods in Physics Research B 434, (2018) p. 29–36

7. T. Kajimoto, T. Sanami, N. Nakao, R. Froeschl, S. Roesler, E. Iliopoulou, A. Infantino, M. Brugger, K. Tanaka, S. Endo, *Reproduction of neutron fluence by unfolding method with an NE213 scintillator*, Nuclear Instruments and Methods in Physics Research A 906, (2018) p. 141–149

List of Tables

List of Figures

Bibliography

[1] L. Evans and P. Bryant (editors), *LHC Machine*, Journal of Instrumentation 3(08):S080001.

[2] ATLAS Collaboration, G. Aad et al., *The ATLAS Experiment at the CERN Large Hadron Collider*, Journal of Instrumentation 3(08):S080003.

[3] ALICE Collaboration, K. Aamodt et al., *The ALICE experiment at the CERN LHC*, Journal of Instrumentation 3(08):S080002.

[4] CMS Collaboration, S. Chatrchyan et al., *The CMS experiment at the CERN LHC*, Journal of Instrumentation 3(08):S080004.

[5] LHCb Collaboration, A. Augusto Alves et al., *The LHCb Detector at the LHC*, Journal of Instrumentation 3(08):S080005.

[6] https://www.cern.ch/charm/.

[7] https://www.cern.ch/r2e/.

[8] M. Brugger, *Radiation Damage to Electronics at the LHC*, Proceedings IPAC-2012-THPPP006 (Presentation given at Conference C12-05-20.1) (2012) 3734–3736.

[9] M. Brugger et al., *FLUKA Capabilities and CERN Applications for the Study of Radiation Damage to Electronics at High-Energy Hadron Accelerators*, Atomic Energy Society of Japan, in progress in NUCLEAR

SCIENCE and TECHNOLOGY (Presentation given at SNA+MC 2010, October 17-21,2010, Tokyo, Japan) (2011) 948–954.

[10] R. Froeschl, M. Brugger, S. Roesler, *The CERN High Energy Accelerator Mixed Field (CHARM) facility in the CERN PS East Experimental Area*, Tech. Rep. Presentation given at the SATIF 12, on 28/04/2014, EDMS 1467128 (2014).

[11] J. Mekki, M. Brugger, R.G. Alia, A. Thornton, N.C. Dos Santos Mota, S. Danzeca, *CHARM: A Mixed Field Facility at CERN for Radiation Tests in Ground, Atmospheric, Space and Accelerator Representative Environments*, IEEE TRANSACTIONS ON NUCLEAR SCIENCE, VOL. 63, NO. 4 (2016) 2106–2114.

[12] L. Gatignon, *Beam Properties for the East Area Irradiation Facility in the T8 Beam Line*, Tech. Rep. EAT8, EDMS 1270807 (2013).

[13] R. Froeschl, *Radiation Protection Assessment of the Proton Irradiation facility and the CHARM facility in the East Area*, Tech. Rep. CERN-RP-2014-008-REPORTS-TN, EDMS 1355933 (2014).

[14] A. Thorton, *CHARM Facility Test Area Radiation Field Description*, Tech. Rep. CERN-ACC-NOTE-2016-12345 (2016).

[15] F. Ravotti, *Personal Communication*.

[16] T.T. Bohlen et al, *The FLUKA Code: Developments and Challenges for High Energy and Medical Applications*, Nuclear Data Sheets 120 (2014) 212–214.

[17] A. Fassò, A. Ferrari, J. Ranft and P.R. Sala, *FLUKA: a multi-particle transport code*, Tech. Rep. CERN-2005-10 (2005), INFN/TC-05/11, SLAC-R-773.

[18] R. Froeschl, *The DORIAN code for the prediction and analysis of residual dose rates due to accelerator radiation induced activation*, Proceedings of the AccApp13 Conference 2013 (Brugge 5-8 August 2013).

[19] M. Huhtinen, *Determination of cross-sections for assessments of air activation at LHC*, Tech. Rep. CERN/TIS-RP/TM/97-29 (1997).

[20] M. Brugger, D. Forkel-Wirth, S. Roesler and P. Vojtyla, *Effective Dose to the Public from Air Releases at LHC Point 7*, Tech. Rep. CERN–SC–2004–064–RP–TN, EDMS 493681.

[21] S. F. Council, *Swiss Radiological Protection Ordinance (RPO)* (22 June 1994, Status as of 1 January 2014, Reference 841.501).

[22] P. Vojtyla, *Models for environmental impact assessments of releases of radioactive substances from CERN facilities*, Tech. Rep. CERN–SC–2005–005–IE, EDMS 607969.

[23] C. Patrignani et al (Particle Data Group), Chinese Phys. C,**40**, 100001 (2016) and 2017 update.

[24] Barbier, M., *Induced Radioactivity*, North-Holland, Amsterdam, 1969.

[25] Gnell F. Knoll, *Radiation Detection and Measurement*, John Wiley & Sons, Inc., 2000.

[26] J. ao Pedro Saraiva, *Radiological Characterization of TFA metallic tubes from CERN Accelerator Complex* (2012).

[27] A.H. Sullivan, *A Guide to Radiation and Radioactivity Levels near High Energy Particle Accelerators*, Nuclear Technology Publishing, Ashford, Kent, TN23 1JW, 1992.

[28] K. Nakamura et al (Particle Data Group) 2010 J. Phys. G: Nucl. Part. Phys. 37 075021.

[29] R.H. Thomas, G.R. Stevenson, *Radiation Safety Aspects of the Operation of Proton Accelerators*, IAEA Technical Report Series No. 282, Vienna (1988) Ch 4, Radiation Shielding, 223.

[30] Cossairt, J. D., *Radiation Physics for Personnel and Environmental Protection, Revision 9B*, Tech. Rep. FERMILAB-TM-1834, 2007.

[31] N. Walter, *Development of an In-Situ Radiological Classification Technique for Material from CERN's Accelerator Facilities* (2015).

[32] R. Froeschl, M. Magistris, F. Leite Pereira, C. Theis, *Computation of radioactivity in particle accelerators and propagation of uncertainties with the JEREMY code*, Tech. Rep. CERN-RP-2014-065-REPORTS-TN (2014).

[33] Bateman, H., *Solution of a system of differential equations occurring in the theory of radioactive transformations*, Proc. Cambridge Philos. Soc. 15 (1910) 423–427.

[34] Shultis, J. K. and Faw, R. E., *Fundamentals of nuclear science and engineering*, Dekker, Abingdon, 2002.

[35] N. Nakao, *Personal Communication* (2017).

[36] G. Battistoni et al., *The Application of the Monte Carlo Code FLUKA in Radiation Protection Studies for the Large Hadron Collider*, Progress in Nuclear Science and Technology, Vol.2 358–364.

[37] A. Mereghetti, *Shielding Data for 100-250 MeV Proton Accelerators: Double Differential Neutron Distributions and Attenuation in thick concrete, iron and concrete/iron shields* (2007).

[38] N. Nakao, Y. Uwamino, K. Tanaka, *Measurement of neutrons generated by 345MeV/u U-238 beam at RIKEN RIBF*, Proceedings of IPAC2014, Dresden, Germany (2014) 1811–1813.

[39] E. Iliopoulou, et al., *Measurements and FLUKA Simulations of Bismuth and Aluminium Activation at the CSBF*, Tech. Rep. CERN–RP–2015–118–REPORTS–TN , EDMS 1566978 (2015).

[40] E. Iliopoulou, et al., *Measurements and FLUKA Simulations of Bismuth and Aluminum Activation at the CERN Shielding Benchmark Facility (CSBF)*, Proceedings of SATIF 13, Dresden, Germany (2016).

[41] E. Iliopoulou, et al., *Measurements and FLUKA simulations of bismuth and aluminium activation at the CERN Shielding Benchmark Facility (CSBF)*, Nuclear Instruments and Methods in Physics Research A 885 (2018) 79–85.

[42] A. Curioni, R. Froeschl, M. Glaser, E. Iliopoulou, F.P. La Torre, F. Pozzi, F. Ravotti, M. Silari, *Single- and multi-foils ^{27}Al (p,3pn) ^{24}Na activation technique for monitoring the intensity of high-energy beams*, Nuclear Instruments and Methods in Physics Research A 858 (2017) 101–105.

[43] N.Nakao et al., *Measurement and calculation of high-energy neutron spectra behind shielding at the CERF 120 GeV/c hadron beam facility*, Nucl.Instr.Meth.B Volume 266 (2008) 93–106.

[44] R. Froeschl, F.P. La Torre, N. Walter, *The ActiWiz material composition catalogue*, Tech. Rep. CERN-RP-2012-002-REPORTS-TN, EDMS 1277395 (2013).

[45] M. Lazzaroni, *Personal Communication*.

[46] F. Maekawa et al., *Production of a Dosimetry Cross Section Set Up to 50 MeV*, Proc. 10th International Symposium on Reactor Dosimetry, Sep. 12-17, 1999, Osaka, Japan, p.417, American Society for Testing and Materials (2001).

[47] R.Froeschl et al, *Radiation Protection Aspects of the Commissioning and Operation of the CHARM facility*, Presentation given at the SATIF-13 conference, Dresden, Germany, 10-12 October 2016.

[48] E. Iliopoulou, et al., *Measurements and FLUKA Simulations of Bismuth, Aluminium and Indium Activation at the CERN Shielding Benchmark Facility (CSBF)*, 2018 J. Phys.: Conf. Ser. **1046** 012004.